Experimental Characterization and Fracture Behavior of Graphene Nanocomposites

Cory Hage Mefford

A thesis
submitted in partial fulfillment of the
requirements for the degree of

Master of Science in Aeronautics and Astronautics

University of Washington
2017

Reading Committee:
Marco Salviato
Jinkyu Yang

Program Authorized to Offer the Degree:
Aeronautics and Astronautics

University of Washington

Abstract

Experimental Characterization and Fracture Behavior of Graphene Nanocomposites

Cory Hage Mefford

Chair of Supervisory Committee:
Dr. Marco Salviato
Department of Aeronautics and Astronautics

This work investigates the structural scaling of polymer/graphene nanocomposites. Fracture tests were conducted on geometrically scaled Single Edge Notch Bending (SENB) specimens with varying contents of graphene. It was shown that while the scaling of the pristine polymer follows Linear Elastic Fracture Mechanics (LEFM), this is not the case for nanocomposites, even for very low graphene contents. In fact, small specimens had a more pronounced ductility with limited scaling and a significant deviation from LEFM whereas larger specimens behaved in a more brittle way, with scaling of nominal strength closer to the one predicted by LEFM. This behavior is due to the significant size of the Fracture Process Zone (FPZ) compared to the specimen size which affects the overall fracturing behavior. This latter aspect needs to be taken into serious consideration since it is shown that, for the specimen sizes investigated in this work, neglecting the non-linear effects of the FPZ can lead to an underestimation of the fracture energy as high as 113%, this error decreasing for increasing specimen sizes. These findings were applied to previously published literature data, where it was shown that most of the specimens tested belonged in the transitional region between ductile and brittle behavior. As a result, the greatest deviation found between LEFM and SEL models was 156%.

Contents

List of Figures

ACKNOWLEDGMENTS

The author wishes to express sincere appreciation to the University of Washington, where she has had the opportunity to work with Dr. Marco Salviato, Yao Qiao, Fiona Spencer, Bill and Tuesday Kuykendall, Luke Richard and Anthony Deleo who helped the success of this research and to Hexion, Huntsman Inc, and TAP Plastics for providing the materials for this work.

DEDICATION

To my parents, for letting me take things apart,
and for my husband for helping me keep everything together.

Chapter 1

Introduction

1.1 Composite Materials

The use of composite materials in design applications has increased in popularity in recent years, but the use of these materials for construction is not a new phenomenon. The relative importance of four basic material groups in a historical context has been presented by M.F. Ashby, shown in fig. 1.1. It can be observed that since the 1960s, the use of metals has been reduced and the use of polymers, ceramics and composite materials has increased significantly [1, 5]. Specifically, wood used to be the primary building material in aerospace structures, which were later replaced with metallic materials. The current trend is that composite materials are increasingly being utilized in place of these metallic aerospace structures [1].

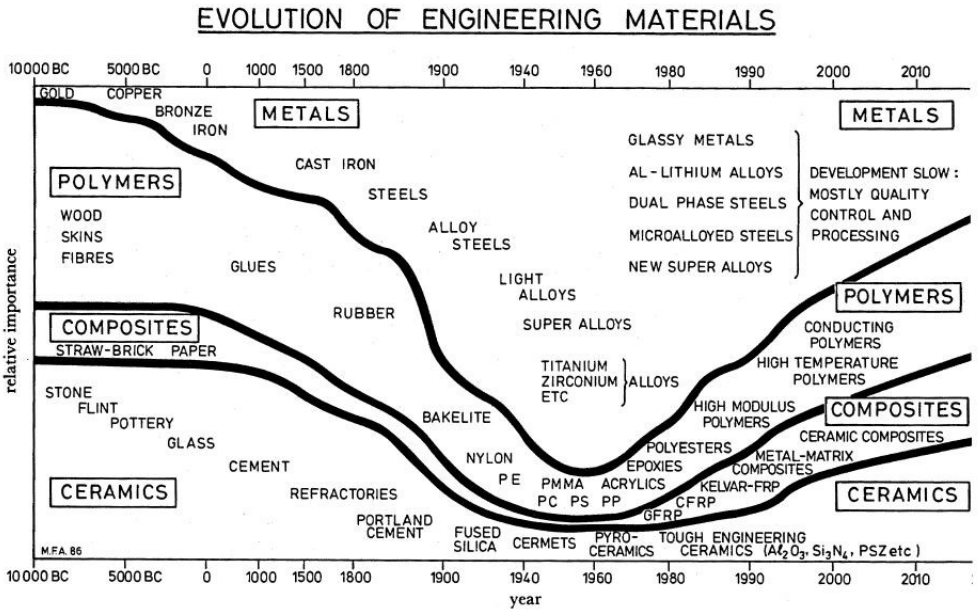

Figure 1.1: Schematic of the relative importance of four classes of materials (metals, polymers, composites, and ceramics) is shown as a function of time [1].

Composite materials are defined as materials that consist of two or more separate materials combined into one structural unit. The resulting material receives beneficial properties from the

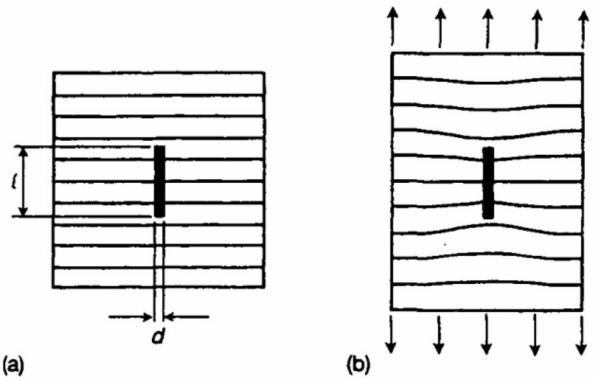

Figure 1.2: A cylindrical reinforcing fiber in a polymer matrix: (a) in the undeformed state; (b) under a tensile load [2]

parent materials, which can result in a material that is stronger and lighter than the parent material are on their own. Early fiber reinforcement can be seen in the use of plant material in clay bricks around 2000 BC. It is thought that this was done to reduce the drying time and not to increase the strength of the final bricks. However, this idea has been carried through to current fiber reinforced composite materials such as steel-reinforced concrete and polymers reinforced with fibers made from glass and carbon [5].

One of the major problems with polymers in engineering is their low stiffness and strength when compared to metals, with the strength approximately 5 times lower and the moduli approximately 100 times lower. Fiber reinforcement is one method for fixing this problem. A good reinforcing additive has to be stiffer and stronger than the polymer matrix; it has to have a good particle size, shape and surface character for effective mechanical coupling to the matrix; it must preserve the desirable qualities of the polymer matrix. To examine the mechanism of reinforcement, one can consider the case of a single cylindrical reinforcing particle embedded in and perfectly bonded to a block of polymer matrix. As pictured in fig. 1.2(a), the particle is of length l and diameter d and is unloaded. In fig. 1.2(b), a tensile load is applied, with the horizontal lines deforming with the tensile load in order to illustrate the strain distribution that has developed. Since the particle is stiffer than the matrix, it deforms less which causes the matrix strain to be reduced overall, especially in the vicinity of the particle. The particle achieves its restraining effect on the matrix entirely via the particle-matrix interface. This highlights the critical role played by the interface. The strength of the composite depends on the strength of the bond between particle and matrix. The more the particle and the matrix can interface, the more effective the reinforcement [2]. This means that the nanoparticle that is chosen must have the ability to interface strongly with the desired matrix material.

From McCrum *et al.*, we get a useful parameter for characterizing the effectiveness of a reinforcement, through a comparison of the ratio of surface area of a particle to the volume of reinforcement. For a particle, if the surface area is A and its volume is V, it is required that the surface-to-volume ratio ($\frac{A}{V}$) to be as large as possible. For a cylindrical particle,

$$\frac{A}{V} = \left(\frac{2\pi}{V}\right)^{\frac{1}{3}} (a^{-\frac{2}{3}} + 2a^{\frac{1}{3}})$$

where $a = \frac{l}{d}$. This relationship is has been plotted in fig. 1.3. It can be observed in that the

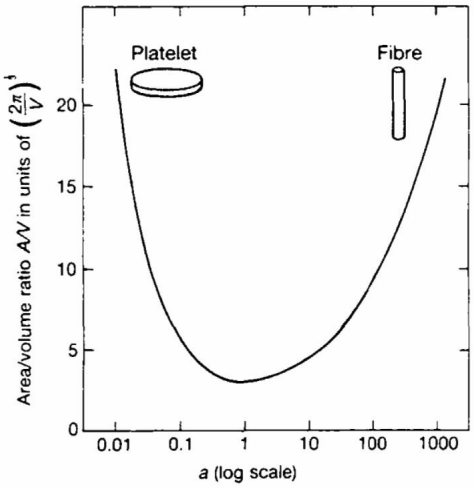

Figure 1.3: Surface-area-to-Volume ratio A/V of a Cylindrical particle of a given volume, plotted versus aspect ratio $a = l/d$ [2]

predicted optimum shape for the reinforcement is when $a >> 1$ (fiber) or $a << 1$ (platelet). These shapes maximize the particle matrix interaction through the interface [2].

The quality of this interface between the filler and matrix is effected by the matrix chemistry, which in turn affects the reinforcement that is observed. In Working, *et al.* they did a comprehensive study using two different matrix materials and ten different fillers. They found that the dispersion was better in one matrix material over the other for all of the nanofillers tested. They also found that the nanofiller quality and processing conditions play a large role in the effectiveness of the final composite material [6].

Since we are purely looking at carbon nanofillers in this work, it is important to show the difference between the different carbon filler options. Long carbon fibers and carbon nanotubes fall into the "fiber" category and graphite and graphene would fall into the "platelet" category. As you can see from fig. 1.3, neither the "fiber" form and the "platelet" form is better than the other in terms of effectiveness as a filler. There is no filler that works with all polymers. Instead, the best choice is to look at what filler is best suited for the polymer of choice [6].

The size of reinforcements has been reduced over time, from the macro scale (diameter > 1 mm) to the micro scale. These smaller sizes offer a better opportunity to control the orientations and interactions with the matrix [7]. These materials have incredible material properties compared to their relative size and thickness. Recently, there has been increasing interest in carbon based "nanocomposites" which contain nanometer-sized reinforcements such as carbon nanoparticles, nanofillers, and nanotubes [5].

1.2 Nanocomposites and Nanoparticles

To fully understand why carbon nanocomposites are so important, it is first key to understand what makes carbon such a unique periodic element. Carbon is the fourth most abundant element on earth and it is the building block of organic chemistry. One of the most impressive characteristics of carbon is that it has the ability form large stable frameworks of interconnecting bonds with different hybridizations. This allows carbon to form numerous two-dimensional and three-dimensional compounds [3].

This ability to take many crystalline forms, forming many different allotropes (see fig. 1.4). The two most well-known allotropes of carbon are graphite and diamonds. However, in recent years, many more allotropes of carbon have been discovered, including single-walled carbon nanotubes and graphene.

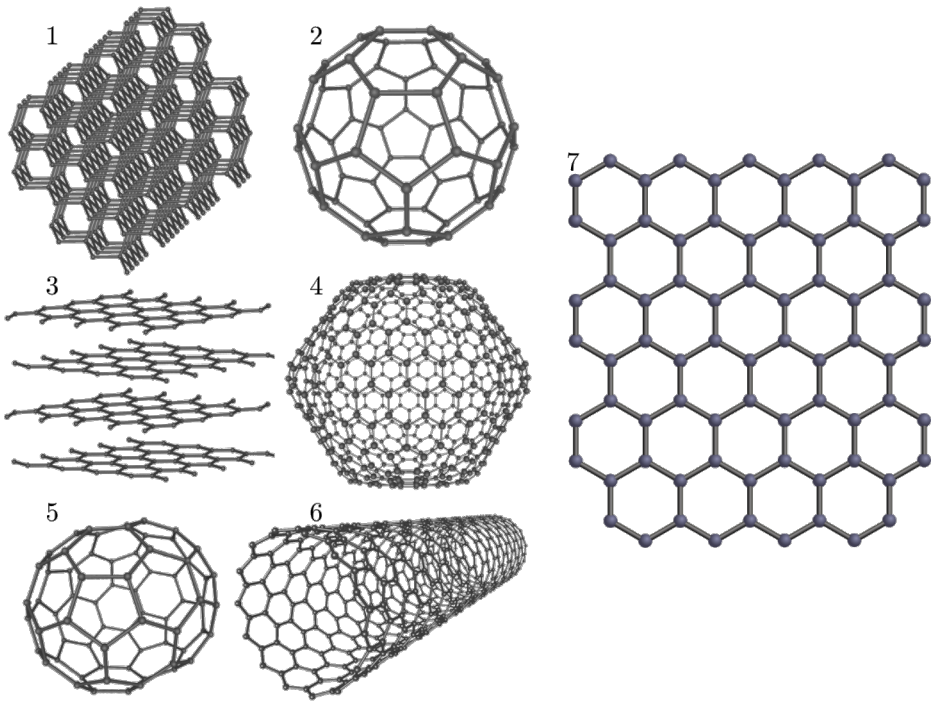

Figure 1.4: Allotropes of Carbon: Diamond (1), Buckminsterfullerene-C60 (2), Graphite (3), C54 (4), Fullerene-C70 (5), Single-walled carbon nanotube (6), and Graphene (7) [3]

Graphene, graphite and carbon nanotubes are very similar in structure which also means that they share some material properties. However, their differences plays a role in how they behave as nanofillers. Carbon rings are composed of many carbon atoms that are covalently bonded together to form a hexagonal ring shape. Graphite is composed of many layers of carbon-ring sheets, bonded together through van-der-Waal's forces. Carbon nanotubes are composed one or more layers of carbon ring sheets in a cylindrical form. Graphene is composed of three or more carbon rings in sheet form. Another method of understanding their structure is that graphite is made from many graphene sheets and carbon nanotubes are made from one or more sheets of graphene "rolled up" to form a tube form. In fig. 1.4, the structure of graphene can be seen in cell 3 and in greater detail in cell 7. Graphene was originally thought of as a hypothetical molecule that was too unstable to be synthesized until Geim and Novoselov isolated graphene in 2004 [8]. Its two-dimensional structure was the strongest material tested, showing high strength and electrical conductivity properties [9]. Graphene's two-dimensional structure allows for it to very effectively transfer its strength and mechanical properties to the host material. This makes it a much better choice for a nanofiller than other conventional carbon nanotubes and nanoclays [10].

1.3 Polymer Fracture Toughness

To better understand why graphene was the chosen nanofiller for this work, it is important to understand why epoxy resins could benefit from reinforcement, what characteristics we are looking to improve and how graphene is a better method to get those results.

Epoxy resins are a type of thermoset polymers, designed to cure through the reaction of epoxide groups with the use of a chemical hardener. They are unique among other thermoset resins due to their ease of use, low cure shrinkage (which reduces residual stresses in the final product) and ability to control the degree of crosslinking through the use of different hardeners [7]. Epoxies are not just used for adhesives and coatings but are also used in structural engineering as matrices in fiber reinforced composites. They are a strong choice for this application because of their low moisture absorption, high modulus, and temperature performance. One of the undesirable features of epoxy is that it is quite brittle and vulnerable to crack. Epoxy also has very little fracture resistance [11]. Therefore, many types of fillers are being explored in order to increase the polymer fracture toughness (K_{1C}) so that they will perform better in fiber reinforced composites.

There are two main types of fillers currently being researched. One is rigid micro-scale thermoplastics, which work well in certain situations, but often increase the overall strength but decrease the toughness of the composite material. This is the result of the filler acting similar to a defect and which can induce stress concentrations. This can initiate and increase cracks to be larger than the critical crack size that typically causes failure [12]. These particles also can deform and create cavitations in the matrix as an external force is applied, which creates defects allowing for crack propagation [13]. The other class of fillers, and the one that is the primary focus of this experiment, are carbon-based nanofillers. Carbon black, carbon nanoclay, multi-wall and single-wall carbon nanotubes (MWCNT and SWCNT), graphene oxide (GO), and graphene nanoplatelets (GNP) are some of the more popular types currently being researched.

Graphene nanoplatelets (GNP) were chosen as the nanofiller for this experiment over the other choices for a few important reasons. One of the downsides of carbon nanotubes, graphene oxide, and carbon black as filler choices is that they significantly increase the viscosity of the epoxy resin at higher concentrations. However, this effect has not been seen in graphene/epoxy composite materials. This means that a broader array of concentrations of graphene can be used, which allows for better mechanical property gains in the final material [9, 11, 14, 15]. In addition, when creating composites using vacuum resin transfer molding, viscosity needs to be low to allow for proper resin distribution. Therefore, having a filler that does not increase the viscosity is very beneficial for this process, since less is needed to get comparable results to other nanofillers.

Secondly, GNPs have a high surface area compared to other nanofillers. This is an important trait because the increased surface area is what allows for stronger bonding between the filler and the matrix. This bond is what allows for proper energy transfer between the matrix and the filler, which determines the toughness of the material. This also means that less graphene needs to be used to get the same results comparable to nanotubes since the available surface area of graphene is so much larger. This also lowers the overall weight of the final material as well. Zaman, *et al.* [16] tested studied the effect that the interface has on an epoxy/graphene platelet composite. They used graphene platelets (GP) and modified graphene nanoplatelets (m-GP) which were specially treated to allow for greater adhesion to the epoxy. Graphene platelets are a novel class of nanofillers due to their good compatibility with most polymers, high aspect ratio, high absolute strength and cost effectiveness. They found that the addition of GP and m-GP showed an improvement to the G_{1c} of 104.3% and 200%, respectively, relative to the control.

It is important to note that the difference in the "tipping point" filler concentrations between these different studies shows that there is no one magic amount of any filler that will give the best

results. That it is instead a more complex problem, which involves many variables. The composition of the epoxy and the filler, the preparation of the samples, and the level of adhesion of the filler to the matrix all seeming play important roles in the success of an epoxy reinforced nanocomposite. Yet, too large of a concentration of nanofillers can cause the fillers to act like defects, causing the strength to be diminished. This is why testing needs to be done with a particular filler to find the best ratio of filler and epoxy [6].

1.4 Graphene Nanocomposites

Thanks to their outstanding specific mechanical and functional properties, the engineering use of polymer/graphene nanocomposites is becoming broader and broader. Current applications include electronics, additive manufacturing, energy storage devices and the use as nanoreinforcement for advanced carbon fiber composites [17–19]. These outstanding properties have been extensively confirmed by a large bulk of literature aimed at understanding the mechanical behavior of these materials and optimizing their application.

Wang *et al.* [20] investigated the effect of graphene morphology on the main toughening mechanisms of polymer/graphene nanocomposites. They found that the toughening effect strongly depends on the size of graphene sheets with the best performance being related to the smallest sheet sizes and the main toughening mechanism being microcrack deflection.

A comprehensive analysis on the mechanisms of damage of graphene based nanocomposites was carried out by Chandrasekaran *et al.* [11, 21] who showed that micro-crack deflection, crack pinning and separation of graphene layers are the main sources of energy absorption. Further, the thermoset system investigated showed an outstanding enhancement of fracture toughness and electric conductivity.

An improvement of the fracture toughness and thermal conductivity was reported by Lee *et al.* [22], who studied thermoset polymers modified by functionalized graphene, whereas the effect of graphene dispersion on the mechanical properties was investigated by Tang *et al.* [23]. Several other studies confirm the outstanding performance of graphene nanocomposites (see, among others, [24–26]).

While a large bulk of data on the mechanical properties of graphene nanocomposites are available already, an aspect often overlooked in the literature is the scaling of the fracturing behavior. This is a serious issue since the design of large nanocomposite structures or small-scale graphene-based electronic components requires capturing the scaling of their mechanical properties. This is challenging since, due to the complex mesostructure characterizing graphene nanocomposites (and other quasi-brittle materials such as concrete, ceramics, rocks, sea ice, and many bio-materials, just to mention a few), the size of the non-linear Fracture Process Zone (FPZ) occurring in the presence of a large stress-free crack is usually not negligible [4, 27–30]. The stress field along the FPZ is nonuniform and decreases with crack opening, due to discontinuous cracking, nano-crack deflection by graphene platelets, and frictional pullout of graphene layers [11, 20, 21, 25]. As a consequence, the fracturing behavior and, most importantly, the energetic size effect associated with the given structural geometry, cannot be described by means of the classical Linear Elastic Fracture Mechanics (LEFM). To capture the effects of a finite, non-negligible FPZ, the introduction of a characteristic (finite) length scale related to the fracture energy and the strength of the material is necessary [4, 27–30].

1.5 Size Effect

In classical linear theory, the elastic solution for the stresses at the vertex of an ellipsoidal cavity in an infinite solid was determined first by Inglis [31]. As is noted in fig. 1.5, the ellipse approaches the line crack (i.e. as the shorter axis tends to zero), the stress at the vertex of the ellipse tends to infinity. Griffith later used this to determine that in the presence of a crack, the stress value cannot be used as a criterion of a failure since the stress at the tip of a sharp crack in an elastic continuum is infinite no matter how small the applied load. This led him to propose an energy criterion of failure which is the basis for linear elastic fracture mechanics (LEFM) [4].

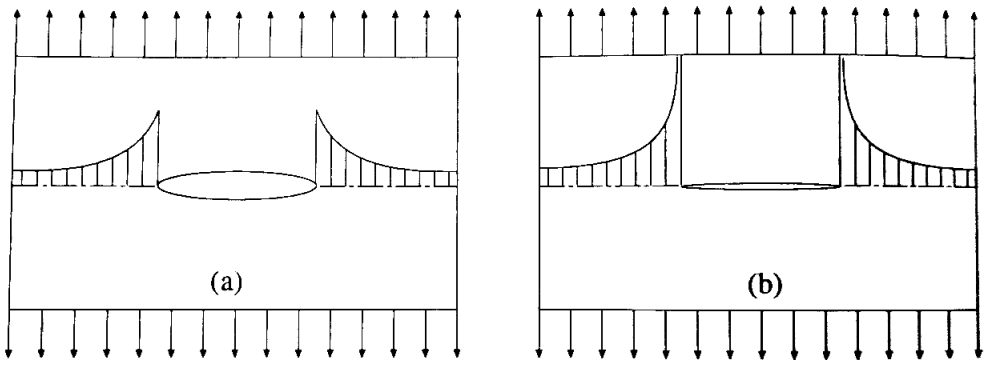

Figure 1.5: (a) The stress at the ellipse vertices is finite in an elastic plate with an elliptical hole; (b) the stress concentration tends to infinity as the ellipse shrinks to a crack [4]

Size effect is the deviation from the prediction that the load capacity predicted by plastic limit analysis or any (deterministic) theory in which the material failure criterion is expressed in terms of stress, strain or both [4]. The conventional wisdom is that mechanical properties scale linearly according to linear elastic fracture mechanics (LEFM) which means that the strength (σ_N) and the structure size (D) are independent of each other. Size effect states that mechanical properties scale non-linearly and that there is a significant relationship between the specimen geometry and the Fracture Process Zone (FPZ).

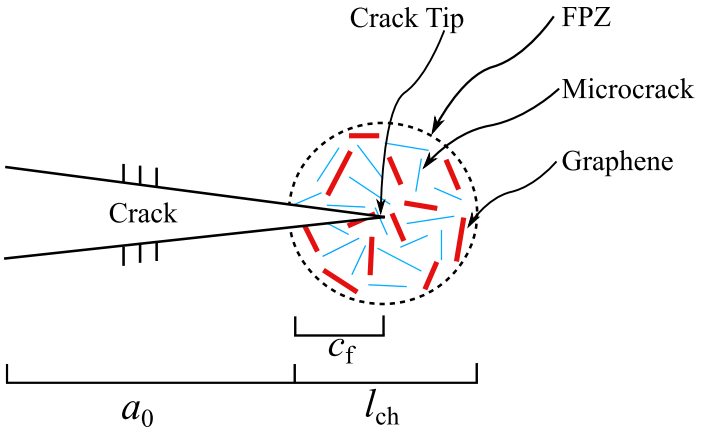

Figure 1.6: Fracture process zone for a quasi-brittle material where a = effective crack length $a = a_0 + c_f$ with a_0 = initial crack length and c_f = effective FPZ length and l_{ch} = characteristic length

The fracture process zone (FPZ) (see fig. 1.6) is a nonlinear zone characterized by progressive softening, for which the stress decreases at increasing deformation. This zone is surrounded by a nonsoftening nonlinear zone characterized by hardening plasticity of perfect plasticity, for which the stress increases at an increasing deformation or remains constant [4]. Quasibrittle materials, such as concrete, ceramics, and nanocomposites, are characterized by a complex mesostructure. This means that the size of the fracture process zone (FPZ) occurring in the presence of a large stress-free crack is non-negligible and its effect must be considered. The stress field along the FPZ is nonuniform and decreases with a crack opening, due to discontinuous cracking, crack bridging by fibers, and frictional pullout of inhomogeneities. As a consequence, the fracturing behavior and, most importantly, the energetic size effect associated with the given structural geometry, cannot be described by means of the classical LEFM [27].

Noted in fig. 4.2, the fracture process zone contains microcracks, which weaken the material around the crack tip. This allows the crack to propagate more easily through the material. It is thought that nanoparticles over a certain concentration will interfere with the FPZ, making the material have a greater tendency to fracture at a lower critical load. The FPZ size is constant among all sizes of specimens. This means that for large specimens its effects are negligible but for small specimens, the FPZ size is comparable to the structure characteristic length. This means that the slightly non-linear stresses in the FPZ strongly affect the global behavior of the material.

It is also worth mentioning that using the size effect method of measuring the fracture properties is easier to implement than other methods because only the peak load is needed. Post peak behavior, crack tip displacement measurement and optical measurements of the crack tip location are not necessary [27]. What is being investigated in this work is the effect that graphene nanoparticles have on the size effect and fracture toughness of epoxy for future use in carbon fiber/epoxy composites.

The accurate scaling of mechanical properties is crucial

1.6 Objectives of this Work

This work is an investigation of the structural scaling of polymer graphene nanocomposites. To this end, fracture tests were be conducted on geometrically scaled Single Edge Notch Bending (SENB) specimens with varying contents of graphene. This was done to study the effects of nanomodification on the scaling. It is shown that while Linear Elastic Fracture Mechanics (LEFM) is an accurate method for predicting the behavior of pristine materials, that this is not the case for predicting the behavior of graphene nanocomposite composite materials, especially when the test specimens are small and for very low graphene contents.

Through the analysis of the nominal strength as a function of the specimen size, it is shown that small specimens have a more pronounced ductility with limited scaling and a significant deviation from LEFM whereas larger specimens behave in a more brittle way, with scaling of nominal strength closer to the one predicted by LEFM. This behavior is due to the significant size of the FPZ compared to the specimen size which affects the overall fracturing behavior.

Accounting for the FPZ size is of utmost importance to capture the scaling of the structural behavior and to correctly estimate the fracture energy of the material from fracture tests. It is shown that the use of LEFM to estimate mode I fracture energy of the nanocomposites leads to non-objective results, the fracture energy depending on the size of the specimen tested. It is also shown that, by introducing a length scale related to the FPZ size by means of an Equivalent Crack approach, a formula for the scaling which depends not only to the material fracture energy but also to the FPZ size can be derived. This formula, known as Bažant's Size Effect Law (SEL) [4, 28–30], enables an excellent fitting of the experimental data and the objective estimation of the fracture

energy and the FPZ size. A comparison between LEFM and SEL showed that for the small specimen sizes investigated, the difference can be as high with this difference decreasing for larger specimens as the effects of the FPZ become less significant in the context of the larger portion of the specimens in the linear elastic regime.

Chapter 2

Material Preparation, Specimen Manufacturing and Testing

2.1 Specimen Geometry

There were two different types of mechanical testing performed in this work. The first was Single Edge Notch Bending (SENB) testing. The design of the SENB test specimens were based on the standard ASTM D5045-99 [32]. Since the scaling of fracture mechanical properties is what is being investigated, test coupons were created in four different sizes, keeping the aspect ratio consistent for the length and width of the specimen but keeping the thickness identical between all specimens. By keeping the aspect ratio identical, we will be able to better determine the effect that scaling has on fracture toughness. The measurements of each specimen is illustrated in fig. 2.1 and table 2.1. The proportion of the four coupon sizes relative to each other is 1:2:4:8, which is illustrated in fig. 2.2.

Size	Width, D	Gauge Length, L	Length, $L = L + 2L_i$	Crack Length, a_0	Thickness, t
Size 1	10	36	42	5	12
Size 2	20	72	84	10	12
Size 3	40	144	168	20	12
Size 4	80	288	336	40	12

Table 2.1: Geometrical specifications of the SENB specimens under study. Units: mm

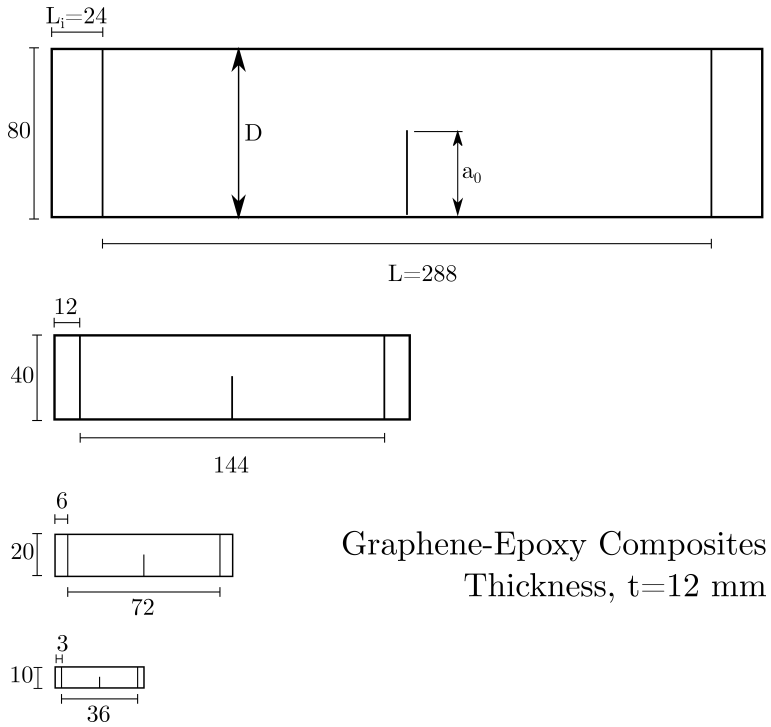

Figure 2.1: Geometry of Single Edge Notch Bending (SENB) Specimens under study. Units: mm

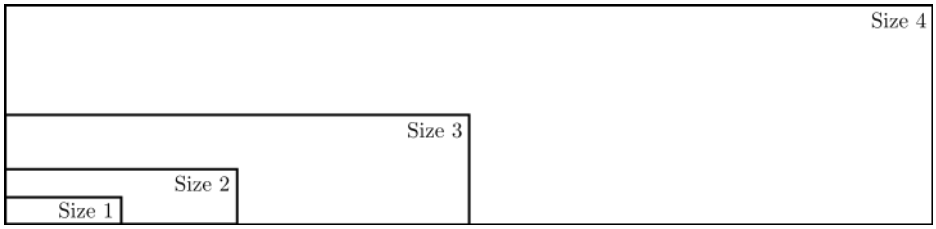

Figure 2.2: Relative Specimen Sizes

The second testing method done was uniaxial testing which utilized dogbone test coupons. The dogbone specimens were based on the standard ASTM D638-02a [33]. The specimens, illustrated in fig. 2.3, were designed so as to ensure that no significant stress concentrations where formed along the neck, which would cause fracture outside of the gauge length. Therefore, the tabs and center portions of the specimen were set at 40 mm and the width of the center portion were set to 12 mm. Tangent curves were made at the junction between the tabs and center section. These curves were allowed to be any length that allowed for a smooth transition. These curves are what determined the overall dimensions of the specimens. Six material configurations characterized by different graphene weight contents were prepared for uniaxial tensile tests: pure epoxy, 0.3 wt%, 0.6 wt%, 0.9 wt%, 1.2 wt%, and 1.6 wt%.

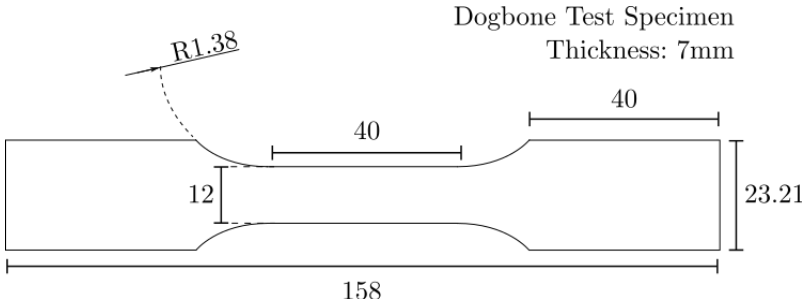

Figure 2.3: Geometry of Dogbone Tensile Test Specimen (Units: mm)

2.2 Mold Design and Creation

The epoxy specimens were created using custom silicone molds designed and manufactured especially for this experiment. 3D printed mold positives were created for use in making the silicone molds. Typically these mold positives are molded out of steel, but this subtractive manufacturing process can waste a great deal of material to create the desired part. 3D printing is an additive manufacturing process that wastes much less material. An added benefit is that it can be a far cheaper and faster solution. In total, four SENB coupon sizes and one dogbone mold configuration were be created.

The first step was to create the mold positives in Solidworks, based on the coupon designs. These mold positives were designed so that silicone can be poured into it to make mold of the desired thickness and dimensions. For the smaller coupon sizes, we were able to fit multiples of each coupon into one mold. From these positives, many molds can be created to accommodate the number of sample coupons we wish to study. The mold positive designs were made so that they use the minimum amount of material but contain enough clearance around each specimen so that the final mold will be strong enough. Please see the "Drawings" section in the appendix, for more detailed drawings for each specimen.

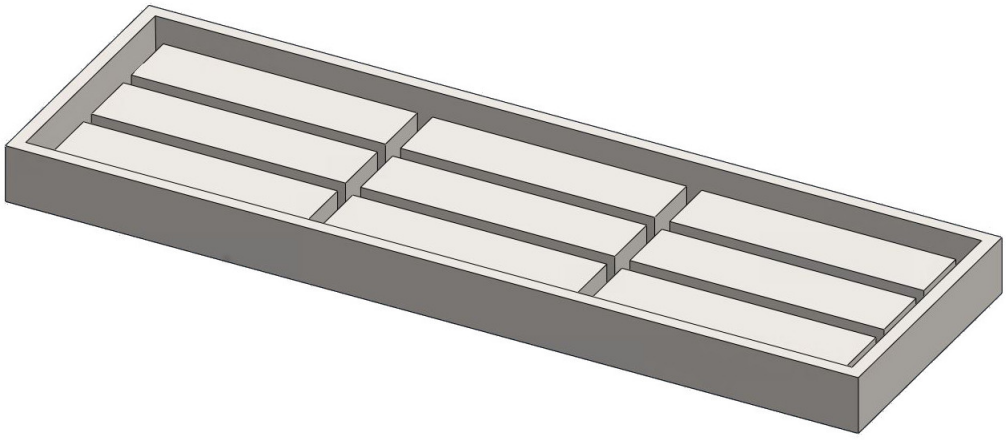

Figure 2.4: Mold Positive for Specimen Size 2

The next step was to have these specimens 3D printed. The mold positive designs for the four 3-point-bending test coupon sizes were created in a FORTUS 400mc 3D printer as seen in fig. 2.5.

Figure 2.5: Fortus 400mc 3D printer: a) exterior; b) detail of the interior

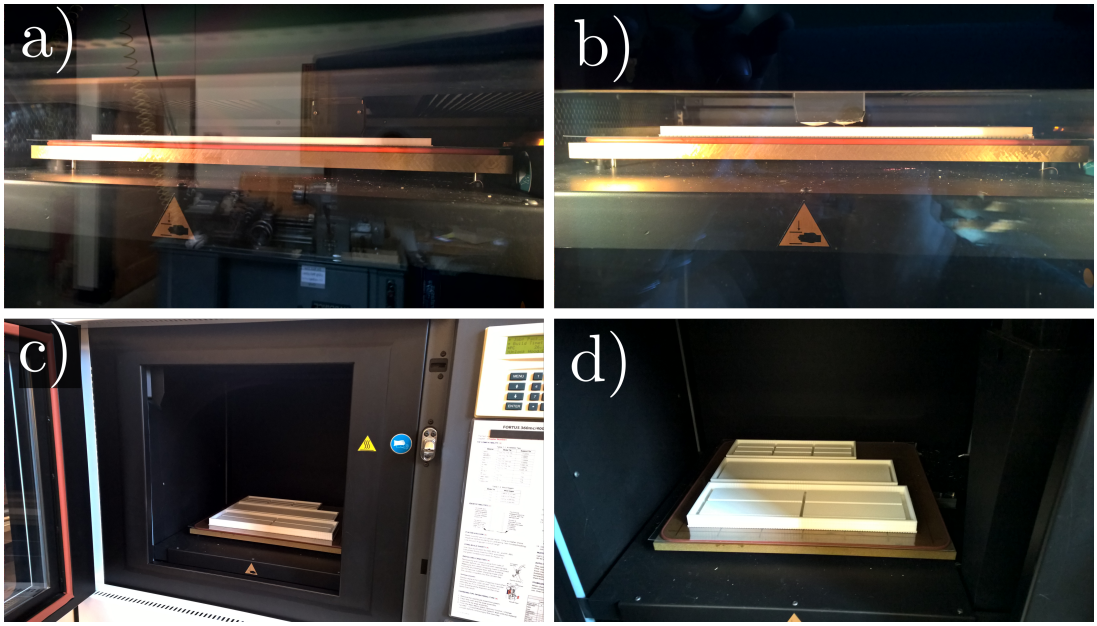

Figure 2.6: Single edge notch mold positive printing process: a) view from outside of the machine while printing is in progress; b) additional view where printing head can be seen; c) view of finished mold positives; d) detail of finished mold positives

The samples were printed in two different batches in the printer for a total print time of approximately 12 hours. In the printing process, support material was placed in the parts to ensure they have the correct final form (fig. 2.5a-d). This support material was removed by hand, using pliers (fig. 2.7b-c). Each sample was then sanded and spackle was applied to smooth out the surface texture (fig. 2.7d). The models were painted with spray primer and allowed to dry completely. Finally any remaining irregularities in the surface were filled again with spackle, the

surface was finely sanded and another coat of primer was applied. The purpose of this process is to remove the surface texture that samples printed in this manner naturally have. A glass-type finish was not necessary, by only a surface smooth enough to not allow a very pronounced texture to be transferred to the silicone. A texture in the silicone molds would then transfer that texture to the test composite coupons, which could cause defects in the coupons, compromising the final test results.

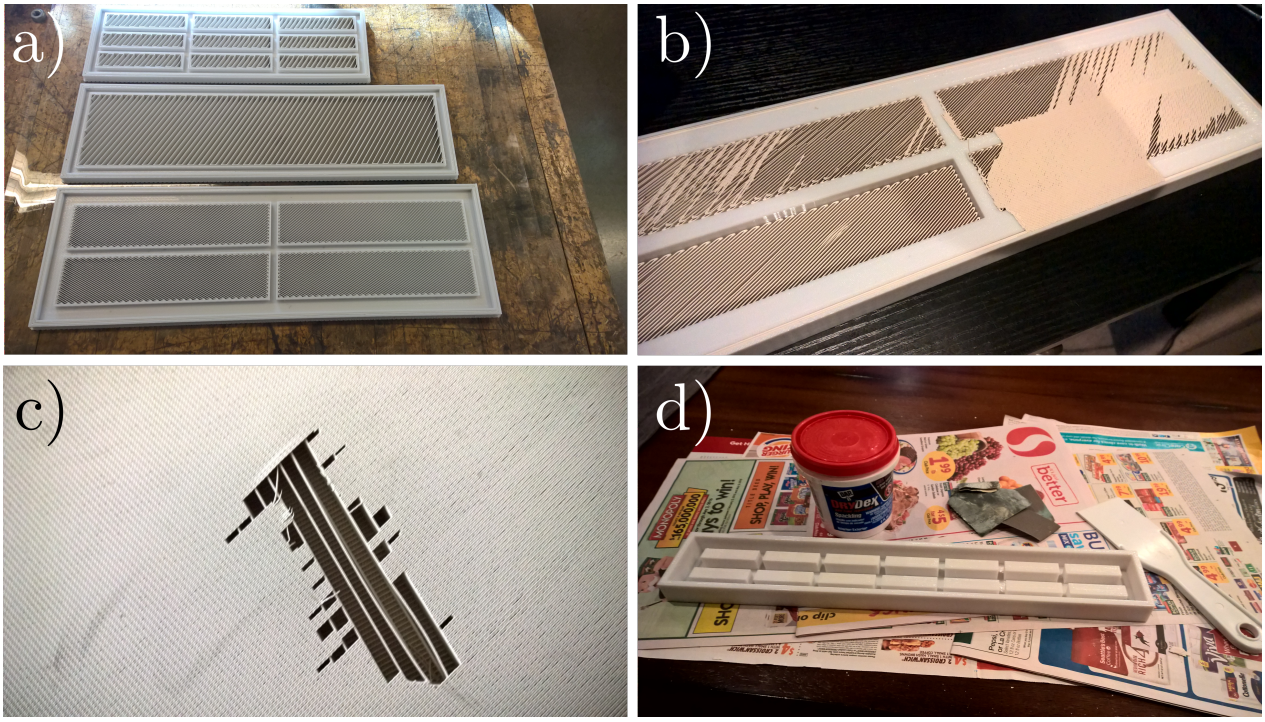

Figure 2.7: Support Material Removal Process and Spackle Application: a) mold positives and the support material; b) detail of partially removed support material inside the finished mold positive; c) detail of the support material; d) spackling process

The dogbone mold positive was created using a Stratasys Objet260 Convex printer, as seen in fig. 2.8a. This printer was the desired printer for all of the mold positives, but the size of the SENB mold positives exceeded the print range of this unit. The printing process was very similar to the Fortus 400mc, noted above. The mold positive was printed on a plate within the printer and took about an hour to print in total (fig. 2.8b-c). Support material was built into the model but it was a softer type of material. To remove it, the mold positive was blasted with pressurized water (fig. 2.8d). The final finish on this model was glass-like, so no sanding or painting was needed.

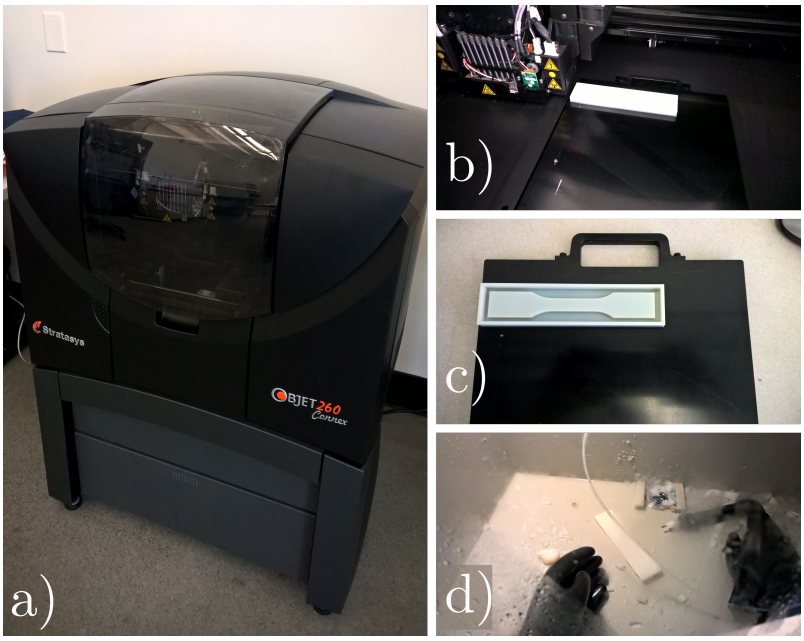

Figure 2.8: Objet 3D Printing Process: a) exterior of printer; b) inside of printer with dogbone mold positive; c) mold positive on printing tray; d) using water jet to remove support material

The next step was to create the molds for each of the five test sample types. The material used was RTV silicone from TAP Plastics [34]. This room temperature vulcanization (RTV) silicone rubber is a two component system that is catalyzed by tin compound to aid in curing process. Silicone was chosen as the mold material based on its low shrinkage, ease of use, and natural nonstick properties. The silicone and tin catalyst were combined using a ratio of 10-to-1, by weight. They were then manually mixed and poured into the mold positives (fig. 2.9a). Then smooth pieces of cardboard that were slightly larger that the mold being made were placed on top of the silicone molds and pieces of wood were placed on top of that (fig. 2.9b). This was done to ensure accurate detail reproduction and to ensure the mold has a flat base. The silicone mixture was quite viscous, so the mixture was allowed to cure for 24-48 hours, instead of the recommended 6-8 hours to allow for proper silicone cross-linking in the final molds. After this time, the silicone molds were removed from the mold positives, the cardboard was removed and had the edges and bottoms cleaned up using a cutting blade.

Figure 2.9: Creating Silicone Molds: a) pouring silicone mixture; b) applying pressure while molds cure

Once the molds were completed, it was now time create the epoxy test coupons. The epoxy and curing agents used for all the test coupons were EPIKOTE^{TM}Resin MGS^{TM}RIMR 135 and EPIKURE^{TM}Curing Agent MGS^{TM}RIMH 134-RIMH 137 [35]. The epoxy and hardener were combined in a 100:36 proportion (by weight). No solvent was used in this experiment, since the resin that is being used has a low viscosity, even after the addition of graphene. For the pure epoxy test coupons, which contained no graphene nanoparticles, the epoxy was manually mixed and poured into the silicone molds. These were allowed to cure at room temperature under the fumehood for 24-48 hours to ensure proper degassing and crosslinking. The samples were then placed in an oven for four hours at 60°C to further cure them. These samples where hand sanded to remove any surface imperfections and to ensure the sides of each test coupon was as straight as possible.

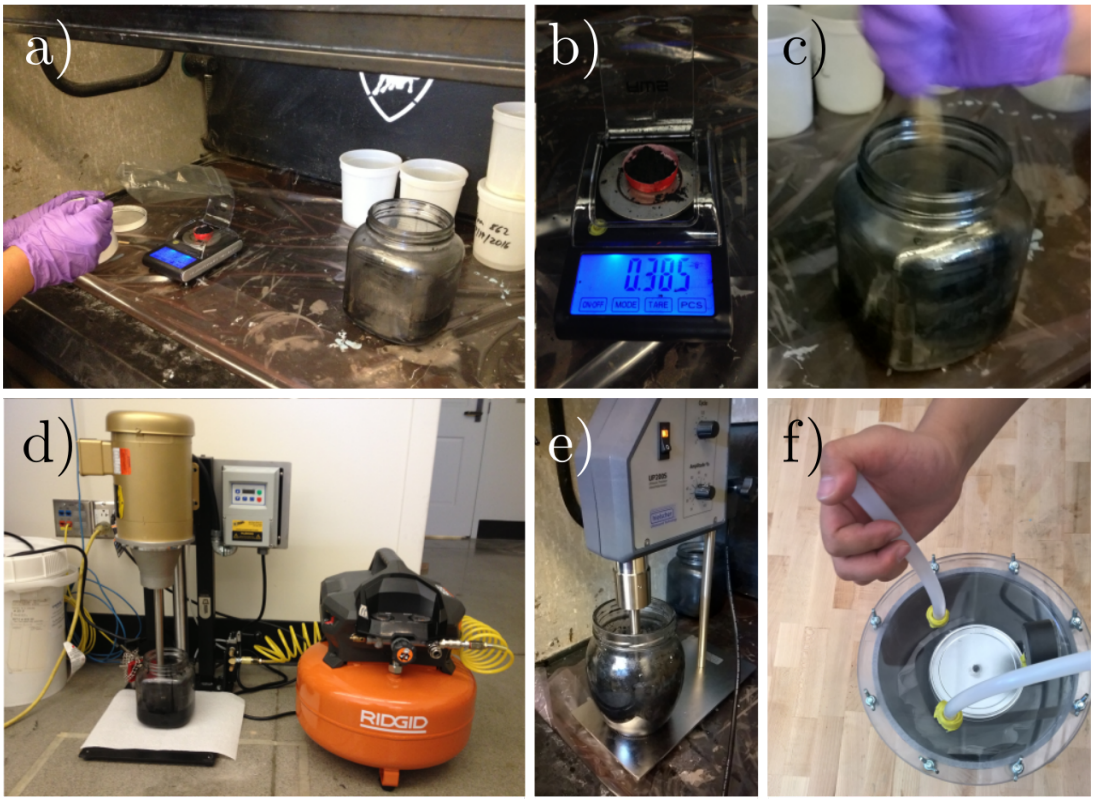

Figure 2.10: Graphene Specimen Preparation: a) weighing out the graphene; b) detail of the scale; c) manual mixing the graphene and epoxy; d) high sheer mixing with air compressor; e) sonication; f) degassing

The graphene used in this experiment was A-12 Graphene Nanoplatelet provided by Graphene Supermarket [36]. The average flake thickness is 3nm which is about 3-8 graphene monolayers with lateral dimensions of approximately 2-8 microns. The graphene used is pure and has not been functionalized. The process for making the graphene nanoparticle test coupons included the same steps detailed above with many more new steps, which are outlined in fig. 2.10:

1. The desired amount of epoxy was poured out according to how large of a batch was being made and this amount also determines the amount of hardener that will be used later
2. The amount of graphene needed for the specific batch was calculated, which depended on what concentration of graphene was desired for that batch
3. This amount was carefully and slowly measured out a few grams at a time and transferred to the container containing the epoxy (fig. 2.10a-b)
4. The epoxy/graphene mixture was manually mixed for 5 minutes (fig. 2.10c)
5. The epoxy graphene mixture was placed in an electrically activated high shear mixer (Mixer Direct [37]) with a 48 mm impeller and mixed for 20 minutes at 1500 rpm. (fig. 2.10d)
6. To promote platelet exfoliation, the mixture was sonicated using a Hielscher UP200S sonicator [38] with a 7 mm sonotrode for 20 minutes at 70% amplitude with a duty cycle of 0.5 (fig. 2.10e)

7. The mixture was degassed for 20 minutes using a Robinair 15400 vacuum pump [39] to remove air bubbles that might still be present in the material (fig. 2.10f)

8. The required amount of hardener was measured out and added to the epoxy/graphene mixture and manually mixed for 10 minutes and then poured into the silicone molds

9. The specimens were allowed to cure at room temperature for approximately 48 hours and then post-cured in an oven for 4 hours at 60°C.

It is worth noting that a similar procedure was successfully adopted by the authors for the exfoliation of nanoclays in thermoset polymer [40–42].

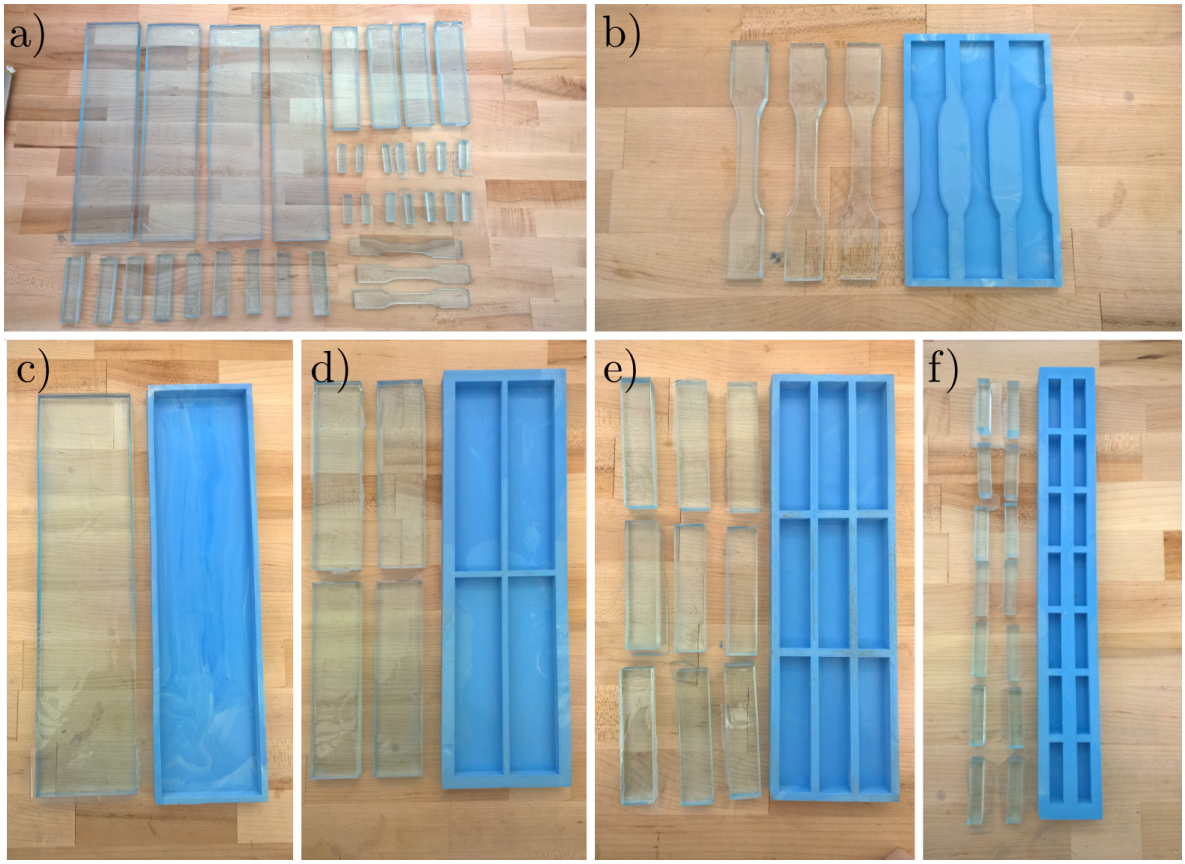

Figure 2.11: Silicone Molds and test coupons: a) group image; b) dogbone specimens; c) large specimen; d) medium specimens; e) second smallest specimens; f) small specimens. Material: Epoxy Resin.

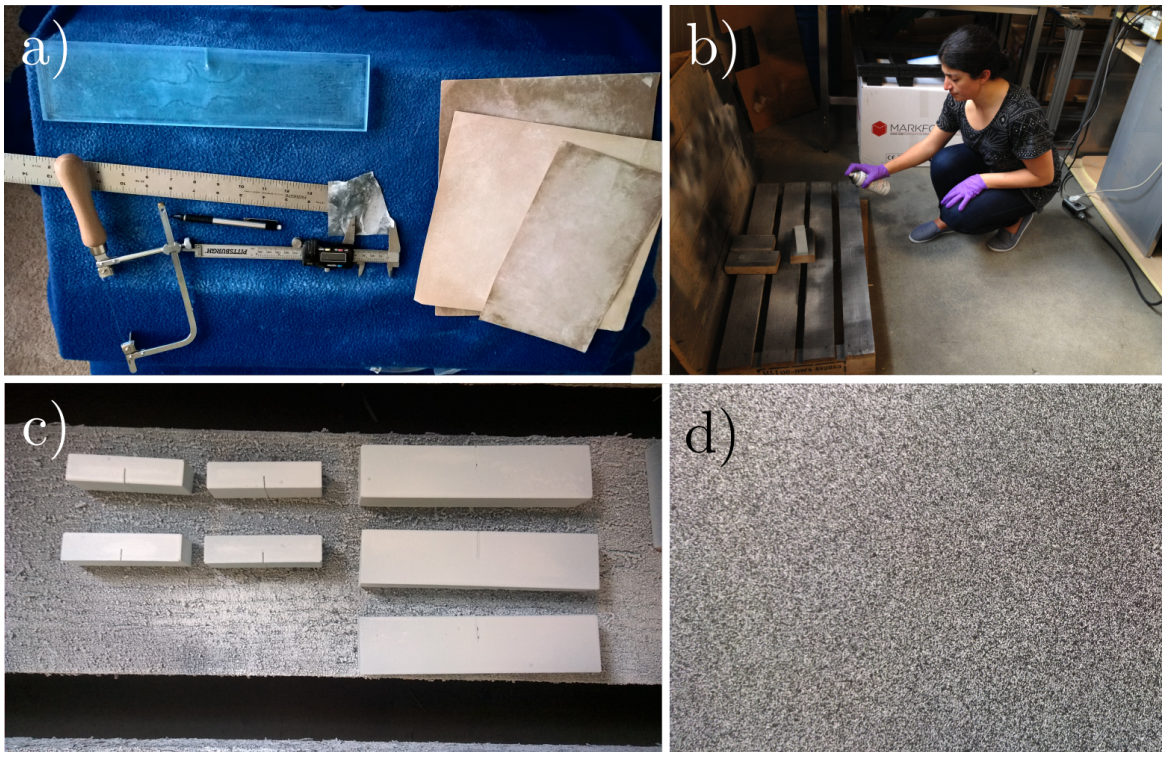

Figure 2.12: Crack Creation and Painting: a) measuring and creating the crack and performing surface sanding; b) painting process and speckling; c) specimens painted white before speckling procedure; d) detail of speckle texture for the DIC

After the curing process, the specimens were pre-cracked through a three stage process. First, a notch was created to about one-quarter of the specimen width by using a saw with a 0.2 mm diamond coated blade . Then the specimens were chilled at 0 °C for approximately 8 hours to facilitate the creation of the crack by tapping. Tapping was preferred to sawing to crate the last portion of the crack in order to provide a very sharp tip and to limit the emergence of plastic residual stresses [43, 44]. The pure epoxy specimens were completely transparent and the crack could be seen as it propagated through the specimen, until it reached the desired length. The epoxy/graphene specimens were completely opaque, even at the lowest concentration, which made identification of the crack tip very difficult. To overcome this issue, the specimens were painted white so that the contrast in color provided a better observation of the crack tip location. This was essential to guarantee that all the crack lengths were within 0.35-0.55 of the width of the specimens. This aspect is very important to guarantee a proper geometrical scaling.

2.3 Mechanical Testing

Three-point bending testing and uniaxial testing was performed using a closed-loop electroarticulated Instron 5585H machine (see fig. 2.15). The Instron was used in with Digital Image Correlation (DIC) camera and software system from Correlated Solutions [45]. The speckled paint pattern mentioned previously (see fig. 2.12d) was done in order to use the (DIC) software and equipment. The 3D-VIC DIC system was the specific technology used, which consists of a two camera system in conjunction with workstation containing special post-processing software which was synchronized with the load frame (see fig. 2.14). Its purpose is to measure and verify the mechanical results that are also being

measured at the same time by the Instron during each test. The DIC acts in place of a traditional strain gauge, with the added benefit of not causing stress concentrations at the contact points on the test specimen. It is expected that this method will yield more accurate results which can be compared to what is measured by the Instron. This is because it allows for the specimen to deform naturally and it does not take the average strain, but rather, the real time strain field is mapped, which will yield more post peak behavior. Additional benefits are the ability to view localized necking, discontinuous yielding and visualization and detection of cracks that are not visible by eye.

The DIC system works by taking images at a user-defined interval and those images are then analyzed in the specialized computer software, which looks at the deformation of the speckled pattern that has been painted on each sample.

For uniaxial testing, the load rate for all the dogbone specimens was 5 mm/min. The above images show the dogbone specimen under increasing loading (viewed from left to right) until fracture. It can be noted that the strain is clearly increasing until fracture occurs.

The rates for the single edge notch for each specimen size was altered to ensure that the strain rate remained consistent across all of the specimen sizes. Those strain rates can be seen in table 2.2. In total, over 150 specimens were tested to get the final results. The high number is the result of many samples breaking in the crack creation process, the crack not being the correct shape, or the results being too much of an outlier.

Specimen Size	Rate ($\frac{mm}{min}$)
Size 1	0.050
Size 2	0.075
Size 3	0.200
Size 4	0.300

Table 2.2: Displacement rates for single edge notch tests

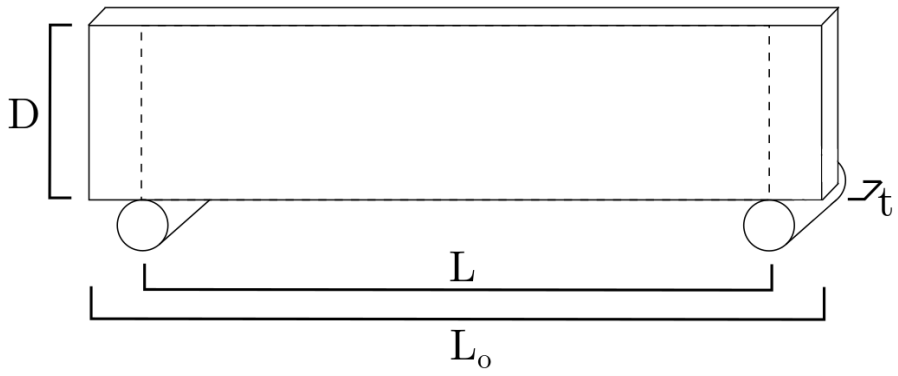

Figure 2.13: Variable Layout for Test Specimens

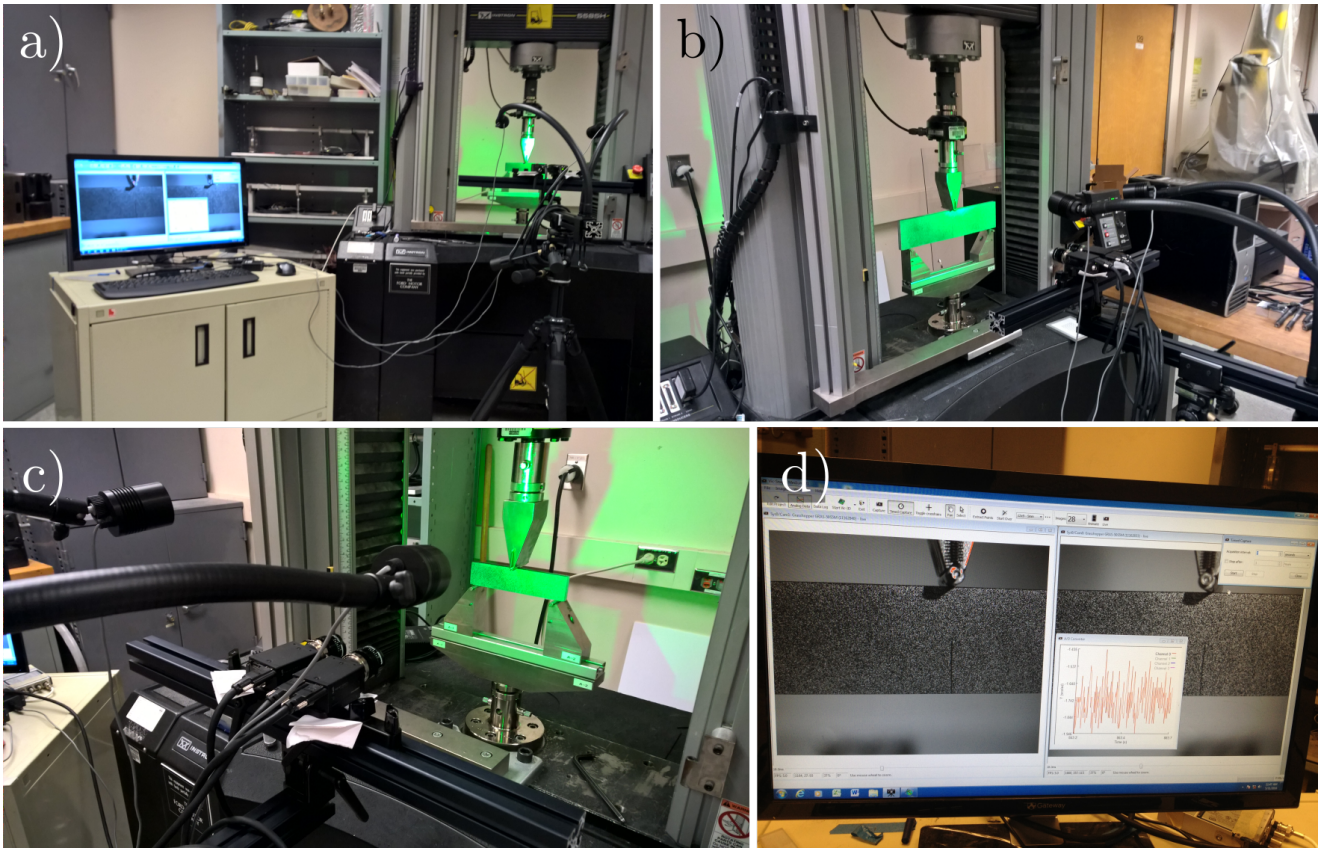

Figure 2.14: Digital Image Capture (DIC) system: a) DIC setup with computer station; b) detail of setup; c) cameras pointed toward sample; d) detail of computer where the camera images were viewed

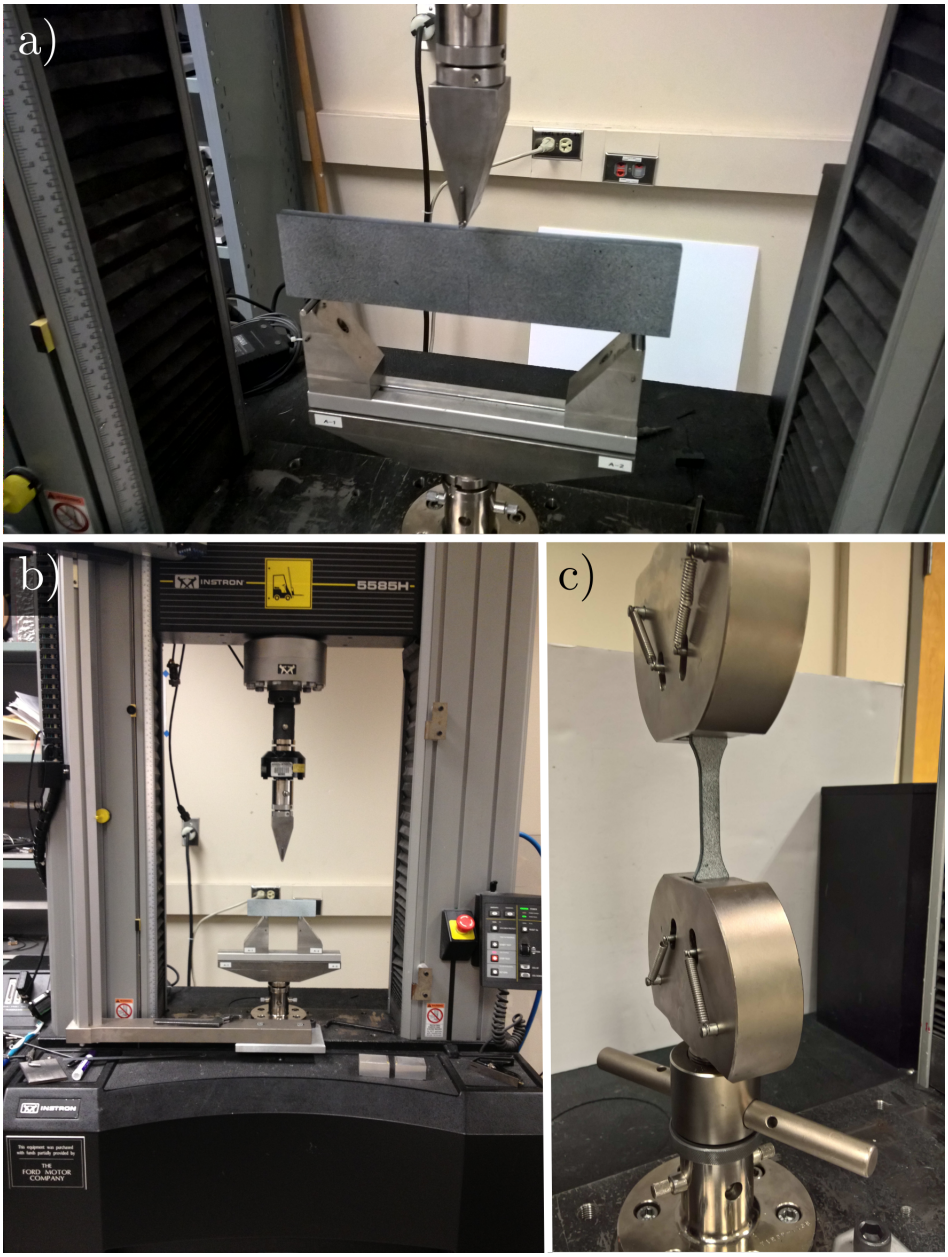

Figure 2.15: Instron Testing Machine: a) detail of SENB setup; b) view of instron machine; c) detail of dogbone setup

The design of the Single Edge Notch Bending (SENB) specimens was based on ASTM D5045-99 [32]. Four sets of SENB specimens were prepared for the three-point bending tests: pure epoxy, 0.3 wt%, 0.9 wt%, and 1.6 wt% graphene nanocomposites. In order to study the scaling of the fracturing behavior, as illustrated in fig. 2.1, geometrically scaled specimens of four different sizes were prepared for each material configuration. The dimensions, scaled as 1:2:4:8, were 10x36 mm, 20x72 mm, 40x144 mm, and 80x288 mm respectively. The various crack lengths of the specimens were approximately in the range 0.35D to 0.55D, where D is the width of the specimen. The scaling did involve the thickness, t, which was kept about 12 mm for all the investigated sizes.

2.4 Morphological Analysis

A major part of scientific evaluation is to thoroughly observe the form of the material. The use of a magnifying glass or an optical microscope are very effective methods for this purpose. However, as long as light is used, nothing smaller than the wavelength of light can be observed, which means observing a nano-structure is extremely difficult. A scanning electron microscope (SEM) utilizes an electron beam whose wavelength is shorter than that of light and allows for observation of a structure down to several nanometers in scale. The SEM machine that was used was a Jeol JSM-6010PLUS/LA electron microscope [46] where an acceleration voltage of 1 kV was applied, without sputtering.

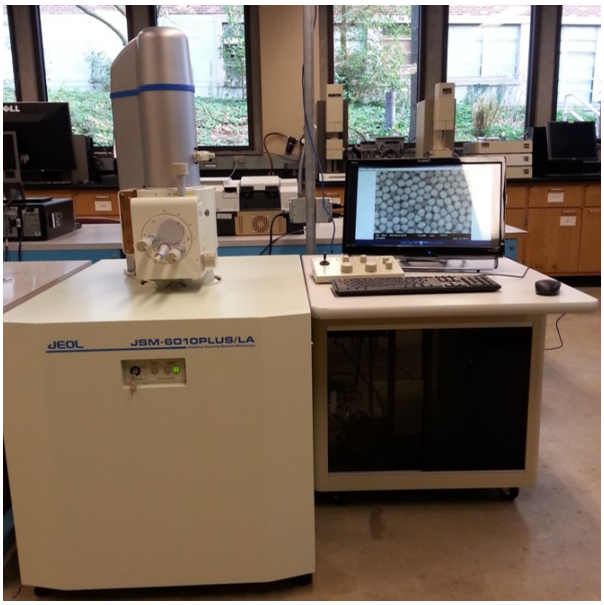

Figure 2.16: Jeol JSM-6010PLUS/LA scanning electron microscope

Since nanoscale graphene particles were used as a filler for the epoxy, the SEM technology was used in this experiment to properly analyze the fracture surfaces of the test single notch edge bending (SENB) specimens. This method was chosen because it enables a closer inspection of the fracture surfaces where the mechanism of failure can be determined and photographed. Through the SEM, images were captured at very high magnifications of the crack propagation around graphene nanoparticles. These images aided the analysis of the test specimens.

Chapter 3

Experimental Results

It is important to reiterate that the ASTM Standard D5045-99 [32] works well in certain situations, but because of the quasi-brittle nature of composites, the assumed linear relationship between the size of the specimen and the mechanical properties can produce inaccurate results. Through the use of size effect, which assumes a nonlinear relationship, the goal is to improve the accuracy of the results tested and simulated.

Even though four different sized specimens were created and made, the results for the largest specimen were inconsistent, partially as a result of the challenges in creating a crack of good quality. More work needs to be done to determine the best method for getting better results for this size. For this reason, the results for the largest specimen have been omitted from the final results.

3.1 Uniaxial Testing

The dogbone specimens were tested at the rate of $5\frac{mm}{min}$ and three specimens tested at six different graphene percent weight concentrations. These results were used to determine several mechanical properties. They were first used to determine the maximum engineering stress and true stress and to see if any changes occur as the concentrations vary. The true and engineering stresses were calculated as shown below:

$$True = \frac{P}{tW(1+e_{xx})^2}$$

$$Engineering = \frac{P}{tW}$$

Where P is the load, t is the specimen thickness, W is the specimen width, and e_{xx} is the strain in x. The Poisson's ratio was determined by using the same linear portion of the true stress plot (approximately 10 to 21 MPa) and plotting it against the strain in the y direction (e_{yy}). The slope of the best fit line was then used as the elastic modulus for that graphene concentration. The plots for the stresses for each graphene concentration can be seen below in fig. 3.1.

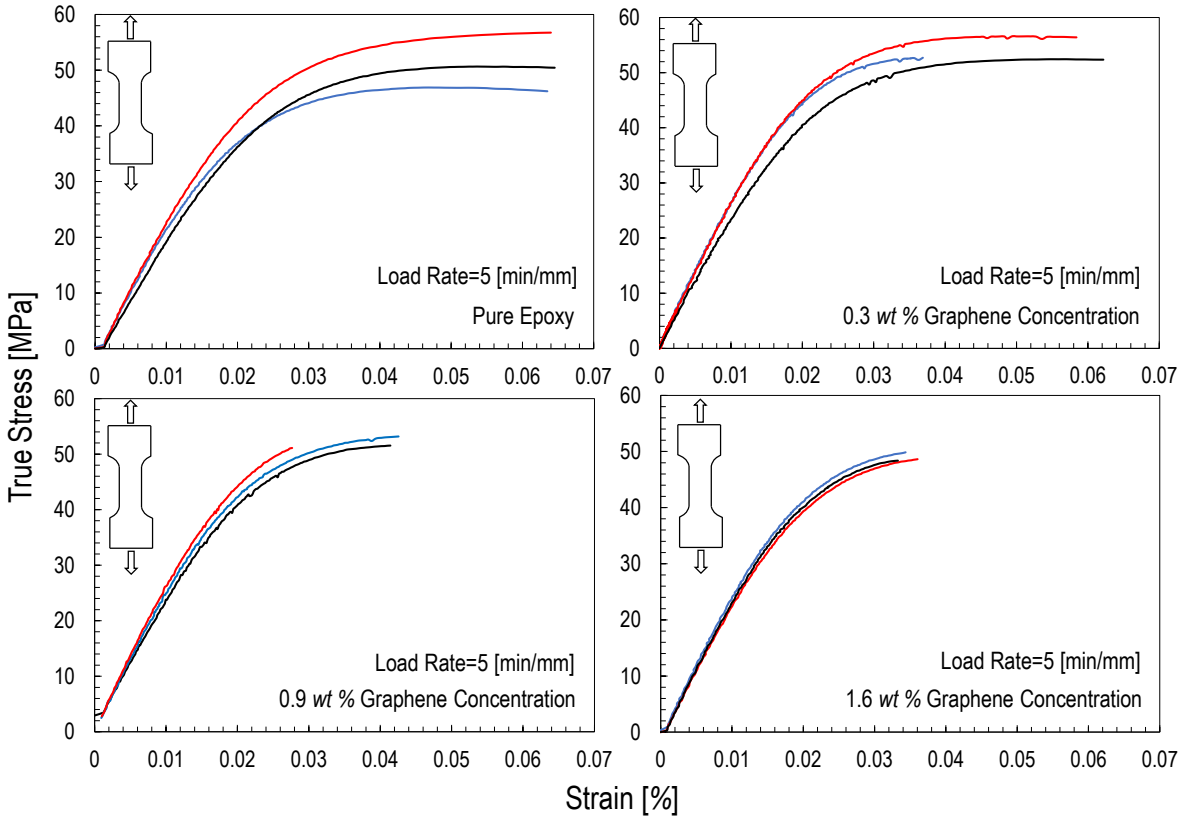

Figure 3.1: True stress vs strain measured from tensile tests on dogbone specimens

The final results for the max stress can be seen in fig. 3.2. While the true and engineering stresses show some variation over the course of adding higher concentrations of graphene, that change is very minimal when the error is considered. One can also see that the difference between results for the load rate of $1\frac{mm}{min}$ and $5\frac{mm}{min}$ are very similar and also show very little relative change to the engineering and true stresses.

It is worth mentioning that as a result of using the DIC, the stress-strain curves could be characterized in the presence of strain localization in the specimens, enabling the investigation of the behavior of the material at large deformations. This was particularly important since all the tests were characterized by a significant non-linear behavior which becomes less and less significant with increasing graphene content. This can be due to a higher presence of voids or defects with higher amounts of graphene which may lead to localizations and failures during the non-linear deformation.

The tensile test specimens were also used to accurately determine the elastic modulus, E, for each specimen graphene concentration. The elastic modulus was determined for each graphene concentration by measuring the elastic modulus from each of the three test specimens. Then, the average of those measurements was taken to get the final results. These values were used in later calculations to determine the K_{1c} and G_f. These results can be seen in tables 3.1 and 3.2. Even though the dogbone specimens were tested at these two different rates, the elastic modulus values from rate $5\frac{mm}{min}$ were used. The change in the modulus over different concentrations can be seen infig. 3.2. It can be observed that the modulus does not show a drastic change as the graphene concentration changes. There is a peak modulus value at $1.2\%wt$ under both loading conditions, but the overall difference between the concentrations is very minimal.

	$0\%wt$	$0.30\%wt$	$0.60\%wt$	$0.90\%wt$	$1.20\%wt$	$1.60\%wt$
Specimen 1	2164.1	2225.7	2039.7	2395.8	3129.1	2208.6
Specimen 2	2195.3	2439.5	2252.0	2343.3	3057.9	2262.6
Specimen 3	2505.8	2190.7	1858.7	2330.3	2923.8	2499.6
Average	2288.4	2285.3	2050.1	2356.5	3036.9	2323.6

Table 3.1: Young's Modulus Results for $1\frac{mm}{min}$ displacement rate dogbone specimens. Unit: MPa

	$0\%wt$	$0.30\%wt$	$0.60\%wt$	$0.90\%wt$	$1.20\%wt$	$1.60\%wt$
Specimen 1	2293.6	2553.7	2221.0	2241.6	2827.7	2461.4
Specimen 2	2364.7	2254.2	2320.7	2418.2	2778.1	2307.6
Specimen 3	2130.8	2587.7	2217.7	2596.9	2750.0	2389.6
Average	2263.0	2465.2	2253.1	2418.9	2785.3	2386.2

Table 3.2: Young's Modulus Results for $5\frac{mm}{min}$ displacement rate dogbone specimens. Unit: MPa

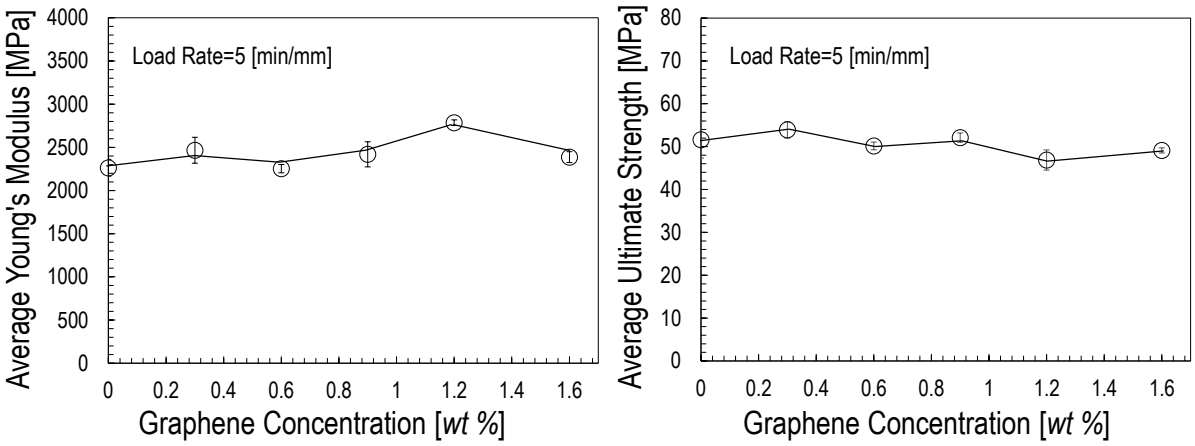

Figure 3.2: Young's modulus and ultimate strength as a function of graphene content

3.2 Single Edge Notch Bending (SENB) Testing

Single edge notch bending testing was done on graphene concentrations of $0.0\%wt$, $0.3\%wt$, $0.9\%wt$, $1.6\%wt$. The load-displacement curves for the three-point bending tests are plotted in fig. 3.4 for the graphene concentrations. It can be observed that for the pure epoxy specimens, the mechanical behavior is linear up to the peak load which is followed by unstable crack propagation. This is an indication of pronounced brittle behavior for all the sizes investigated. With the addition of graphene, differences in the behavior of small specimens with respect to large specimens become visible, this effect being more pronounced for higher graphene contents. In fact, while large specimens show a very linear response up to failure, a significant non-linear segment before the peak load characterizes the smaller sizes. This latter aspect indicates hardening inelastic behavior and reduced brittleness (or higher ductility) for the smallest specimen sizes. After reaching the peak load, the specimens exhibited snap-back instability for all the investigated sizes and graphene concentrations. As a consequence, the failures were catastrophic (dynamic) and occurred shortly after the peak load.

The crack length, maximum load, and nominal strength $\sigma_{Nc} = 3P_cL/2tD^2$ for geometrically scaled specimens of different Graphene Concentrations (GC) are tabulated in table 3.3. In the definition of nominal strength, P_c is the critical load, t is the thickness of the specimens, L is the span between the two supports, and D is the width of the specimens.

The size effect results can be seen in fig. 3.5. For all graphene concentrations, good grouping of the specimen data at the three different specimen sizes was achieved. The linear best fit line for each graphene percentage weight data set can be noted on each graph. It can be observed that the slope of a line increases as the graphene concentration increases. This is key, since the slope corresponds to the fracture toughness value, G_f, which also increasing.

In fig. 3.6, the size effect curves of the nominal stress are shown for each graphene percent weight concentration. The curves show the ideal curves for the nominal stress, based on the specimen size, D. It can be seen that the experimental values for each size at the specified concentration fit well into this data set. It is clear in these plots that the nominal stress is reduced as the specimen size increases. It can be noted that the overall trend of this data is that the maximum nominal stress is reduced as the concentration of graphene increases. It is also noticeable that the slope of the curves becomes less steep as the graphene concentration is increased.

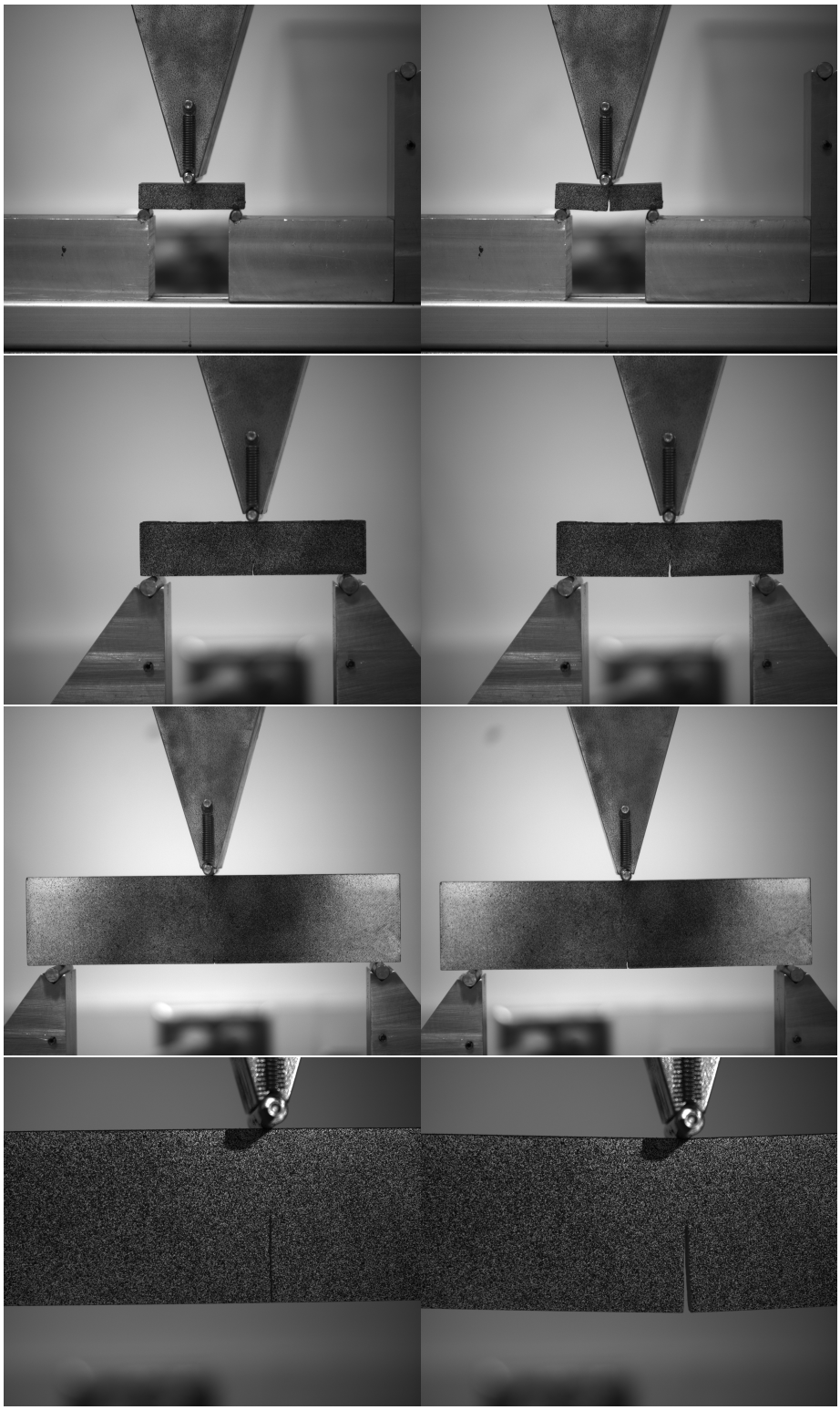

Figure 3.3: Four sizes of SENB test specimens, shown under two different load states

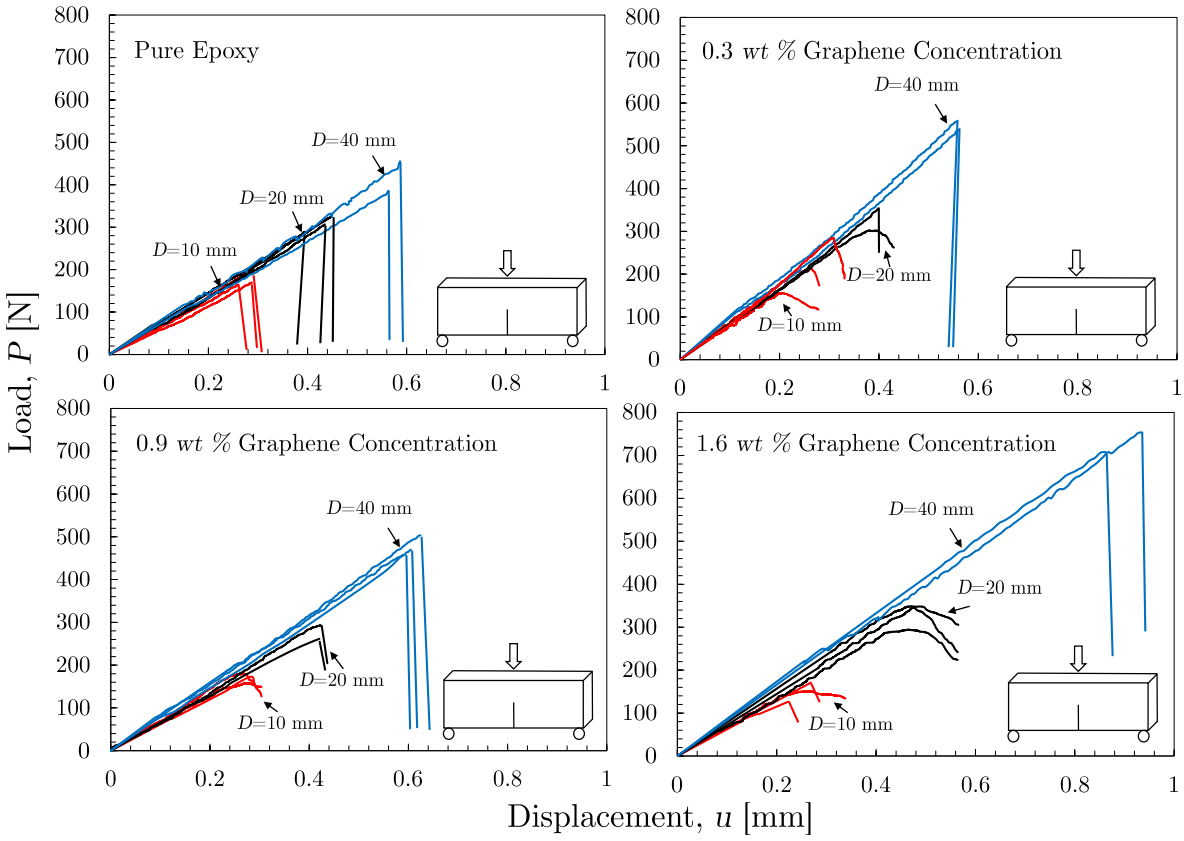

Figure 3.4: Load-displacement curves for different graphene concentrations and specimen sizes.

GC (wt%)	Specimen width (mm)	Crack length (mm)	Max load (N)	Nominal strength (MPa)
0	D=10	5.03	169.33	7.73
0	D=10	4.96	164.62	7.47
0	D=10	4.38	201.01	9.48
0	D=20	7.63	289.27	7.91
0	D=20	9.26	306.58	6.65
0	D=20	9.28	325.62	6.61
0	D=40	17.27	385.44	4.93
0	D=40	16.46	455.31	5.37
0.3	D=10	5.01	155.00	7.35
0.3	D=10	4.04	212.84	10.38
0.3	D=10	3.39	284.40	13.45
0.3	D=20	7.03	353.95	9.04
0.3	D=20	4.88	538.00	12.48
0.3	D=20	7.67	302.23	7.78
0.3	D=40	13.84	539.04	6.61
0.3	D=40	13.13	558.68	7.12
0.9	D=10	4.62	179.58	8.39
0.9	D=10	5.19	157.52	6.87
0.9	D=10	5.21	172.87	7.36
0.9	D=20	8.46	292.67	7.10
0.9	D=20	9.86	261.56	5.94
0.9	D=40	15.86	503.51	6.04
0.9	D=40	16.93	469.50	5.52
0.9	D=40	17.68	457.80	5.15
1.6	D=10	5.69	150.36	6.51
1.6	D=10	5.54	171.04	7.49
1.6	D=10	6.02	126.40	5.61
1.6	D=20	9.27	348.10	7.76
1.6	D=20	9.04	348.27	7.92
1.6	D=20	10.35	294.07	6.56
1.6	D=40	13.80	717.68	8.41
1.6	D=40	13.53	769.07	8.73

Table 3.3: Max load and nominal strength of specimens at different graphene concentrations.

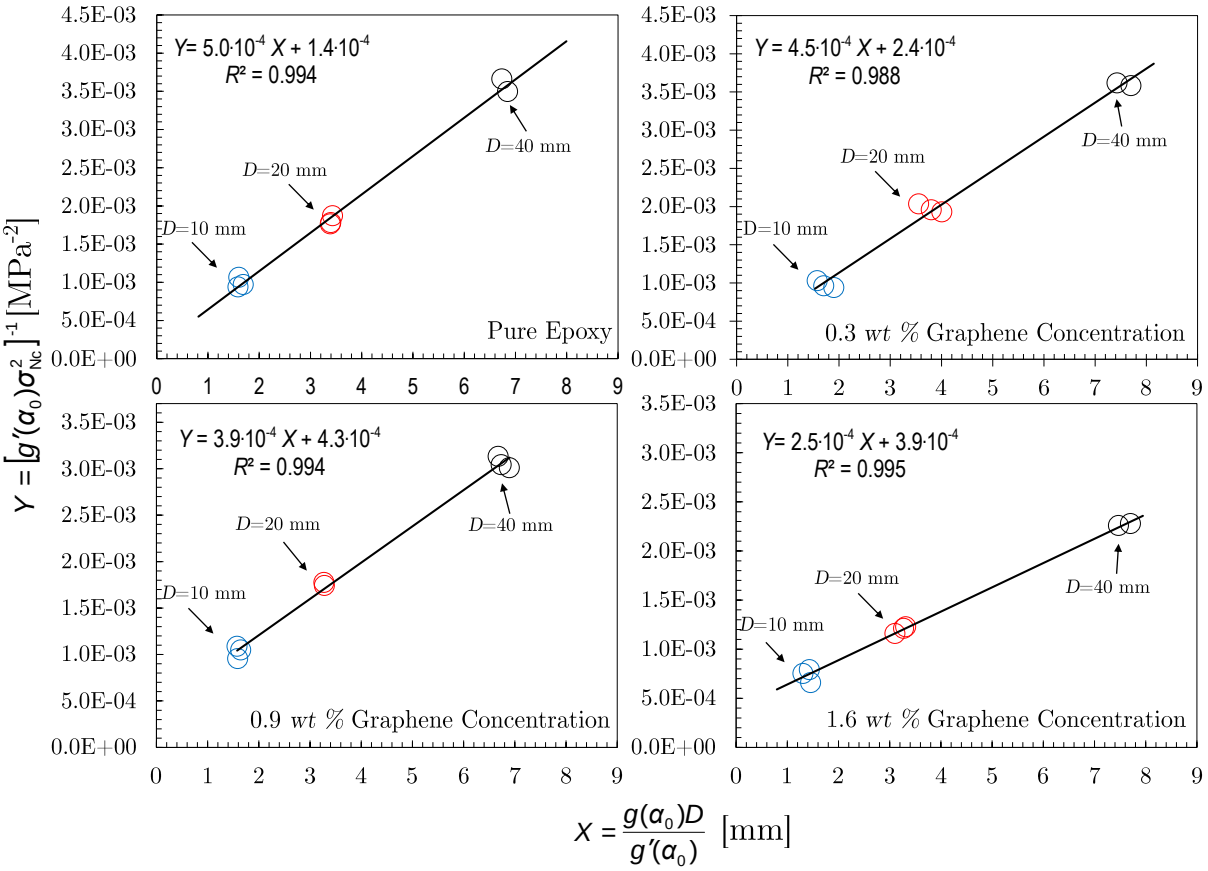

Figure 3.5: Single Edge Notch Bending Test Results

	0.00%wt	0.30%wt	0.90%wt	1.60%wt
G_f	0.880	0.911	1.06	1.69
c_f	0.283	0.546	1.10	1.58

Table 3.4: G_f and c_f changes as graphene concentration is increased

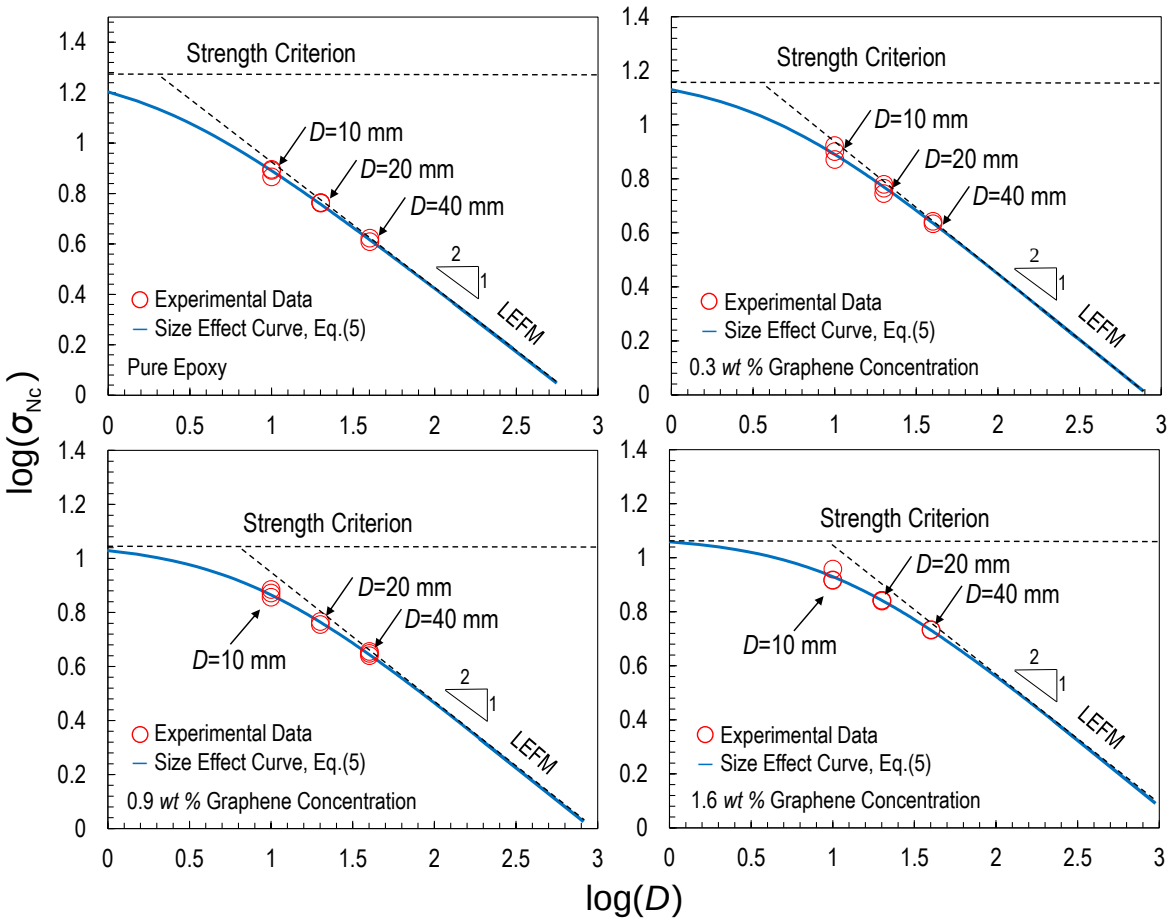

Figure 3.6: Size effect comparison of the experimental results from each size to three ideal models for the nominal stress

	$0.00\%wt$	$0.30\%wt$	$0.90\%wt$	$1.60\%wt$
$ln(D_0)$	0.255	0.540	0.843	1.00
D_0	1.80	3.47	6.97	10.1

Table 3.5: Comparison of specific size (D_0)

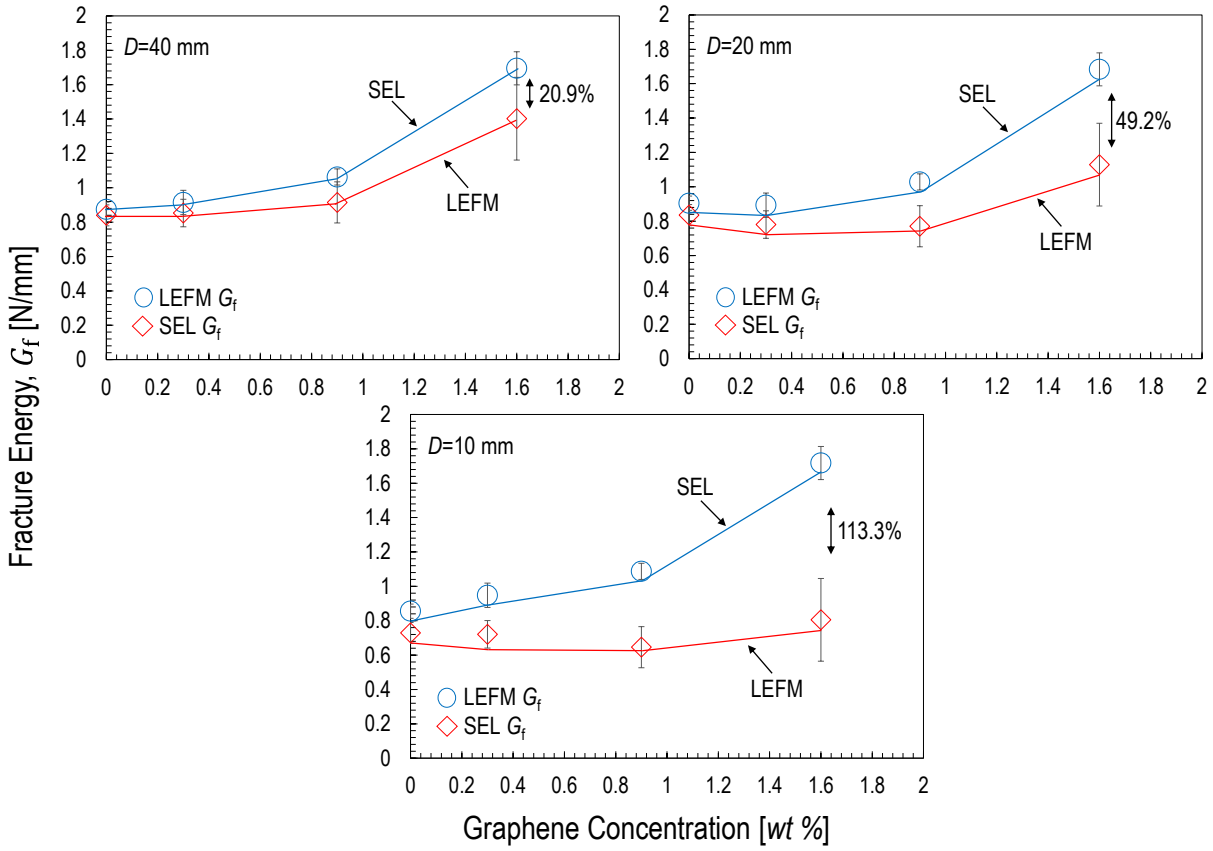

Figure 3.7: Fracture energy estimated from LEFM and SEL for several specimen sizes and graphene contents.

In fig. 3.7, this corrected calculation for G_f is compared to the traditional LEFM calculation of G_f. The values plotted are the average G_f values measured for all the specimen sizes tested, which were either calculated using LEFM or using the corrected method. The results show between a 9.4% and 44.9% increase in the G_f value, as seen in table 3.6. This shows that as the amount of graphene nanofiller is increased, the difference between the LEFM and the corrected values of G_f grows larger. This signifies that LEFM has trouble accurately predicting the behavior of nanocomposites, but it also seems to have a significant amount of error predicting the behavior of smaller specimens as the amount of filler increases.

Graphene $\%wt$	Average G_f LEFM	Average G_f Corrected	% Difference
0.00	0.796	0.878	9.82
0.30	0.776	0.919	16.8
0.90	0.778	1.05	29.7
1.60	1.08	1.70	44.9

Table 3.6: Percent difference between LEFM G_f compared to the Corrected G_f

3.3 SEM Analysis

Scanning Electron Microscope (SEM) imaging was performed in order to investigate the damage mechanisms that lead to the increase in mode I fracture energy of graphene nanocomposites. SEM images of the four test sample concentrations are pictured in fig. 3.9 and the differences between each concentration can be clearly observed. In fig. 3.9a it shows the plain epoxy specimen has some surface imperfections and dust but overall is relatively smooth. In fig. 3.9b-d they show the $0.3\%wt$, $0.9\%wt$ and $1.6\%wt$ specimens where you can clearly see the surface becomes rougher in texture as the graphene concentration increases. This rough fracture surface contains many smaller surfaces of different heights. This indicates that the crack extension path is more complex which leads to increased the fracture toughness measured [11, 47]. In fig. 3.8, the fracture modes for graphene sheets is shown and detailed in order to better illustrate what is occurring during crack propagation.

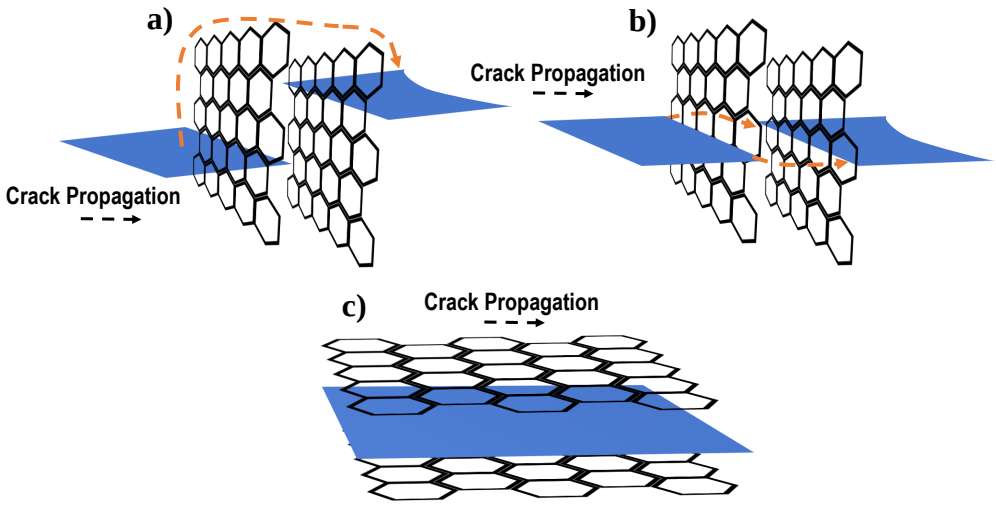

Figure 3.8: Schematic of the main damage mechanisms of graphene nanocomposites reported in this work: a) crack deflection; b) crack bifurcation/pinning; c) separation between graphene layers.

Higher magnification images in the propagation region are shown in fig. 3.10a-c for 0.9 wt% and 1.6 wt% graphene concentrations. Based on the pictures, the damage mechanisms are shown to be the following: a) microcrack deflection; b) microcrack pinning; and c) separation between graphene layers. As fig. 3.10a shows, crack deflection occurs when the crack front meets the surface of the graphene sheets and the crack is deflected leading to crack propagation around the graphene sheet into another plane. On the other hand, fig. 3.10b shows that when the crack front meets the surface of the graphene sheets, it becomes pinned and splits into two cracks. Finally, as shown in fig. 3.10c, when the crack front meets the edge of the graphene sheets, the crack continues to propagate in between the layers, splitting the agglomerate in two.

These damage mechanisms, schematically illustrated in 3.8, cause the crack to take a more torturous path thus requiring more energy to be released during the crack propagation. It is worth mentioning that similar damage mechanisms were reported by Chandrasekaran *et al.* [11, 21] for graphene nanocomposites and by Quaresimin *et al.* [40] and Zappalorto *et al.* [41,42]) for nanofillers of similar morphology.

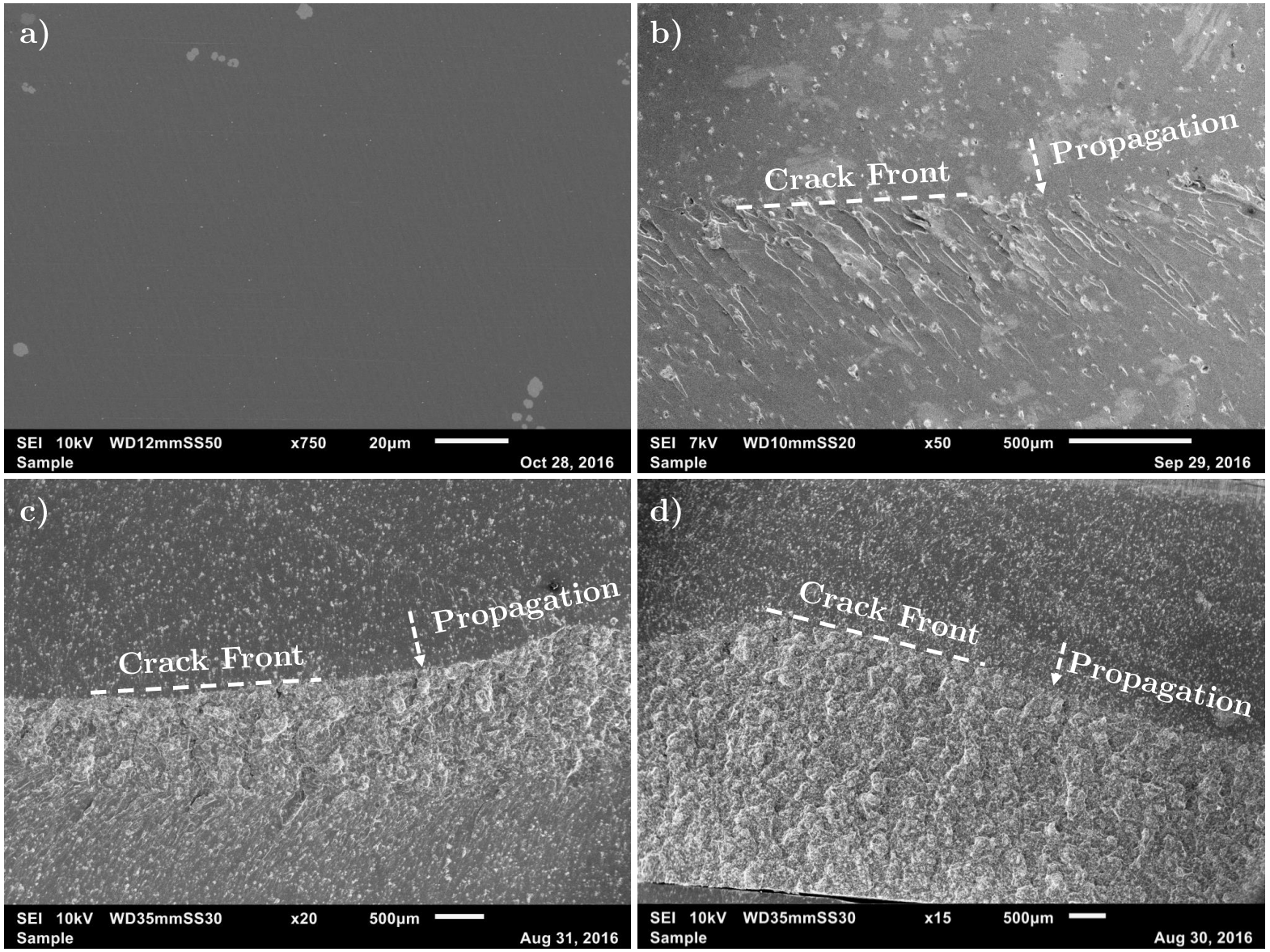

Figure 3.9: Fracture surfaces of specimens at different graphene concentrations: a) Pure epoxy; b) 0.3 wt%; c) 0.9 wt%; d) 1.6 wt%.

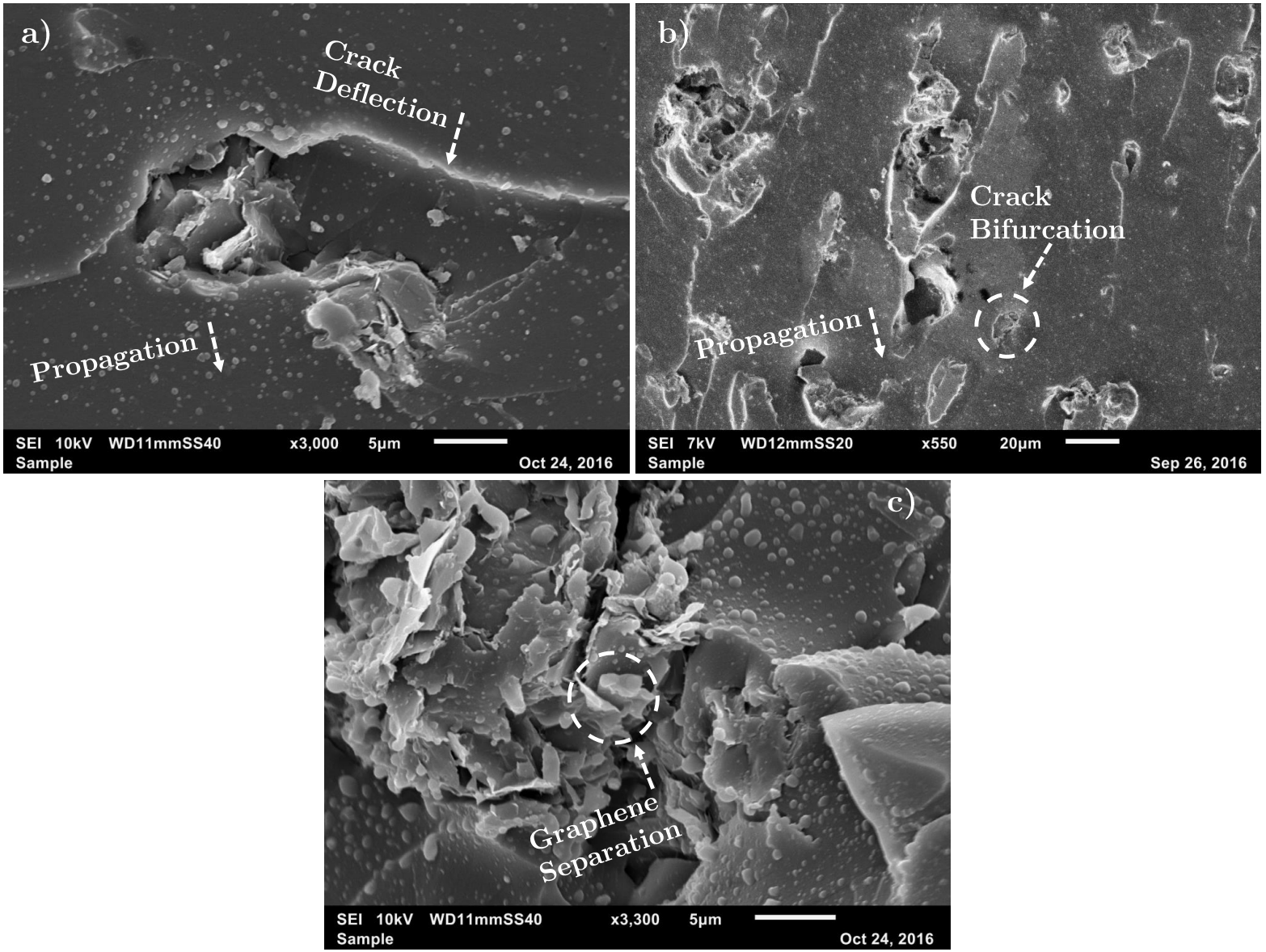

Figure 3.10: Damage mechanisms of graphene nanocomposites: a) crack deflection (1.6 wt% graphene concentration); b) crack pinning/bifurcation (0.9 wt% graphene concentration); c) separation between graphene layers (1.6 wt% graphene concentration).

Chapter 4

Data Analysis

As a result of the novel nature of this research, it is important to detail the specific calculations that were done to analyze the data for this experiment. Certain assumptions that are usually made in LEFM and in size effect calculations are being challenged and therefore the calculations done for this experiment need to be laid out explicitly.

4.1 Analysis of fracture tests by Size Effect Law (SEL)

The size of the non-linear Fracture Process Zone (FPZ) occurring in the presence of a large stress-free crack is generally not negligible. The stress field along the FPZ is nonuniform and decreases with crack opening, due to discontinuous cracking, micro-crack deflection, micro-crack pinning and graphene layer separations [11, 21]. As a consequence, the fracturing behavior and, most importantly, the energetic size effect associated with the given structural geometry, cannot be described by means of classical Linear Elastic Fracture Mechanics (LEFM). To capture the effects of a finite, non-negligible FPZ, the introduction of a characteristic (finite) length scale related to the fracture energy and the strength of the material is necessary [4, 27–30].

4.1.1 Size effect law for graphene nanocomposites

Let's consider an infinite plate subjected to a uniform remote stress and weakened by a crack of length 2a. According to linear elastic fracture mechanics (LEFM), the stress intensity factor can be written as,

$$K = \sigma\sqrt{\pi a} \tag{4.1}$$

Now, let's consider a plate with finite dimensions,

$$K = \sigma\sqrt{\pi a} f\left(\frac{a}{D}, \frac{a}{W}, t, ...\right) \tag{4.2}$$

where $\frac{a}{D}$ is the crack length versus width, $\frac{a}{W}$ is the crack length versus the height and t is the specimen thickness. This additional function can also take into consideration additional relevant system parameters which serves to better refine Equation eq. (4.2) to accurately represent the system.

Assuming plane strain, the relationship between stress intensity factor, K, and the energy release rate, G, is

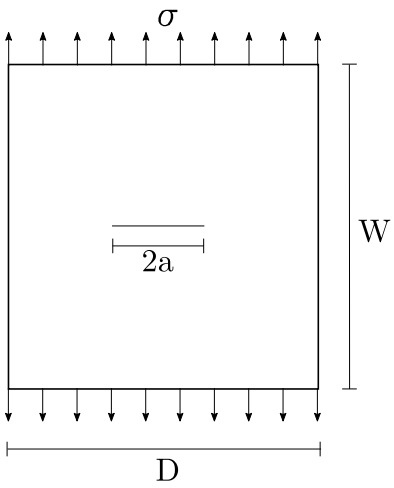

Figure 4.1: Finite Plate with a Set Initial Crack Length

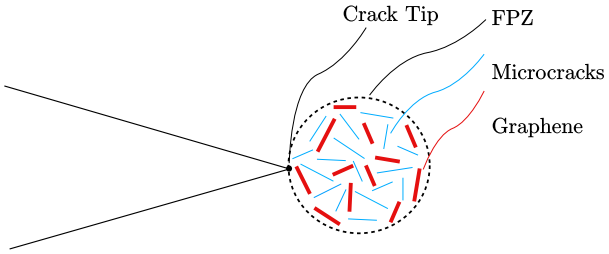

Figure 4.2: Crack Tip Detail and Fracture Progress Zone (FPZ)

$$G = \frac{K^2}{E}(1 - v^2) \tag{4.3}$$

These well understood equations have been in use effectively for many years. However, there is a problem with this equation when one is working with nanocomposites, which are quasi-brittle where they behave in a nonlinear manner. In Linear Elastic Fracture Mechanics (LEFM), when a specimen contains a crack, the assumption is made that the damage occurs at one point at the tip of the crack. In ductile materials there is a plastic zone that develops at the crack tip, which increases in size as the applied load increases until the crack grows and the material behind the crack tip unloads. This loading and unloading cycle near the crack tip leads to dissipation of energy. Similarly, the quasi-brittle nanocomposite specimen contains a Fracture Process Zone (FPZ), as shown in fig. 1.6. This zone contains microcracks scattered among the nanofiller in the material, and these microcracks can propagate throughout the rest of the sample. Depending on the size of the test specimen, this area is large by comparison. In other words, the FPZ is a material property that does not change and is independent the test specimen size. What changes is the ratio between the FPZ size and the specimen characteristic length, D. As the $\frac{FPZSize}{D} \to 0$ with $D \to \infty$ and $\frac{FPZSize}{D} \to \infty$ with $D >> 0$, meaning that the FPZ represents a larger and larger portion of the structure as the test specimen size decreases. Therefore, the role that the FPZ plays in the fracture behavior needs to be taken into account.

In order to incorporate this into the traditional equation, it is assumed that the crack length is longer than the original crack length of α_o. The new crack length is $\alpha_o + c_f$ where c_f is the length of the FPZ and is a material property that will be experimentally determined. Therefore, since $\alpha = \alpha_o + c_f$, from Equation eq. (4.2), we get

$$K = \sigma\sqrt{\pi(\alpha + c_f)}f\left(\frac{\alpha + c_f}{D}, \frac{\alpha + c_f}{W}, t, ...\right) \tag{4.4}$$

Combining Equations eq. (4.3) and eq. (4.4),

$$G(\alpha) = \frac{\sigma_N^2 \pi(\alpha + c_f)f^2}{E}(1 - v^2)$$

Substituting $g(\alpha) = \pi\left(\frac{\alpha}{D} + \frac{c_f}{D}\right)(1 - v^2)f^2$,

$$G(\alpha) = \frac{\sigma_N^2}{E^*} D g(\alpha) \tag{4.5}$$

where G is the energy release rate, $E^* = E$ for plane stress, $E^* = E/(1 - v^2)$, σ_N the nominal stress, and α is the ratio of the crack length compared to the width of the specimen,

$$\alpha = \frac{l}{D}$$

$$\alpha_o = \frac{l_o}{D}$$

where α_o is the total length of the crack and D is the width of the test specimen. The nominal stress is calculated by,

$$\sigma_N = \frac{3PL}{2tD^2}$$

where P is the applied load, L is the length, D is the width and t is the thickness of the specimen. From eq. (4.5), the failure condition can be written as,

$$G(\alpha_0 + c_f/D) = \frac{\sigma_N^2}{E^*} D g(\alpha_0 + c_f/D) = G_f \tag{4.6}$$

where G_f is the mode I fracture energy of the material and c_f is the effective FPZ length, which are both assumed to me material properties. This equation charaterizes the peak load conditions if $g'(\alpha) > 0$, i.e. only if the structure has positive geometry. Assuming $\frac{c_f}{D} << 1$, Equation eq. (4.6) can be Taylor expanded around α_o,

$$G(\alpha) = \frac{\sigma_N^2}{E^*} D \left(g(\alpha_o) + g'(\alpha_o)\frac{c_f}{D} + O\left[\frac{c_f}{D}\right]\right)$$

Neglecting H.O.T.,

$$\boxed{G(\alpha) = \frac{\sigma_N^2}{E^*} D \left(g_o(\alpha) + g_o'(\alpha)\frac{c_f}{D}\right)} \tag{4.7}$$

where $g_o = g(\alpha_o)$ and $g_o' = g'(\alpha_o)$. This approximation is always true for any load applied to the structure. Since graphene composites are quasi-isotropic, the same value E^* is used when looking at any direction in the test specimen. If the final load being applied is the critical load ($P = P_c$), $G = G_f$. G has become a material property and is independent of the value of α. The fracture energy can now be found by inverting Equation eq. (4.7) to get,

$$\sigma_N^2 = \frac{E^* G_f}{D g_o + c_f g_o'}$$

$$\Downarrow$$

$$\sigma_{Nc} = \sqrt{\frac{E^* G_f}{D g_o + c_f g_o'}} \tag{4.8}$$

where $g'(\alpha_0)$ $=\mathrm{d}g(\alpha_0)/\mathrm{d}\alpha$. The only unknown values above are c_f and G_f. The σ_N will be determined experimentally and the g_o will be found through finite element analysis. All other values are known quantities about the structure. This equation relates the nominal strength of radially scaled structures to a characteristic size, D and it can be rewritten in the following form,

$$\sigma_{Nc} = \frac{\sigma_0}{\sqrt{1 + D/D_0}} \tag{4.9}$$

where $\sigma_0 = (E^* G_f / c_f g'(\alpha_0))^{0.5}$ and $D_0 = c_f g'(\alpha_0)/g(\alpha_0) =$ constant, depending on both FPZ size and specimen geometry. Contrary to classical LEFM, eq. (4.9) is endowed with a characteristic length scale D_0. This is key to describe the transition from ductile to brittle behavior with increasing structure size reported in the fracture tests.

4.1.2 Fitting experimental data to SEL

Graphing the relationship between the nominal stress (σ_N) and the width of the test sample (D) is done through a logarithmic plot. From Equation section 6.1,

$$ln(\sigma_N) = ln\left(\frac{EG_f}{Dg_o + c_f g_o'}\right)^{\frac{1}{2}} = ln\left(\frac{Dg_o + c_f g_o'}{EG_f}\right)^{-\frac{1}{2}}$$

$$= -\frac{1}{2}\left[ln(Dg_o + c_f g_o') - ln(EG_f)\right]$$

$$= -\frac{1}{2}\left[ln\left[D\left(g_o + \frac{c_f}{D}g_o'\right)\right] - ln(EG_f)\right]$$

$$\boxed{ln(\sigma_N) = -\frac{1}{2}ln(D) - \frac{1}{2}ln\left(g_o + \frac{c_f}{D}g_o'\right) + \frac{1}{2}ln(EG_f)} \tag{4.10}$$

$$\boxed{ln(\sigma_N) = -\frac{1}{2}ln(D) - \frac{1}{2}ln(g_o) + \frac{1}{2}ln(EG_f)} \tag{4.11}$$

Eq. 4.11 assumes that $D >> c_f$. If this relationship is not true for the test sample, you have the general equation, seen in eq. 4.10.

To find a first estimate of the stress needed to fracture the coupon, it was assumed that $E = 3000MPa$ and $\sigma_t^2 = 70MPa$, which means

$$G_f = 0.6\frac{N}{mm}$$

$$c_f = 0.44\frac{EG_f}{\sigma_t^2}$$

Precracking by tapping is the only accurate approach to test the polymer fracture toughness, since the radius of curvature at the notch tip seems to play an important role, despite of what LEFM suggests (see section 7.1). The specimens were designed and made in four geometrically scaled sizes.

The actual values of G_f and c_f can be determined by regression analysis of the experimental data. Assuming geometrically scaled structures, Bažant *et al.* [4] proposed to define the following,

$$X = D, \quad Y = \sigma_{Nc}^{-2} \tag{4.12}$$

$$\sigma_0 = C^{-1/2}, \quad D_0 = \frac{C}{A} = \frac{1}{A\left(\sigma_0\right)^2} \tag{4.13}$$

thanks to which, eq. (4.9) can now be expressed in the following linear form,

$$Y = Ax + C \tag{4.14}$$

Eq. (4.14) can be used to perform a linear regression analysis of the size effect data provided that all the specimens are scaled exactly (i.e. $g(\alpha_0)$ and $g'(\alpha_0)$ take the same values for all the tests). This implies that all the specimens of different sizes have the same normalized crack lengths.

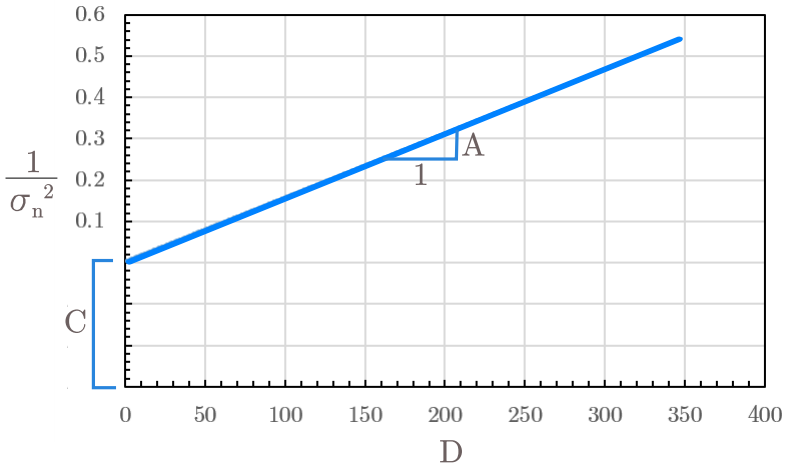

However, since the initial cracks for the nanocomposites were created by tapping to avoid residual stresses at the crack tip [43, 44], a perfect scaling could not be guaranteed. To overcome this issue, in this study, eq. (4.14) was rearranged as follows,

$$\frac{1}{g'(\alpha)\sigma_{N_c}^2} = \frac{g(\alpha)}{g'(\alpha)EG_f}D + \frac{c_f}{EG_f}g'(\alpha) \Longleftrightarrow y = Bx + M \tag{4.15}$$

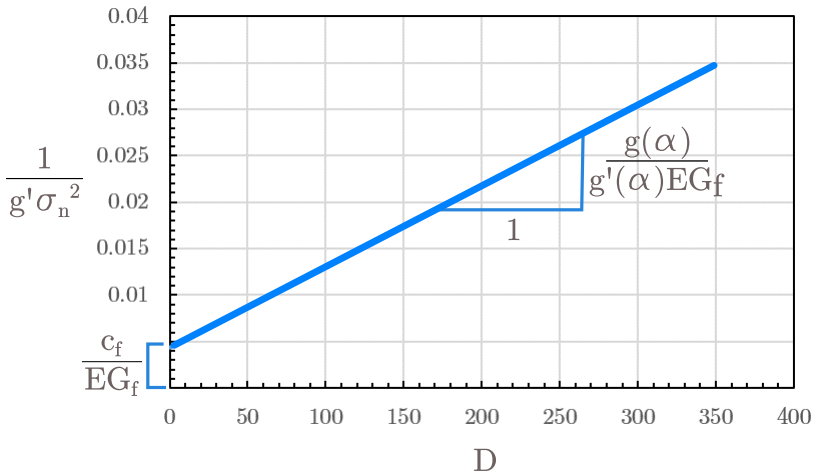

where now $X = g(\alpha_0)D/g'(\alpha_0)$, $Y = \left(g'(\alpha_0)\sigma_{Nc}^2\right)^{-1}$, $B = (E^*G_f)^{-1}$, and $M = c_f/E^*G_f$. Following section 4.1.2, a linear regression analysis was conducted for all the graphene concentrations as represented in fig. 3.5 and the parameters B and M, reported in fig. 3.5a-d, could be estimated for all the graphene concentrations.

It is interesting to note that the slope B of the regression curve decreases significantly with increasing concentrations of graphene whereas the intercept M shows an opposite trend. As can be noted from the expressions of B and M, a milder slope denotes a higher mode I fracture energy thus confirming a toughening effect of the graphene nanoplatelets. Conversely, for increasing fracture energies, a higher value of the intercept indicates an increasing size of the effective Fracture Process Zone (it is worth mentioning here that the case of a material with negligible FPZ, as assumed by LEFM, corresponds to regression lines passing through the origin). This suggests an increasing ductility of the material system with increasing graphene content.

4.2 Estimation of fracture properties by SEL

The parameters of the size effect law, B and M, can be directly related to the mode I fracture energy of the material, G_f and the effective FPZ size, c_f as follows:

$$G_f = \frac{1}{E^* B}, \quad c_f = \frac{M}{B} \tag{4.16}$$

provided that the functions $g(\alpha)$ and $g'(\alpha) = \mathrm{d}g(\alpha)/\mathrm{d}\alpha$ and the elastic modulus E^* are known. The mode I fracture energy G_f and the effective FPZ length c_f estimated by means of eq. (4.16)a,b are tabulated in Table 3.4 whereas the calculation of $g(\alpha)$ and $g'(\alpha)$ is discussed in the next section.

It is worth noting here that, indeed, the addition of graphene led to an enhancement of the mode I fracture energy which increased from 0.880 N/mm for the pure epoxy case to 1.693 N/mm for the 1.6 wt% case, a 92.4% improvement. On the other hand, the addition of graphene caused a larger FPZ size which changed from 283 μm to 1587 μm. This latter aspect is of utmost importance: while the inherent assumption of LEFM of a negligible FPZ seems reasonable for the pure epoxy case, this is not true for graphene-modified specimens which show a FPZ about one order of magnitude larger and not negligible compared to e.g. the specimen width. This is in agreement with the results obtained by Salviato *et al.* for other nanocomposite systems by means of multi-scale analytical models [48–56].

The importance of the finiteness of the FPZ for the estimation of nanocomposite fracture energy and its consequences on the structural scaling will be the subject of section 4.5.

4.3 Determining G, g and g'

The model of one of the specimens was made to scale in ABAQUS, where a total of 33,394 nodes and 11,003 elements were used to create an accurate mesh. This mesh had a much higher concentration of nodes and elements around the crack tip to ensure high accuracy of the results. A crack 0.5α was simulated into the model as well and simulations were done to predict the behavior of specimen and the critical load for each specimen size. Since all of the sizes are geometrically scaled, only one size needed to be simulated. These models in ABAQUS also were used to determine the J-integral which was used to calculate g and g'.

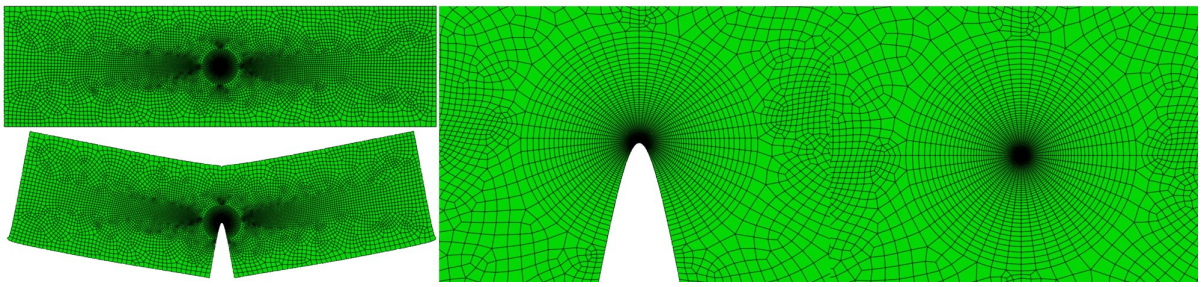

Figure 4.3: ABAQUS Mesh for Single Edge Notch Specimen and Crack Detail

The J-integral [57] is an approach to describe the failure condition of a system. In linear elastic fracture mechanics (LEFM) the J-integral coincides with the energy release rate and in non-linear fracture mechanics, it provides a measure of the energy required to propagate a crack.

In 2D, the J-Integral is:

$$J = \int_\tau \left(W dx_2 - t \frac{\delta u}{\delta x_1} ds \right) = \int_\tau \left(W dx_2 - t_i \frac{\delta u_i}{\delta x_1} ds \right) \tag{4.17}$$

Where,

$W(x_1, x_2)$ is strain energy density
$t = [\sigma]n$ is surface traction vector
n is normal to the curve τ
$[\sigma]$ is Cauchy stress tensor
u is displacement vector

It is important to note that the J-integral will be zero over a closed path. It is also path independent, meaning that it does not depend on the path of integration around the crack tip. Therefore, the value of the J-integral calculated on any path around the crack tip is equal to the energy release rate (G). The result of the J-integral gives the value of G at the crack length modeled directly, since the result of the J-integral on any path around the crack tip is equal to the energy release rate $J = G$. From this value of G, the value for g can be calculated by rearranging the below equation for $G(\alpha)$,

$$G(\alpha) = \frac{\sigma_N^2}{E} D g(\alpha)$$

Where,

$\alpha = \frac{a}{D}$ is the crack length divided by the width of the specimen
σ_N is the nominal stress
E is the elastic modulus
D is the specimen width

Rearranging the above equation,

$$g(\alpha) = \frac{G(\alpha) E}{D \sigma_N^2}$$

To determine $g' = \frac{dg}{d\alpha}$ at a specific value of alpha, the crack length was changed very slightly to make it shorter and longer than the desired value for alpha. At each of these values, the J-integral was recalculated. These values for G were then plotted against the corresponding value for alpha. The slope of this line is equal to the value of g'. The final values calculated are shown in the table below and more detailed images of the meshes created in ABAQUS can be found in fig. 7.5.

α	G	g	g'
0.495	0.0911	2.70	
0.500	0.0940	2.79	17.7
0.505	0.0971	2.88	

In addition, predictive plots for g and g' were created, as shown below, in fig. 4.4.

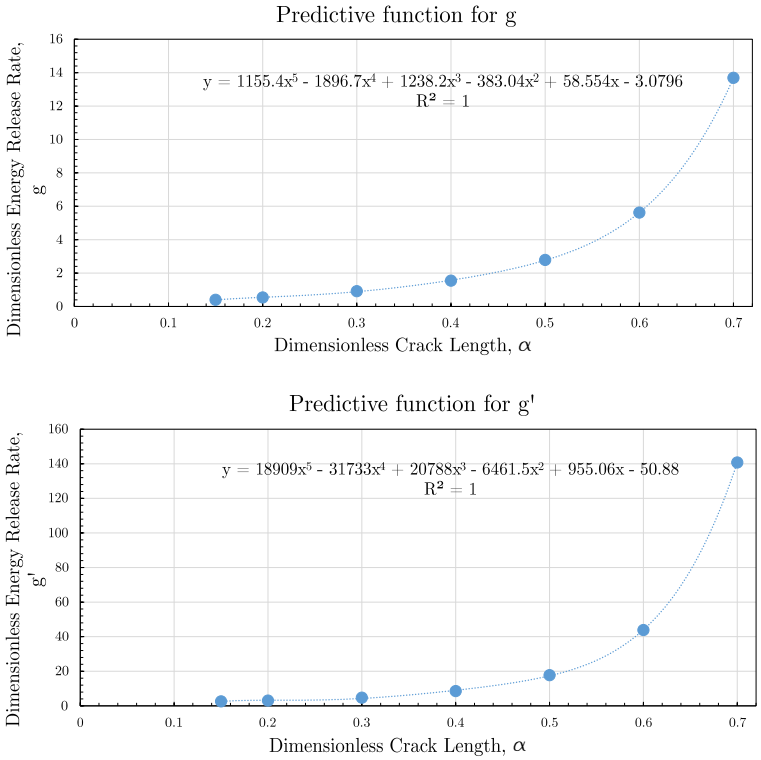

Figure 4.4: Predictive functions for g and g'

4.4 Size effect analysis

To investigate the scaling behavior of structural strength, it is interesting to analyze perfectly radially scaled specimens of different sizes. Now that the fracture properties of the various material systems are known, it is possible to estimate the structural strength for a given normalized crack length starting from the experimental data. In fact, let us consider a crack length of $0.5D$ for all the specimen sizes. One can relate the experimental results, calculated for crack lengths close to $0.5D$ but not exactly $0.5D$, to the desired case by imposing that the energy release rate at failure is G_f in both cases:

$$\frac{\sigma_{Nc,exp}^2 D}{E^*}\left[g(\alpha_{0,exp}) + \frac{c_f}{D}g'(\alpha_{0,exp})\right] = \frac{\sigma_{Nc,desired}^2 D}{E^*}\left[g(0.5) + \frac{c_f}{D}g'(0.5)\right] \tag{4.18}$$

This leads to the following expression for the adjusted nominal strength:

$$\sigma_{Nc,desired} = \sigma_{Nc,exp}\sqrt{\frac{Dg(\alpha_{0,exp}) + c_f g'(\alpha_{0,exp})}{Dg(0.5) + c_f g'(0.5)}} \tag{4.19}$$

The experimental data adjusted according to 4.19 and the fitting by SEL are shown in fig. 3.6a-d where the structural strength σ_{Nc} is plotted as a function of the structure size D in double logarithmic scale. In such a graph, the structural scaling predicted by LEFM is represented by a line of slope $-1/2$ whereas the case of no scaling, as predicted by stress-based failure criteria, is represented by a horizontal line. The intersection between the LEFM asymptote, typical of brittle

behavior, and the plastic asymptote, typical of ductile behavior, corresponds to $D = D_0$, called the *transitional size* [4].

As can be noted from fig. 3.6a, the experimental data related to the pure epoxy system all lie very close to the LEFM asymptote showing that, for the range of sizes investigated in this work (or larger sizes), linear elastic fracture mechanics provides a very accurate description of fracture scaling. This confirms that, for the pure epoxy and sufficiently large specimens, the FPZ size has a negligible effect and LEFM can be applied, as suggested by ASTM D5045-99 [32]. However, this is not the case for graphene nanocomposites which, as fig. 3.6b-d show, are characterized by a significant deviation from LEFM, the deviation being more pronounced for smaller sizes and higher graphene concentrations. In particular, the figures show a transition of the experimental data from stress-driven failure, characterized by the horizontal asymptote, to energy driven fracture characterized by the $-1/2$ asymptote. This phenomenon can be ascribed to the increased size of the FPZ compared to the structure size which makes the non-linear effects caused by micro-damage in front of the crack tip not negligible. For sufficiently small specimens, the FPZ affects the structural behavior and causes a significant deviation from the scaling predicted by LEFM with a much milder effect of the size on the structural strength. On the other hand, for increasing sizes, the effects of the FPZ become less and less significant thus leading to a stronger size effect closely captured by LEFM. Further, comparing the size effect plots of nanocomposites with different graphene concentrations, it can be noted a gradual shift towards the ductile region thus showing that not only the addition of graphene leads to a higher fracture toughness but also to a gradually more ductile structural behavior for a given size.

The foregoing conclusions are extremely important for the design of graphene nanocomposite structures or electronic components. As the experimental data show, LEFM does not always provide an accurate method to extrapolate the structural strength of larger structures from lab tests on small-scale specimens, especially if the size of the specimens belonged to the transitional zone. In fact, the use of LEFM in such cases may lead to a significant underestimation of structural strength, thus hindering the full exploitation of graphene nanocomposite fracture properties. This is a severe limitation in several engineering applications such as e.g. aerospace or aeronautics for which structural performance optimization is of utmost importance. On the other hand, LEFM always overestimates significantly the strength when used to predict the structural performance at smaller length-scales. This is a serious issue for the design of e.g. graphene-based MEMS and small electronic components or nanomodified carbon fiber composites in which the inter-fiber distance occupied by the resin is only a few micrometers and it is comparable to the FPZ size. In such cases, SEL or other material models characterized by a characteristic length scale ought to be used.

4.5 LEFM vs. SEL for the estimation for the fracture properties of nanocomposites

Having discussed the scaling of the fracturing behavior and having shown that, for graphene nanocomposites, the FPZ is not negligible for the range of specimen sizes investigated, it is interesting to check how the mode I fracture energy calculated through SEL compares to the estimation from LEFM for the various sizes and graphene contents.

The fracture energy can be calculated by means of LEFM as follows:

$$G\left(\alpha_0\right) = \frac{\sigma_N^2 D}{E^*} g(\alpha_0) \tag{4.20}$$

where all the quantities and functions have the same meaning discussed in previous sections but, different from SEL, the FPZ length is not accounted for. fig. 3.7a-c show a comparison between

the fracture energy estimated by SEL and by LEFM for different specimen sizes and graphene concentrations. As can be noted, for a given size, the difference between SEL and LEFM increases with the amount of graphene with LEFM underestimating G_f. The difference increases with the addition of graphene since, as shown in previous sections, the FPZ size increases monotonically and thus the cardinal assumption of LEFM becomes less and less accurate. The underestimation caused by LEFM can be very significant if one considers that the maximum difference, occurring at 1.6 wt% for all sizes, is 20.9%, 49.2% and even 113.3% for the large, medium and small sizes respectively. More importantly, a serious issue about using LEFM when the specimen sizes belong to the transitional region is that the estimate is not objective, i.e. it does depend on the size of the specimen tested. This can be noted from fig. 3.7a-c which show that, for a given graphene content, the fracture energy estimated by LEFM is size dependent, being lower for smaller sizes. It is interesting to note that, for example, the calculations based on LEFM for 1.6 wt% nanocomposites show basically no increment in the fracture energy for the small size specimen while, for the large size, the increment is about 50%. Conversely, thanks to the characteristic length scale associated with the FPZ size, SEL provides the same estimate of the fracture energy for all the sizes. Of course, the size dependence of the fracture energy estimated by LEFM and its difference from SEL depends on the range of sizes investigated: for sufficiently large specimens, both the theories provide the same, size independent, fracture energy. However, as will be shown in a following publication, most of the tests on nanocomposites reported in the literature were performed on small specimens belonging to the transitional region between ductile and brittle behavior. This may explain why the range of fracture energy increments obtained by nanomodification reported in the literature is so large: neglecting the effects of the non-linear FPZ lead to fracture energy estimates which were size dependent and consistently underestimating, the underestimation being more significant for larger nanofiller concentrations and smaller specimen sizes.

4.6 Study of applicability of LEFM to polymer nanocomposites

The ASTM D5045-99 provides a lower limit for $(D - a)$ to guarantee a plane strain condition. According to the standard:

$$(D - a) \geq 2.5(K_{IC}/\sigma_y)^2 \tag{4.21}$$

where D is the specimen width, a is the crack length, K_{IC} is the fracture toughness, and σ_y is the yielding stress. Even if this limit is suggested for a different purpose, it is interesting to check if it would be enough to guarantee the use of LEFM to estimate the fracture energy of the material for the graphene nanocomposites investigated in this work. To this end, Eq. (4.21) is compared to the width D_{cr} which would be required to guarantee a difference between the nominal strength predicted by LEFM and SEL lower than 10%. Accordingly, the lower limit of D can be calculated as follows:

$$\sqrt{\frac{EG_f}{D_{cr}g(\alpha_0) + c_f g'(\alpha_0)}} = 0.9\sqrt{\frac{EG_f}{D_{cr}g(\alpha_0)}} \tag{4.22}$$

Finally, rearranging Eq. (4.22), the lower bound D_{cr} can be expressed in the following general form:

$$D_{cr} = 4.263\frac{g'(\alpha_0)}{g(\alpha_0)}c_f \tag{4.23}$$

A comparison between the standard ASTM D5045-99 and SEL for the case in which the crack length is half the width D of the specimen is reported in Table 4.1 by using an average Poisson's ratio of 0.4 for all the graphene concentrations.

Graphene concentration (wt%)	ASTM D5045-99 (mm)	Size effect curve (mm)
0	$D > 4.45$	$D > 7.70$
0.3	$D > 4.60$	$D > 14.80$
0.9	$D > 5.62$	$D > 29.71$
1.6	$D > 9.97$	$D > 43.04$

Table 4.1: ASTM D5045-99 and SEL for the limitations of size criteria on SENB specimens.

According to Table 4.1, the difference between ASTM D5045-99 and size effect curve can be significant depending on the graphene content. For the highest graphene content and the geometry investigated in this study, D_{cr} (the width providing a difference between LEFM and SEL of 10% only) would be in the order of 40 mm. This limit is significantly reduced for the pristine epoxy, with LEFM being valid for widths larger than approximately 7 mm. For both cases, the value calculated from the standard is always lower with $D_{cr} = 9.97$ mm and 4.45 mm for the 1.6 wt% and pure epoxy specimens respectively.

Chapter 5

Discussion of Experimental Results

The predominant reason for exploring the use of nanofillers for use with epoxy was to find a filler that would make the epoxy matrix stronger, but not take the place of actual fiber reinforcement. The purpose for the strengthened matrix material is to be used in conjunction with carbon fiber reinforcements to create an overall stronger composite material. Fillers offer a opportunity to add strength without adding a great deal of weight, which is especially applicable in the design of aerospace structures. Through this experiment, graphene has shown great success as a nanofiller, with many improvements in fracture toughness without increasing the elastic modulus.

The tensile testing provided a great deal of information about the behavior and mechanical properties of the graphene/epoxy composite material. This is partially because a wider range of graphene concentrations were able to be tested with the dogbone specimens since they are smaller and easier to manufacture. The first item determined through these tests was the maximum engineering and true stresses. It was shown that there wasn't a great deal of variation of this material property over the course of the experiment, if you take the amount of error into consideration. It was also shown that the elastic modulus varies between different filler concentrations, but that there is very little overall change, when error is considered. These are very good results but because they show that adding the filler does not weaken the epoxy, since the true and engineering stresses and the elastic modulus are almost unchanged, as filler is added. In addition, the specimens were tested at two different rates yet the results for the elastic modulus and the stresses are very similar, which means that the displacement rate does not have a large effect on theses results.

Lee, Ikeda, Miyazaki and Choi [13] found that the fracture toughness, K_{1c}, is directly proportional to the energy release rate, G_f. This finding has been replicated in my results. The SENB results shown in fig. 3.5 demonstrate that the graphene has indeed increased the fracture toughness of the epoxy. The slope of the best fit line progressively increases as the graphene percent weight increases. This indicates that the fracture toughness, K_{1c}, is increasing, meaning the material is becoming more resistant to cracking as the nanofiller concentration increases. The general trend is that as the nominal stress and c_f increases, the K_{1c} also increases. Crack inhibition is also shown to be occurring with the steady increase in the fracture energy, G_f as the graphene nanofiller concentration increases. The electron microscope imaging clearly shows many instances of microcracks passing through the material, coming into contact with a graphene sheet, and moving around it, which clearly demonstrates that crack inhibition is occurring. This is consistent with the idea that the more filler that is in the material, the greater the distance the crack needs to travel in order to go through the whole material, thus increasing the value of G_f. In fig. 3.9, it can be observed that the material at $1.6\%wt$ graphene is far rougher in texture than that of $0.3\%wt$ graphene. You can also see more instances of graphene sheet pullout and rupture of graphene sheets

as a result of interfacial adhesion. As mention earlier, this rough fracture surface contains smaller surfaces of varying heights, which indicates a more complex crack extension path, which leads to a higher K_1c measured value.

It is also unclear whether $1.6\%wt$ is the optimum graphene concentration, since testing beyond this amount was not conducted. The general trend is that after a certain concentration, the occurrence of defects and agglomerations outweighs the beneficial crack inhibition properties, and the mechanical properties deteriorate as a result. Further study needs to be done to determine what this critical concentration is for this particular epoxy matrix.

This experiment also demonstrated that size effect corrected method is more accurate when analyzing nanocomposites versus using the LEFM method. In fig. 3.5 it shows that for each of the three specimen sizes analyzed, there is good grouping of the results and the slope of the best fit line increases, meaning that the fracture energy and the size of the fracture process zone is increasing. This fracture process zone increase means that the area of microcracking in proportion to the area of the specimen is also increasing. It can also be observed that the nominal stress decreases as the specimen size and the graphene percent weight increases. The experimental results closely fit the ideal size effect trend shown in fig. 3.6. This directly shows that size effect as a model accurately describes the relationship between the specimen size and the nominal stress measured. As fig. 3.7 and table 3.6 show, the difference between the LEFM and corrected fracture energy results was between $20.9\% - 113.3\%$, meaning that the LEFM prediction under estimates the fracture energy by this amount.

The key to LEFM analysis is the assumption that the area at the tip of a crack is infinitely small, which means that the force at the crack tip is approaching infinity. Now taking the FPZ area into account, we can see that if the specimen is sufficiently large compared to the size of the FPZ, the assumption that the crack tip area is negligible can be made, knowing there will be a slight amount of error. However, if the the area of the FPZ is large compared to the size of the specimen, then the FPZ area is no longer negligible and must be taken into account in the analysis in order to receive accurate results. D_0 is the minimum specimen width after which LEFM can be used to approximate the results, knowing there will be varying degrees of error. As can be noted in fig. 3.6, the value for D_0 increases as the percent weight of graphene increases. This signifies that the specimens that are tested need to be larger and larger as the amount of nanofiller is increased to remain in the LEFM testing range. In mechanical testing, one wants to be able to test as small of a specimen as possible to get accurate results. This means that as more filler is added, one needs to test larger specimens to get accurate results. It can also be noted tat the fit between the ideal corrected model and the LEFM model gets worse as the percent weight of the nanofiller is increased, which means that even if you do choose to use the LEFM method, the ability for your experimental data to properly fit your LEFM prediction will be greatly diminished, with potentially great errors. These errors mean that the researcher would be overestimating the nominal stress in their test specimens, which means the fracture energy calculated would be much lower than what is actually occurring. These results can be seen in fig. 3.7. That means that the LEFM method is not very accurate at predicting behavior even in the plain epoxy.

Chapter 6

Analysis of Literature Data

6.1 Data Analysis

This improved method for calculating G_f works in other data sets, the results from other studies were extracted and reanalyzed using both the "LEFM" method and the corrected method. It is anticipated that the corrected method will greatly improve the results in situations where a small test specimen was used, but that the results will remain very similar between the two methods if the test specimen is larger.

The studies that were chosen tested nanoparticles and their effectiveness in epoxy resins using either single edge notch (SENB)or compact tension (CT) test methods. The information needed from each study was the percent weight of the filler ($\%wt$), young's modulus (E), ultimate stress (f_t), and the fracture energy (G_f) according to LEFM. If specific values were not provided for these parameters, it was assumed that $E = 3000MPa$ and $f_t = 50MPa$. The value for G_f using LEFM was calculated using the following equation, when not explicitly provided in the article being reviewed:

$$G_{f_{LEFM}} = \frac{K^2}{E}(1 - v)$$

The corrected value of G_f was derived by combining the following equations:

$$G_f = \frac{\sigma_N^2}{E} D \left(g_0 + g_0' \frac{c_f}{D} \right) \tag{6.1}$$

$$c_f = 0.44 \frac{EG_f}{f_t^2} \tag{6.2}$$

$$G_{f_{LEFM}} = \frac{\sigma_n^2}{E} D g_0 \tag{6.3}$$

$$\sigma_n^2 = \frac{EG_{f_{LEFM}}}{D g_0} \tag{6.4}$$

Combining equation 6.1 and equation 6.2,

$$G_f = \frac{\sigma_N^2}{E} D \left(g_0 + g_0' \frac{0.44 EG_f}{D f_t^2} \right)$$

$$G_f = \frac{\sigma_N^2}{E} D g_0 + \frac{\sigma_N^2}{E} D g_0' \frac{0.44 EG_f}{D f_t^2}$$

substituting in equation 6.3 and simplifying,

$$G_f = G_{f_{LEFM}} + \frac{0.44\sigma_N^2 g_0' G_f}{f_t^2}$$

$$G_f \left(1 - \frac{0.44\sigma_N^2 g_0'}{f_t^2}\right) = G_{f_{LEFM}}$$

substituting in equation 6.4 and rearranging to solve for G_f,

$$G_f \left(1 - \frac{0.44 g_0'}{f_t^2} \frac{E G_{f_{LEFM}}}{D g_0}\right) = G_{f_{LEFM}}$$

$$\boxed{G_{f_{Corrected}} = \frac{G_{f_{LEFM}}}{1 - \left(\frac{0.44 G_{f_{LEFM}}}{D f_t^2} \frac{E g_0'}{g_0}\right)}}$$

The same g_0 and g_0' values calculated previously for this study were used to calculate the results for the papers which also used single edge notch as their testing method. To calculate the g and g' values for the compact tension specimens, it is first important to show how the nominal stress (σ_N) is defined, since it is different than what is used for single edge notch specimens. The nominal stress is defined as the pressure experienced by the hole in the specimen. Mathematically, the nominal stress is defined as,

$$\sigma_N = \frac{P}{tD} \tag{6.5}$$

where $D = W/4$ according to ASTM Standard D5045-99 [32]. Therefore,

$$\sigma_N = \frac{P}{t\frac{W}{4}} \Longrightarrow P = \sigma_N \frac{W}{4} t \tag{6.6}$$

$$K_{1c} = \frac{P}{t\sqrt{W}} f(\alpha) \tag{6.7}$$

Where $\alpha = a/W$ and a is the crack length and W is the width of the specimen. Placing Equation 6.6 in Equation 6.7

$$K_{1c} = \frac{\sigma_N \frac{W}{4} t}{t\sqrt{W}} f(\alpha) = \frac{W\sigma_N}{4\sqrt{W}} f(\alpha) \tag{6.8}$$

$$G_{1C} = \frac{K_{1c}^2}{E}(1 - v^2) = \frac{W\sigma_N^2}{16E} f(\alpha)^2 (1 - v^2) \tag{6.9}$$

Since,

$$G = \frac{W\sigma_N^2}{E} g(\alpha) \Longrightarrow g(\alpha) = \frac{f(\alpha)^2(1 - v^2)}{16} \tag{6.10}$$

Every other value is known for the compact tension specimens except for $f(\alpha)$. According to the standard for a compact tension specimen,

$$f(\alpha) = f(a/W) = \frac{2 + \alpha}{(1 - \alpha)^{3/2}}(0.886 + 4.64\alpha - 13.32\alpha^2 + 14.72\alpha^3 - 5.6\alpha^4) \tag{6.11}$$

Equations 6.10 and 6.11 were applied to a value of $\alpha = 0.5$ and to two other values that were slightly above and below the value of 0.5. g' was calculated by finding the slope between these three alpha values computed around $\alpha = 0.5$.

α	g	g'
0.45	3.814311	
0.50	5.116801	32.68595
0.55	7.082906	

These values were used to determine the fracture energy (G_f) for each compact tension specimen that was evaluated from each paper that was reviewed.

6.2 Analytical Results

In the below figures and tables, the results for the fracture energy and the corrected fracture energy were calculated for the following papers and those results were plotted [11,12,15,23–25,58–71]. The largest percent difference for each data set is noted on each plot, as well as the particular nanofiller used in each experiment. The specimen size used in each experiment is different as are the fracture process zone (FPZ) sizes, since different nanofillers were used in each experiment. The diameter of the FPZ, c_f, can be calculated using Equation 6.2 and was calculated for each data point in the papers that were investigated.

The following list is a summary of each of the papers used for this analysis, with the type of testing done, specimen sizes, mechanical properties (given, assumed and calculated) that were used to determine the fracture energy values. The sizes of the specimens are given in length by width by thickness.

- In Dittanet, *et al.* 2012 [58], they used single edge notch bending to determine the fracture energy and other mechanical properties as a comparison between three different sizes of silica nanoparticles. The specimen size used was 75.6 mm by 12.7 mm by 6.36 mm.

  23nm Silica nanoparticle:

$\%wt$	E (MPa)	f_t (MPa)	K_f $(MPa.mm^{0.5})$	$G_{f(LEFM)}$ (N/mm)	$G_{f(Corrected)}$ (N/mm)	$\%diff$	c_f (mm)
0	3500	85	1.110	0.303	0.313	3.328	0.0667
2.5	3500	83	1.700	0.700	0.759	8.463	0.1697
5	3620	85	1.780	0.742	0.808	8.881	0.1781
10	4240	86	1.870	0.700	0.768	9.655	0.1936
15	4560	83	2.170	0.876	1.004	14.576	0.2923
20	4780	86	2.210	0.866	0.987	13.999	0.2807
25	5220	83	2.400	0.934	1.106	18.382	0.3686
30	5530	82	2.520	0.973	1.180	21.296	0.4271

  74nm Silica nanoparticle:

$\%wt$	E (MPa)	f_t (MPa)	K_f $(MPa.mm^{0.5})$	$G_{f(LEFM)}$ (N/mm)	$G_{f(Corrected)}$ (N/mm)	$\%diff$	c_f (mm)
0	3500	85	1.110	0.303	0.313	3.328	0.0667
2.5	3670	81	1.750	0.707	0.774	9.501	0.1905
5	3800	83	1.890	0.797	0.882	10.675	0.2141
10	4150	83	2.030	0.842	0.947	12.522	0.2511
15	4500	83	2.360	1.050	1.236	17.714	0.3552
20	4760	81	2.550	1.157	1.418	22.574	0.4527
25	5430	79	2.710	1.146	1.467	28.002	0.5616
30	5600	78	2.890	1.264	1.697	34.276	0.6874

170nm Silica nanoparticle:

$\%wt$	E (MPa)	f_t (MPa)	K_f $(MPa.mm^{0.5})$	$G_{f(LEFM)}$ (N/mm)	$G_{f(Corrected)}$ (N/mm)	$\%diff$	c_f (mm)
0	3500	85	1.11	0.303	0.313	3.328	0.0667
2.5	3500	83	1.68	0.684	0.740	8.254	0.1655
5	3620	85	1.75	0.717	0.778	8.556	0.1716
10	4250	84	2.04	0.830	0.932	12.320	0.2471
15	4600	85	2.31	0.983	1.139	15.917	0.3192
20	4870	85	2.48	1.070	1.271	18.799	0.3770
25	5350	83	2.52	1.006	1.214	20.687	0.4149
30	5780	82	2.65	1.030	1.278	24.109	0.4835

- In Jiang, *et al.* 2013 [24], they used single edge notched bending to find the fracture energy and other mechanical properties. The elastic modulus, ultimate strength and poison ratio had to be assumed, since they were not given in the original paper. The specimen was 150 mm by 20 mm by 10 mm.

  Graphene oxide (GO) nanoparticle:

$\%wt$	E (MPa)	f_t (MPa)	K_f $(MPa.mm^{0.5})$	v	$G_{f(LEFM)}$ (N/mm)	$G_{f(Corrected)}$ (N/mm)	$\%diff$	c_f (mm)
0	3000	50	44.349	0.35	0.575	0.637	10.642	0.3361
0.100	3000	50	60.096	0.35	1.056	1.283	21.449	0.6774
0.247	3000	50	53.026	0.35	0.822	0.954	15.942	0.5035
0.499	3000	50	37.279	0.35	0.406	0.436	7.291	0.2303
1.002	3000	50	31.494	0.35	0.290	0.305	5.098	0.1610

  Functionalized silica nanoparticles attached graphene oxide (ATGO):

$\%wt$	E (MPa)	f_t (MPa)	K_f $(MPa.mm^{0.5})$	v	$G_{f(LEFM)}$ (N/mm)	$G_{f(Corrected)}$ (N/mm)	$\%diff$	c_f (mm)
0	3000	50	44.349	0.35	0.575	0.637	10.642	0.3361
0.100	3000	50	51.419	0.35	0.773	0.888	14.849	0.4690
0.252	3000	50	58.168	0.35	0.990	1.186	19.826	0.6262
0.499	3000	50	68.452	0.35	1.371	1.778	29.724	0.9387
1.002	3000	50	83.556	0.35	2.042	3.101	51.840	1.6372
3.002	3000	50	82.913	0.35	2.011	3.029	50.643	1.5994

  SiO_2 mixed with the APTES (ATL):

$\%wt$	E (MPa)	f_t (MPa)	K_f $(MPa.mm^{0.5})$	v	$G_{f(LEFM)}$ (N/mm)	$G_{f(Corrected)}$ (N/mm)	$\%diff$	c_f (mm)
0	3000	50	44.349	0.35	0.575	0.637	10.642	0.3361
0.100	3000	50	48.527	0.35	0.689	0.778	13.014	0.4110
0.252	3000	50	56.561	0.35	0.936	1.109	18.546	0.5857
0.499	3000	50	65.559	0.35	1.257	1.592	26.611	0.8404
0.997	3000	50	73.915	0.35	1.598	2.181	36.457	1.1514
2.996	3000	50	71.344	0.35	1.489	1.982	33.140	1.0466

- Using compact tension testing, Liu *et al.* 2011 [59] tested the fracture toughness of silica and rubber particles, both individually and in different combinations to determine what type of effect it would have on the final material. The paper provided all the necessary information and none had to be approximated. The specimen size they used was 30 mm by 36 mm by 6 mm.

  Silica nanoparticles:

$\%wt$	E (MPa)	f_t (MPa)	K_f $(MPa.mm^{0.5})$	$G_{f(LEFM)}$ (N/mm)	$G_{f(Corrected)}$ (N/mm)	$\%diff$	c_f (mm)
0	2860	42.10	0.951	0.277	0.289	4.371	0.2053
2	2880	45.10	1.010	0.308	0.321	4.260	0.2001
4	2930	42.00	1.140	0.390	0.415	6.461	0.3034
6	2980	43.10	1.260	0.465	0.500	7.514	0.3529
8	3120	42.70	1.390	0.546	0.598	9.593	0.4505
10	3140	46.50	1.570	0.690	0.761	10.360	0.4866
12	3200	48.30	1.700	0.791	0.881	11.316	0.5314
20	3480	54.20	2.110	1.120	1.279	14.195	0.6667

  Rubber nanoparticles:

$\%wt$	E (MPa)	f_t (MPa)	K_f $(MPa.mm^{0.5})$	$G_{f(LEFM)}$ (N/mm)	$G_{f(Corrected)}$ (N/mm)	$\%diff$	c_f (mm)
0	2860	42.10	30.073	0.277	0.289	4.371	0.2053
2	2630	45.60	31.939	0.341	0.355	4.211	0.1978
4	2510	43.20	41.426	0.604	0.654	8.238	0.3869
6	2450	39.50	51.229	0.946	1.099	16.167	0.7593
8	2330	38.30	59.767	1.340	1.674	24.909	1.1698
10	2300	37.60	71.151	1.930	2.734	41.678	1.9573
12	2250	36.40	78.108	2.380	3.830	60.943	2.8621
15	2180	32.20	87.595	3.100	7.962	156.846	7.3660

  Rubber 6% constant while Silica varies:

$\%wt$	E (MPa)	f_t (MPa)	K_f $(MPa.mm^{0.5})$	$G_{f(LEFM)}$ (N/mm)	$G_{f(Corrected)}$ (N/mm)	$\%diff$	c_f (mm)
0	2860	42.10	0.951	0.277	0.289	4.371	0.2053
2	2520	39.80	1.720	1.030	1.217	18.136	0.8517
4	2550	39.80	1.790	1.100	1.319	19.890	0.9341
6	2670	40.00	1.950	1.250	1.554	24.290	1.1408
8	2800	41.10	2.030	1.290	1.613	25.052	1.1765
10	2900	35.60	2.800	2.480	5.295	113.525	5.3315

  Silicone 10% constant while Rubber varies:

$\%wt$	E (MPa)	f_t (MPa)	K_f $(MPa.mm^{0.5})$	$G_{f(LEFM)}$ (N/mm)	$G_{f(Corrected)}$ (N/mm)	$\%diff$	c_f (mm)
0	2860	42.10	0.951	0.277	0.289	4.371	0.2053
4	2920	43.90	1.930	1.120	1.332	18.904	0.8878
10	2780	35.60	2.800	2.480	5.058	103.945	4.8816

- In Zamanian *et al.* 2013 [60] they used single notch bending tests to determine the fracture energy and other mechanical properties of silica/epoxy composites, with three different sizes of silica nanoparticles (12 mm, 20 mm and 40 mm). An ultimate stress if 50 MPa was assumed for their data, since none was provided. Their specimen size used was 52.8 mm by 12 mm by 6 mm.

  12 mm Silica nanoparticle:

$\%wt$	E (MPa)	f_t (MPa)	K_f $(MPa.mm^{0.5})$	$G_{f(LEFM)}$ (N/mm)	$G_{f(Corrected)}$ (N/mm)	$\%diff$	c_f (mm)
0	3530	50	1.070	0.283	0.312	10.236	0.1940
1	3610	50	1.250	0.384	0.441	14.796	0.2804
3	3730	50	1.520	0.544	0.670	23.202	0.4397
4.5	3850	50	1.630	0.611	0.782	27.980	0.5302
6	3770	50	1.620	0.620	0.792	27.742	0.5257

  20 mm Silica nanoparticle:

$\%wt$	E (MPa)	f_t (MPa)	K_f $(MPa.mm^{0.5})$	$G_{f(LEFM)}$ (N/mm)	$G_{f(Corrected)}$ (N/mm)	$\%diff$	c_f (mm)
0	3530	50	1.070	0.283	0.312	10.236	0.1940
1	3570	50	1.180	0.347	0.391	12.981	0.2460
3	3690	50	1.320	0.417	0.486	16.661	0.3157
7	3960	50	1.500	0.497	0.608	22.380	0.4241
9	3890	50	1.470	0.486	0.589	21.273	0.4031

  40 mm Silica nanoparticle:

$\%wt$	E (MPa)	f_t (MPa)	K_f $(MPa.mm^{0.5})$	$G_{f(LEFM)}$ (N/mm)	$G_{f(Corrected)}$ (N/mm)	$\%diff$	c_f (mm)
0	3530	50	1.070	0.283	0.312	10.236	0.1940
1.5	3610	50	1.170	0.335	0.377	12.633	0.2394
4.5	3740	50	1.280	0.383	0.441	15.328	0.2904
7.5	3940	50	1.410	0.446	0.533	19.494	0.3694
10.5	3930	50	1.390	0.427	0.506	18.485	0.3503

- In Konnola *et al.* 2015 [61], they used single notch edge bending tests to find the fracture toughness and other mechanical properties for multiwalled nanotubes with different functional groups attached. The elastic modulus was assumed to be 3000MPa, since that information was not provided. The specimen size used was 24 mm by 6 mm by 3 mm.

  MWNT:

$\%wt$	E (MPa)	f_t (MPa)	K_f $(MPa.mm^{0.5})$	$G_{f(LEFM)}$ (N/mm)	$G_{f(Corrected)}$ (N/mm)	$\%diff$	c_f (mm)
0	3000	68.3	22.136	0.143	0.150	4.472	0.0424
0.1	3000	69.4	34.785	0.354	0.394	11.406	0.1081
0.2	3000	76.1	44.272	0.573	0.665	15.999	0.1516
0.3	3000	71.6	37.947	0.421	0.476	12.926	0.1225
0.4	3000	68.4	34.785	0.354	0.396	11.781	0.1116

MWNT-COOH:

$\%wt$	E (MPa)	f_t (MPa)	K_f $(MPa.mm^{0.5})$	$G_{f(LEFM)}$ (N/mm)	$G_{f(Corrected)}$ (N/mm)	$\%diff$	c_f (mm)
0	3000	68.30	22.136	0.143	0.150	4.472	0.0424
0.1	3000	71.70	28.460	0.237	0.253	6.861	0.0650
0.2	3000	72.30	41.110	0.494	0.569	15.174	0.1438
0.3	3000	78.90	37.947	0.421	0.465	10.408	0.0986
0.4	3000	68.60	25.298	0.187	0.198	5.867	0.0556

MWNT-g-PES:

$\%wt$	E (MPa)	f_t (MPa)	K_f $(MPa.mm^{0.5})$	$G_{f(LEFM)}$ (N/mm)	$G_{f(Corrected)}$ (N/mm)	$\%diff$	c_f (mm)
0	3000	68.300	22.136	0.143	0.150	4.472	0.0424
0.1	3000	80.800	41.110	0.494	0.553	11.793	0.1117
0.2	3000	86.200	47.434	0.658	0.751	14.077	0.1334
0.3	3000	83.500	53.759	0.845	1.017	20.325	0.1926
0.4	3000	76.200	37.947	0.421	0.469	11.243	0.1065

- In Naous *et al.* 2006 [62], they used single edge notch bending to determine the fracture toughness and other mechanical properties of a $Al_2O_3/epoxy$ composite material. All the information that was needed for analysis was provided and no assumptions were made. The specimens were 53 mm by 12 mm by 6 mm.

$\%wt$	E (MPa)	f_t (MPa)	K_f $(MPa.mm^{0.5})$	$G_{f(LEFM)}$ (N/mm)	$G_{f(Corrected)}$ (N/mm)	$\%diff$	c_f (mm)
0	2495.05	48.793	44.275	0.689	0.828	20.159	0.3820
0.5	2542.57	50.091	47.737	0.786	0.965	22.708	0.4303
1	2566.34	50.365	46.232	0.731	0.882	20.728	0.3928
2	2661.39	50.775	49.083	0.794	0.981	23.518	0.4457

- Wetzel *et al.* 2006 [63] used compact tension testing to test the fracture toughness and other mechanical properties for $Al_2O_3/epoxy$ and $TiO_2/epoxy$ specimens (sized 30 mm by 36 mm by 4 mm). The elastic modulus of the specimens with nanofiller in them was assumed to be 3000 MPa since that value was not provided in the original study.

  Al_2O_3:

$\%wt$	E (MPa)	f_t (MPa)	K_f $(MPa.mm^{0.5})$	$G_{f(LEFM)}$ (N/mm)	$G_{f(Corrected)}$ (N/mm)	$\%diff$	c_f (mm)
0	2600	125.274	15.784	0.084	0.084	0.131	0.0061
0.5	3000	128.259	18.647	0.102	0.102	0.174	0.0082
1	3000	130.249	20.555	0.124	0.124	0.205	0.0096
2	3000	134.229	22.599	0.149	0.150	0.234	0.0110
3	3000	136.716	24.099	0.170	0.170	0.256	0.0120
5	3000	139.701	25.734	0.194	0.194	0.280	0.0131
10	3000	145.174	36.094	0.381	0.383	0.511	0.0240

TiO_2:

$\%wt$	E (MPa)	f_t (MPa)	K_f $(MPa.mm^{0.5})$	$G_{f(LEFM)}$ (N/mm)	$G_{f(Corrected)}$ (N/mm)	$\%diff$	c_f (mm)
0	2600	125.274	16.057	0.087	0.087	0.135	0.0064
0.5	3000	129.254	18.510	0.100	0.100	0.169	0.0079
1	3000	129.254	18.510	0.100	0.100	0.169	0.0079
2	3000	130.249	19.737	0.114	0.114	0.189	0.0089
3	3000	134.726	20.964	0.129	0.129	0.199	0.0094
4	3000	132.239	22.872	0.153	0.153	0.247	0.0116
5	3000	139.701	22.872	0.153	0.153	0.221	0.0104
8	3000	143.184	23.690	0.164	0.165	0.226	0.0106
10	3000	143.682	27.234	0.217	0.218	0.296	0.0139

- Zhang *et al.* 2008 [64] used compact tension testing to find the fracture toughness and other mechanical properties. The test specimen was 36 mm by 36 mm by 5.7 mm and all the data that was needed for the fracture energy calculations was given in the original paper.

$\%wt$	E (MPa)	f_t (MPa)	K_f $(MPa.mm^{0.5})$	$G_{f(LEFM)}$ (N/mm)	$G_{f(Corrected)}$ (N/mm)	$\%diff$	c_f (mm)
0	3020	82.39	20.239	0.119	0.119	0.413	0.0233
1	3220	82.94	20.555	0.115	0.116	0.424	0.0239
3	3290	82.43	24.666	0.161	0.162	0.611	0.0344
6	3490	83.88	26.879	0.183	0.184	0.714	0.0402
7	3670	83.92	28.144	0.189	0.191	0.776	0.0437
8	3600	83.80	29.093	0.205	0.207	0.827	0.0466
10	3920	85.90	31.307	0.217	0.219	0.910	0.0513
13	4130	83.37	32.571	0.225	0.228	1.056	0.0595
15	4470	88.94	35.734	0.253	0.256	1.129	0.0636

- In Ma *et al.* 2008 [66] they used compact tension to test the fracture toughness and fracture energy of a silica/epoxy composite cured using two different agents (J230 and DDS). The specimen size used was 30 mm by 43.2 mm by 5 mm and all the information needed to calculate the corrected fracture energy was given, so no assumptions were made.

  Cured with J230:

$\%wt$	E (MPa)	f_t (MPa)	K_f $(MPa.mm^{0.5})$	$G_{f(LEFM)}$ (N/mm)	$G_{f(Corrected)}$ (N/mm)	$\%diff$	c_f (mm)
0	2750	57.1	23.085	0.175	0.177	1.402	0.0659
10	3640	58.3	38.896	0.368	0.382	3.834	0.1801
20	3850	59.5	53.126	0.655	0.702	7.151	0.3358

Cured with DDS:

$\%wt$	E (MPa)	f_t (MPa)	K_f $(MPa.mm^{0.5})$	$G_{f(LEFM)}$ (N/mm)	$G_{f(Corrected)}$ (N/mm)	$\%diff$	c_f (mm)
0	3200	88.2	16.128	0.073	0.073	0.282	0.0132
10	3790	104.3	21.820	0.109	0.109	0.357	0.0168
20	4480	107.4	25.931	0.132	0.133	0.483	0.0227

- Chen *et al.* 2008 [67] used 19 mm by 19 mm by 3 mm compact tension specimens to test the fracture toughness and fracture energy and other mechanical properties in silica/epoxy composites. All the information necessary for the corrected calculations was given, so no assumptions needed to be made.

$\%wt$	E (MPa)	f_t (MPa)	K_f $(MPa.mm^{0.5})$	$G_{f(LEFM)}$ (N/mm)	$G_{f(Corrected)}$ (N/mm)	$\%diff$	c_f (mm)
0	2760	86	1.381	0.606	0.627	3.461	0.1029
1.25	2970	82	1.838	0.998	1.068	6.976	0.2075
5	3170	86	1.916	1.016	1.086	6.886	0.2048
10	3450	86	1.587	0.640	0.670	4.620	0.1374

- Kim *et al.* 2008 [12] used single edge notch bending tests to find the fracture toughness and other mechanical properties for carbon black/epoxy and nanoclay/epoxy composites. The specimen size they used was 48 mm by 12 mm by 6 mm. For the carbon black specimens, a poisson ratio of 0.35 was assumed so that the fracture energy using LEFM could be calculated. For the nanoclay specimens the elastic modulus, ultimate strength and the poisson ratio were assumed to be 3000MPa, 50MPa, and 0.35 respectively.

  Carbon Black:

$\%wt$	E (MPa)	f_t (MPa)	K_f $(MPa.mm^{0.5})$	v	$G_{f(LEFM)}$ (N/mm)	$G_{f(Corrected)}$ (N/mm)	$\%diff$	c_f (mm)
0	2213	44.688	23.446	0.35	0.218	0.231	5.942	0.1126
0.5	2213	50.000	24.801	0.35	0.244	0.257	5.278	0.1000
1.0	2213	53.750	25.931	0.35	0.267	0.280	4.978	0.0943
1.5	2213	54.375	26.473	0.35	0.278	0.292	5.075	0.0962
2.0	2213	52.500	27.647	0.35	0.303	0.321	5.989	0.1135
3.0	2213	50.000	28.867	0.35	0.330	0.355	7.287	0.1381

  Nanoclay:

$\%wt$	E (MPa)	f_t (MPa)	K_f $(MPa.mm^{0.5})$	v	$G_{f(LEFM)}$ (N/mm)	$G_{f(Corrected)}$ (N/mm)	$\%diff$	c_f (mm)
0	3000	50	23.511	0.35	0.162	0.169	4.718	0.0894
0.5	3000	50	28.117	0.35	0.231	0.247	6.887	0.1305
1	3000	50	31.554	0.35	0.291	0.317	8.832	0.1673
1.5	3000	50	34.235	0.35	0.343	0.379	10.561	0.2001
2	3000	50	34.166	0.35	0.341	0.377	10.514	0.1992
3	3000	50	35.129	0.35	0.361	0.401	11.182	0.2119

- In Carolan *et al.* 2008 [68], they did single edge notch bending tests on composites containing silica nanoparticles and/or polysiloxane core-shell rubber (CSR) nanoparticles. The specimen size was 48 mm by 12 mm by 6 mm. The ultimate strength was assumed to be 50MPa and

the fracture toughness was not given nor was it needed since the fracture energy using LEFM was calculated in the original paper.

Silica nanoparticle:

$\%wt$	E (MPa)	f_t (MPa)	$G_{f(LEFM)}$ (N/mm)	$G_{f(Corrected)}$ (N/mm)	$\%diff$	c_f (mm)
0	3114.29	50	0.125	0.130	3.764	0.0713
5	3257.14	50	0.193	0.205	6.198	0.1175
10	3528.57	50	0.229	0.247	8.099	0.1535
20	4028.57	50	0.266	0.296	11.064	0.2097

Silica & reactive diluent(25%) nanoparticle:

$\%wt$	E (MPa)	f_t (MPa)	$G_{f(LEFM)}$ (N/mm)	$G_{f(Corrected)}$ (N/mm)	$\%diff$	c_f (mm)
0	2928.57	50	0.174	0.182	4.957	0.0939
4	3071.43	50	0.189	0.200	5.701	0.1080
8	3200	50	0.202	0.214	6.374	0.1208
16	3571.43	50	0.245	0.267	8.847	0.1676

Core shell rubber nanoparticle:

$\%wt$	E (MPa)	f_t (MPa)	$G_{f(LEFM)}$ (N/mm)	$G_{f(Corrected)}$ (N/mm)	$\%diff$	c_f (mm)
0	3126.17	50	0.124	0.129	3.733	0.0707
5	2719.63	50	0.285	0.307	7.746	0.1468
10	2481.31	50	0.514	0.583	13.441	0.2547
20	2116.82	50	0.890	1.079	21.224	0.4022

Core shell rubber & 25%(reactive diluent) nanoparticle:

$\%wt$	E (MPa)	f_t (MPa)	$G_{f(LEFM)}$ (N/mm)	$G_{f(Corrected)}$ (N/mm)	$\%diff$	c_f (mm)
0	2943.93	50	0.179	0.188	5.147	0.0975
4	2733.64	50	0.514	0.591	15.013	0.2845
8	2439.25	50	0.932	1.181	26.760	0.5071
16	1920.56	50	1.239	1.591	28.382	0.5378

Core shell rubber & 25%(reactive diluent)+4%(silica) nanoparticle:

$\%wt$	E (MPa)	f_t (MPa)	$G_{f(LEFM)}$ (N/mm)	$G_{f(Corrected)}$ (N/mm)	$\%diff$	c_f (mm)
2	2850	50	0.349	0.385	10.181	0.1929
4	2720	50	0.631	0.751	18.975	0.3596
6	2670	50	0.780	0.967	23.976	0.4543
8	2610	50	1.055	1.417	34.348	0.6509

Core shell rubber & 25%(reactive diluent)+8%(silica) nanoparticle:

$\%wt$	E (MPa)	f_t (MPa)	$G_{f(LEFM)}$ (N/mm)	$G_{f(Corrected)}$ (N/mm)	$\%diff$	c_f (mm)
2	2970	50	0.371	0.414	11.413	0.2163
4	2980	50	0.724	0.906	25.067	0.4750
6	2710	50	1.077	1.477	37.187	0.7047
8	2640	50	1.218	1.737	42.586	0.8070

- In Bortz *et al.* 2011 [69] they used helical ribbon CNF as the filler for a structural epoxy and tested to see if the fracture toughness and fatigue performance would change. The specimen size tested was 50.8 mm by 12.7 mm by 4 mm. The ultimate stress for 0.5%wt was not given and was assumed to be 78MPa and the elastic modulus for all was assumed to be 3000MPa.

$\%wt$	E (MPa)	f_t (MPa)	$G_{f(LEFM)}$ (N/mm)	$G_{f(Corrected)}$ (N/mm)	$\%diff$	c_f (mm)
0	3000	79.7	0.243	0.249	2.583	0.0518
0.5	3000	78	0.556	0.592	6.400	0.1284
1	3000	77.8	0.615	0.659	7.167	0.1437

- Swaminathan, *et al.* 2010 [70] looked at the fracture properties of exfoliated nanoclay composites, through single edge notch (specimen size 40 mm by 10 mm by 5 mm). The elastic modulus was assumed to be 3000MPa, poisson of 0.35, and the ultimate strength is assumed to be 50MPa since these values were not provided in the original paper and are needed to calculated both values of G_f.

$\%wt$	E (MPa)	f_t (MPa)	K_f $(MPa.mm^{0.5})$	v	$G_{f(LEFM)}$ (N/mm)	$G_{f(Corrected)}$ (N/mm)	$\%diff$	c_f (mm)
0	3000	50	25.931	0.35	0.197	0.211	7.039	0.1112
0.4	3000	50	27.196	0.35	0.216	0.233	7.798	0.1231
1.6	3000	50	27.828	0.35	0.227	0.245	8.195	0.1294
3.9	3000	50	29.725	0.35	0.258	0.283	9.459	0.1494
5.3	3000	50	30.042	0.35	0.264	0.290	9.681	0.1529

- Vaziri *et al.* 2011 [71] investigated the fracture and mechanical properties polystyrene/silica nanocomposites. They used single edge notch bending test with a specimen sized 51.12 mm by 12.78 mm by 3.175 mm. The poisson ratio was assumed to be 0.35 in order to calculate the fracture energy (G_f) using LEFM.

$\%wt$	E (MPa)	f_t (MPa)	K_f $(MPa.mm^{0.5})$	v	$G_{f(LEFM)}$ (N/mm)	$G_{f(Corrected)}$ (N/mm)	$\%diff$	c_f (mm)
0	3120	34.65	21.788	0.35	0.134	0.144	8.184	0.1652
0.1	3135.7	36.55	22.770	0.35	0.145	0.157	8.021	0.1619
0.2	3150.3	37.2	25.610	0.35	0.183	0.201	9.972	0.2012
0.8	3183.0	37.4	26.880	0.35	0.199	0.221	10.967	0.2213
2.0	3454.0	34.4	21.380	0.35	0.116	0.125	7.980	0.1610
5.0	3490.0	29.5	19.100	0.35	0.092	0.100	8.720	0.1760
10.0	3604.0	28.0	17.710	0.35	0.076	0.083	8.288	0.1673

- Tang *et al.* 2013 [23] used compact tension testing (specimens 36 mm by 36 mm by 7 mm) to investigate the effect of graphene dispersion on the mechanical properties of graphene/epoxy composites. All the necessary information for calculating the fracture energies was provided in the original paper and no assumptions about the data needed to be made.

  Poorly dispersed graphene samples:

$\%wt$	E (MPa)	f_t (MPa)	K_f $(MPamm^{0.5})$	v	$G_{f(LEFM)}$ (N/mm)	$G_{f(Corrected)}$ (N/mm)	$\%diff$	c_f (mm)
0	2928.0	53.083	15.669	0.35	0.074	0.074	0.601	0.0338
0.025	2947.2	51.660	17.435	0.35	0.091	0.091	0.787	0.0443
0.05	2976.0	46.601	18.347	0.35	0.099	0.100	1.073	0.0605
0.1	3038.4	43.123	19.088	0.35	0.105	0.107	1.361	0.0767
0.2	3074.4	39.012	19.316	0.35	0.106	0.108	1.708	0.0963

Highly dispersed graphene samples:

$\%wt$	E (MPa)	f_t (MPa)	K_f $(MPamm^{0.5})$	v	$G_{f(LEFM)}$ (N/mm)	$G_{f(Corrected)}$ (N/mm)	$\%diff$	c_f (mm)
0	2928.0	53.083	15.669	0.35	0.074	0.074	0.601	0.0338
0.025	2961.6	56.878	18.689	0.35	0.103	0.104	0.745	0.0420
0.05	3002.4	53.874	19.486	0.35	0.111	0.112	0.904	0.0510
0.1	3050.4	51.344	20.455	0.35	0.120	0.122	1.099	0.0620
0.2	3105.6	52.609	23.703	0.35	0.159	0.161	1.410	0.0795

- Shokreih et al 2013 [25] looked at the effect of graphene nanoplatelets and nanosheets on fracture toughness in epoxy composites using single edge notch bending test. The test specimen used was 72 mm by 18 mm by 9 mm. The fracture energy using LEFM was provided in the original paper, so it did not need to be calculated again.

$\%wt$	E (MPa)	f_t (MPa)	$G_{f(LEFM)}$ (N/mm)	$G_{f(Corrected)}$ (N/mm)	$\%diff$	c_f (mm)
0	2500	59.923	0.350	0.364	3.922	0.1115
0.05	2580.68	67.066	0.390	0.404	3.592	0.1021
0.1	2607.95	69.672	0.408	0.422	3.510	0.0998
0.25	2718.75	73.822	0.456	0.473	3.654	0.1039
0.5	2759.66	70.058	0.582	0.613	5.340	0.1518
1	2769.89	67.259	0.380	0.394	3.734	0.1061

- Khan *et al.* 2013 [15] used compact tension testing to investigate the effects of multi-wall carbon nanotube alignment on mechanical properties of epoxy nanocomposites. A specimen sized 45 mm by 43.2 mm by 5 mm was used. To calculate the fracture energy, the ultimate stress was assumed to be 50MPa and the poisson ratio to be 0.35, since these values were not provided in the original paper.

$\%wt$	E (MPa)	f_t (MPa)	K_f $(MPa.mm^{0.5})$	v	$G_{f(LEFM)}$ (N/mm)	$G_{f(Corrected)}$ (N/mm)	$\%diff$	c_f (mm)
0	2910.45	50	32.744	0.35	0.323	0.331	2.407	0.1696
0.1	3031.34	50	36.563	0.35	0.387	0.399	3.019	0.2127
0.3	3340.30	50	38.472	0.35	0.389	0.402	3.354	0.2363
0.5	3434.33	50	37.422	0.35	0.358	0.369	3.167	0.2231

- Chandrasekaran et al 2008 [11] used a 32 mm by 8 mm by 4 mm specimen size to test the fracture toughness and failure mechanism of graphene based epoxy composites. The elastic modulus, ultimate strength and poisson ratio were assumed to be 3000MPa, 50MPa and 0.35, respectively, since these values were not provided in the original paper and are needed to calculate the fracture energy.

  Graphene oxide:

$\%wt$	E (MPa)	f_t (MPa)	K_f $(MPa.mm^{0.5})$	v	$G_{f(LEFM)}$ (N/mm)	$G_{f(Corrected)}$ (N/mm)	$\%diff$	c_f (mm)
0	3000	50	17.930	0.35	0.0940	0.0979	4.0911	0.0517
0.05	3000	50	19.835	0.35	0.1151	0.1209	5.0529	0.0638
0.1	3000	50	22.659	0.35	0.1502	0.1602	6.6975	0.0846
0.3	3000	50	24.186	0.35	0.1711	0.1843	7.7022	0.0973
0.5	3000	50	25.102	0.35	0.1843	0.1997	8.3463	0.1054

Graphene nanoparticles:

$\%wt$	E (MPa)	f_t (MPa)	K_f $(MPa.mm^{0.5})$	v	$G_{f(LEFM)}$ (N/mm)	$G_{f(Corrected)}$ (N/mm)	$\%diff$	c_f (mm)
0	3000	50	18.494	0.35	0.100	0.104	4.364	0.0551
0.2	3000	50	20.140	0.35	0.119	0.125	5.218	0.0659
0.5	3000	50	22.430	0.35	0.147	0.157	6.554	0.0828
1	3000	50	25.713	0.35	0.193	0.210	8.793	0.1111
2	3000	50	23.117	0.35	0.156	0.167	6.990	0.0883

Multi-walled carbon nanotubes:

$\%wt$	E (MPa)	f_t (MPa)	K_f $(MPa.mm^{0.5})$	v	$G_{f(LEFM)}$ (N/mm)	$G_{f(Corrected)}$ (N/mm)	$\%diff$	c_f (mm)
0	3000	50	18.012	0.35	0.095	0.099	4.130	0.0522
0.2	3000	50	18.843	0.35	0.104	0.109	4.538	0.0573
0.5	3000	50	19.453	0.35	0.111	0.116	4.851	0.0613

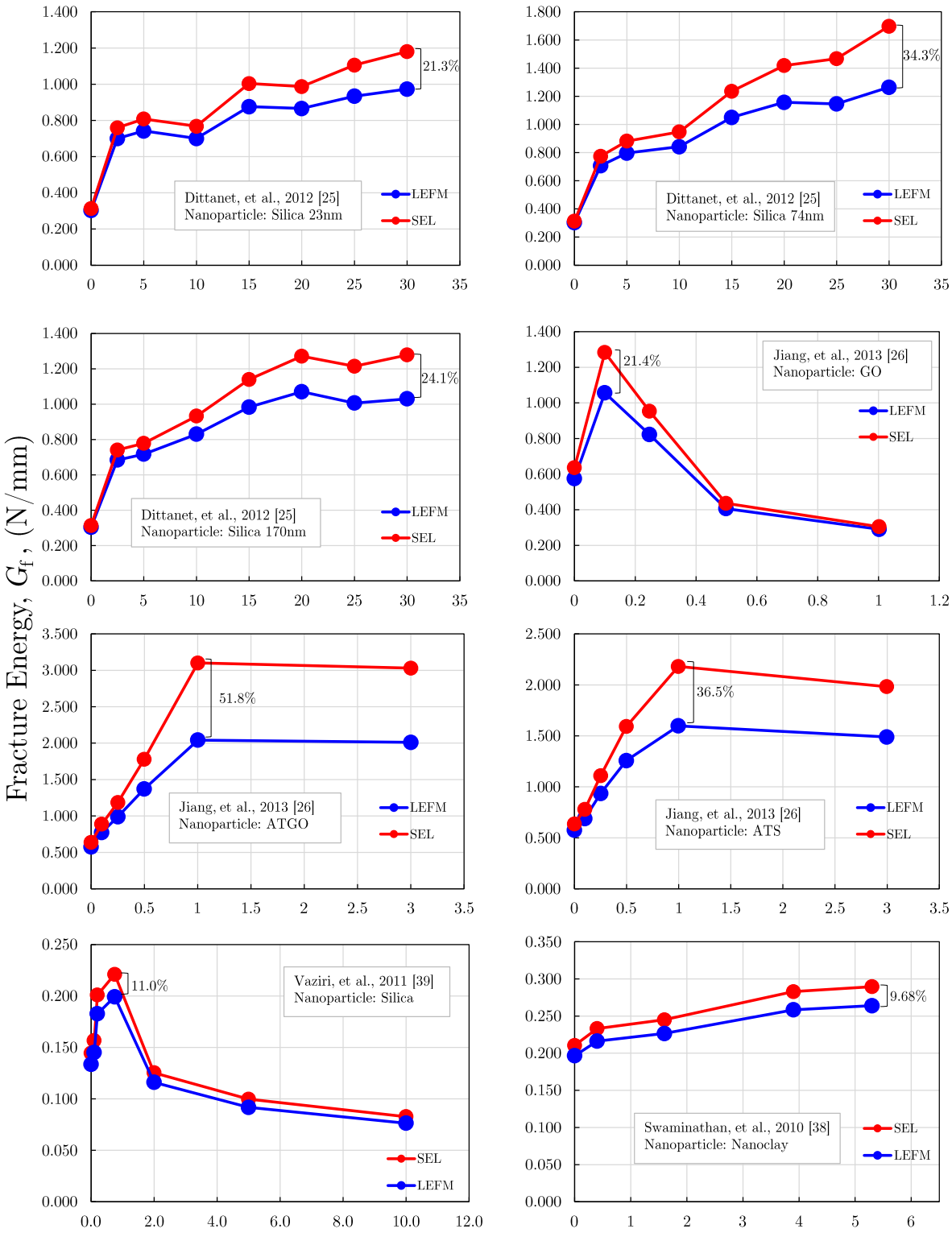
Fracture Energy, G_f, (N/mm)
Nanoparticle Weight Percent, %wt
Dittanet, et al., 2012 [25]
Nanoparticle: Silica 23nm
21.3%
LEFM
SEL
Dittanet, et al., 2012 [25]
Nanoparticle: Silica 74nm
34.3%
LEFM
SEL
Dittanet, et al., 2012 [25]
Nanoparticle: Silica 170nm
24.1%
LEFM
SEL
Jiang, et al., 2013 [26]
Nanoparticle: GO
21.4%
LEFM
SEL
Jiang, et al., 2013 [26]
Nanoparticle: ATGO
51.8%
LEFM
SEL
Jiang, et al., 2013 [26]
Nanoparticle: ATS
36.5%
LEFM
SEL
Vaziri, et al., 2011 [39]
Nanoparticle: Silica
11.0%
SEL
LEFM
Swaminathan, et al., 2010 [38]
Nanoparticle: Nanoclay
9.68%
SEL
LEFM

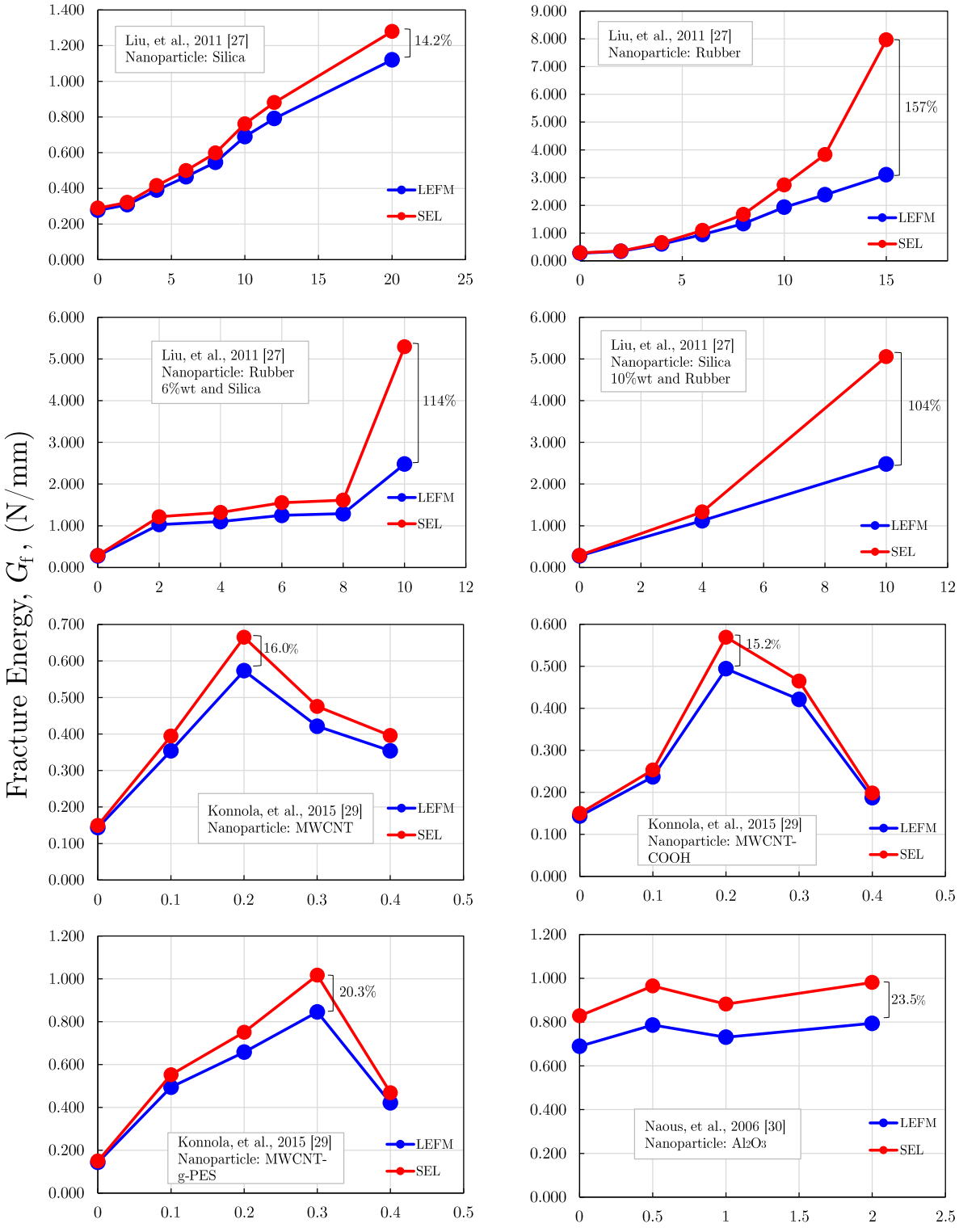
Liu, et al., 2011 [27]
Nanoparticle: Silica
14.2%
LEFM
SEL
Liu, et al., 2011 [27]
Nanoparticle: Rubber
157%
LEFM
SEL
Liu, et al., 2011 [27]
Nanoparticle: Rubber
6%wt and Silica
114%
LEFM
SEL
Liu, et al., 2011 [27]
Nanoparticle: Silica
10%wt and Rubber
104%
LEFM
SEL
Konnola, et al., 2015 [29]
Nanoparticle: MWCNT
16.0%
LEFM
SEL
Konnola, et al., 2015 [29]
Nanoparticle: MWCNT-
COOH
15.2%
LEFM
SEL
Konnola, et al., 2015 [29]
Nanoparticle: MWCNT-
g-PES
20.3%
LEFM
SEL
Naous, et al., 2006 [30]
Nanoparticle: Al2O3
23.5%
LEFM
SEL
Fracture Energy, G_f, (N/mm)
Nanoparticle Weight Percent, %wt

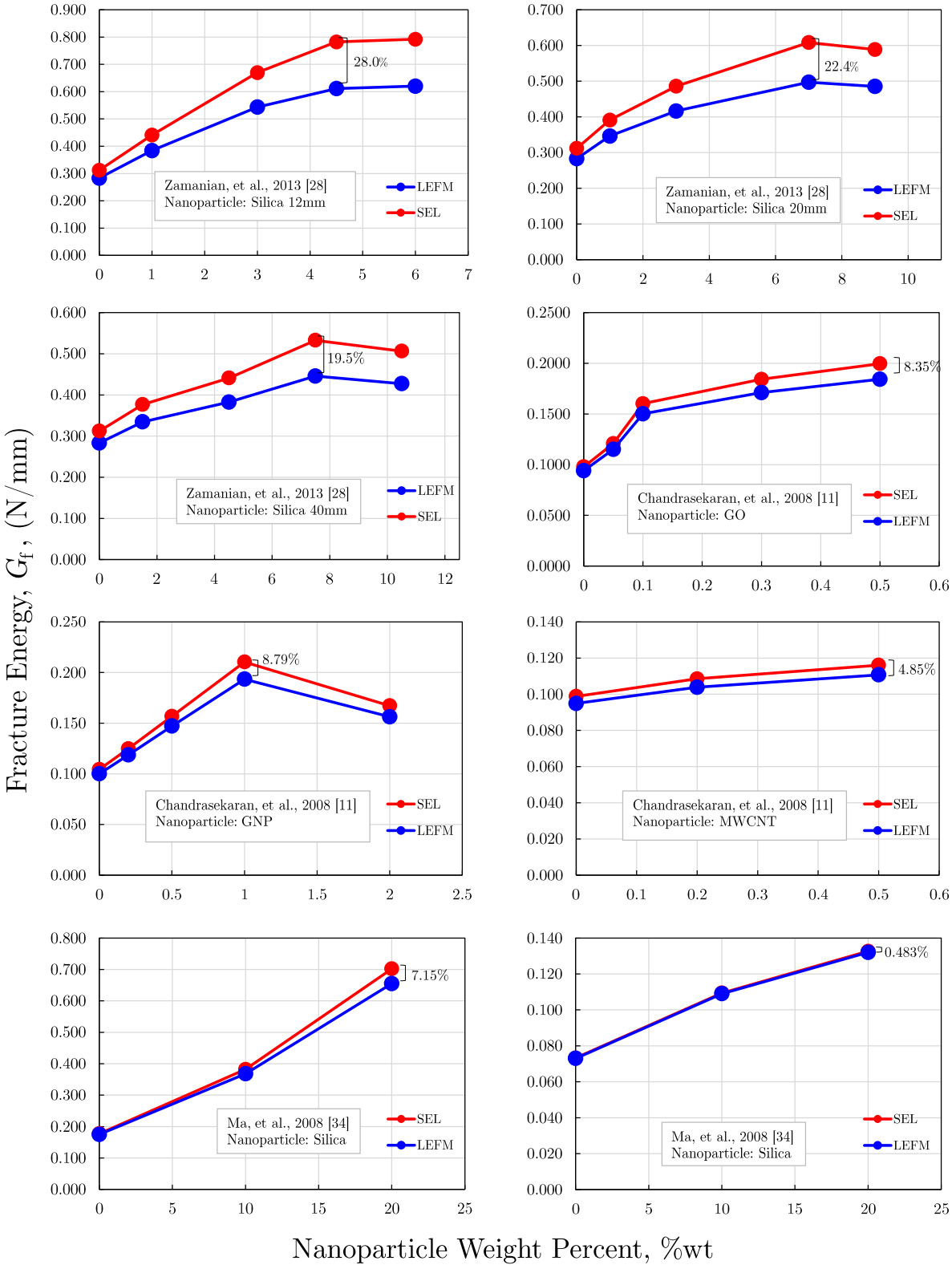
Fracture Energy, G_f, (N/mm)
Nanoparticle Weight Percent, %wt
Zamanian, et al., 2013 [28]
Nanoparticle: Silica 12mm
28.0%
LEFM
SEL
Zamanian, et al., 2013 [28]
Nanoparticle: Silica 20mm
22.4%
LEFM
SEL
Zamanian, et al., 2013 [28]
Nanoparticle: Silica 40mm
19.5%
LEFM
SEL
Chandrasekaran, et al., 2008 [11]
Nanoparticle: GO
8.35%
SEL
LEFM
Chandrasekaran, et al., 2008 [11]
Nanoparticle: GNP
8.79%
SEL
LEFM
Chandrasekaran, et al., 2008 [11]
Nanoparticle: MWCNT
4.85%
SEL
LEFM
Ma, et al., 2008 [34]
Nanoparticle: Silica
7.15%
SEL
LEFM
Ma, et al., 2008 [34]
Nanoparticle: Silica
0.483%
SEL
LEFM

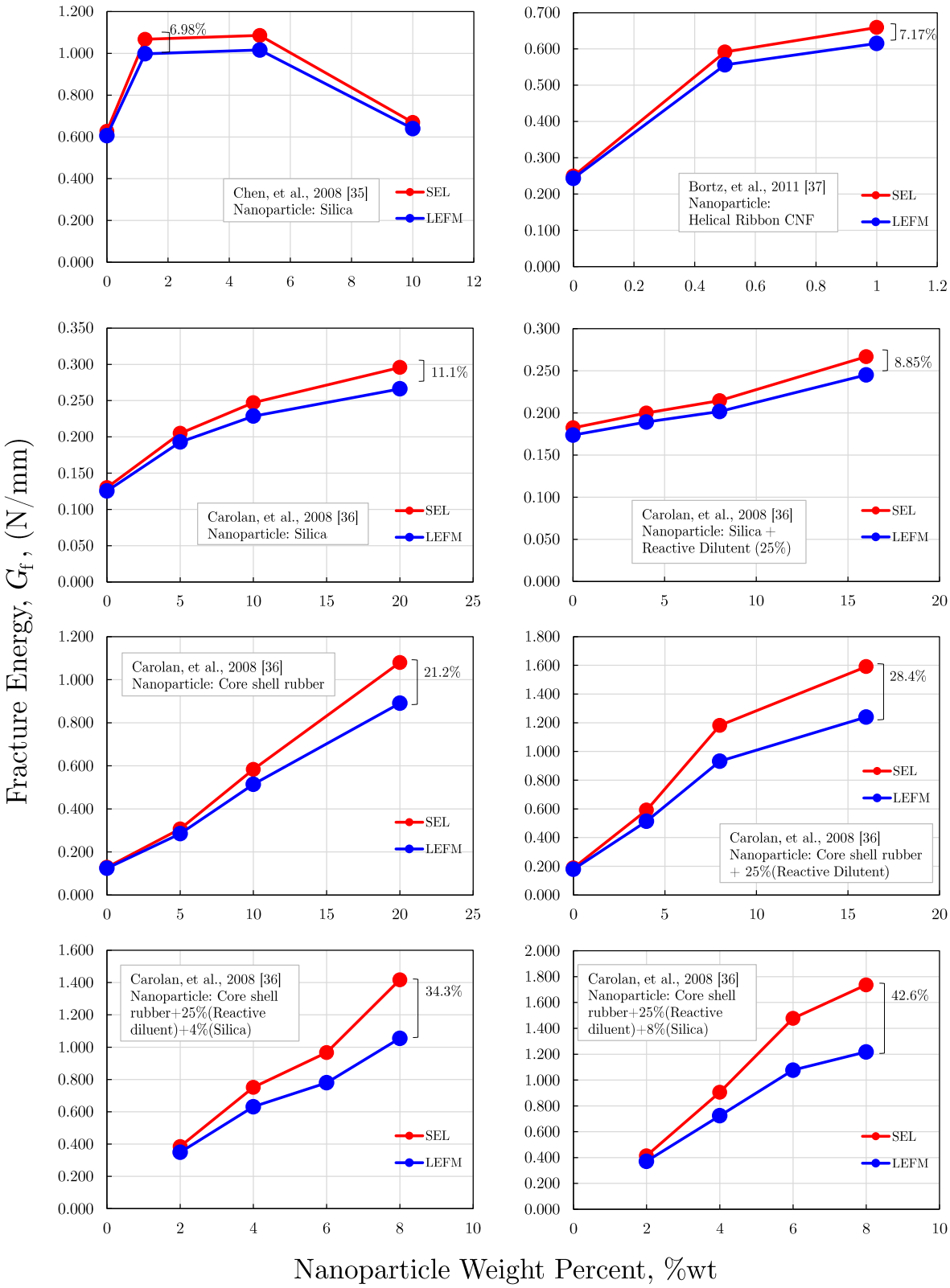
Fracture Energy, G_f, (N/mm)
Nanoparticle Weight Percent, %wt
Chen, et al., 2008 [35]
Nanoparticle: Silica
6.98%
SEL
LEFM
Bortz, et al., 2011 [37]
Nanoparticle:
Helical Ribbon CNF
7.17%
Carolan, et al., 2008 [36]
Nanoparticle: Silica
11.1%
Carolan, et al., 2008 [36]
Nanoparticle: Silica +
Reactive Dilutent (25%)
8.85%
Carolan, et al., 2008 [36]
Nanoparticle: Core shell rubber
21.2%
Carolan, et al., 2008 [36]
Nanoparticle: Core shell rubber
+ 25%(Reactive Dilutent)
28.4%
Carolan, et al., 2008 [36]
Nanoparticle: Core shell
rubber+25%(Reactive
diluent)+4%(Silica)
34.3%
Carolan, et al., 2008 [36]
Nanoparticle: Core shell
rubber+25%(Reactive
diluent)+8%(Silica)
42.6%

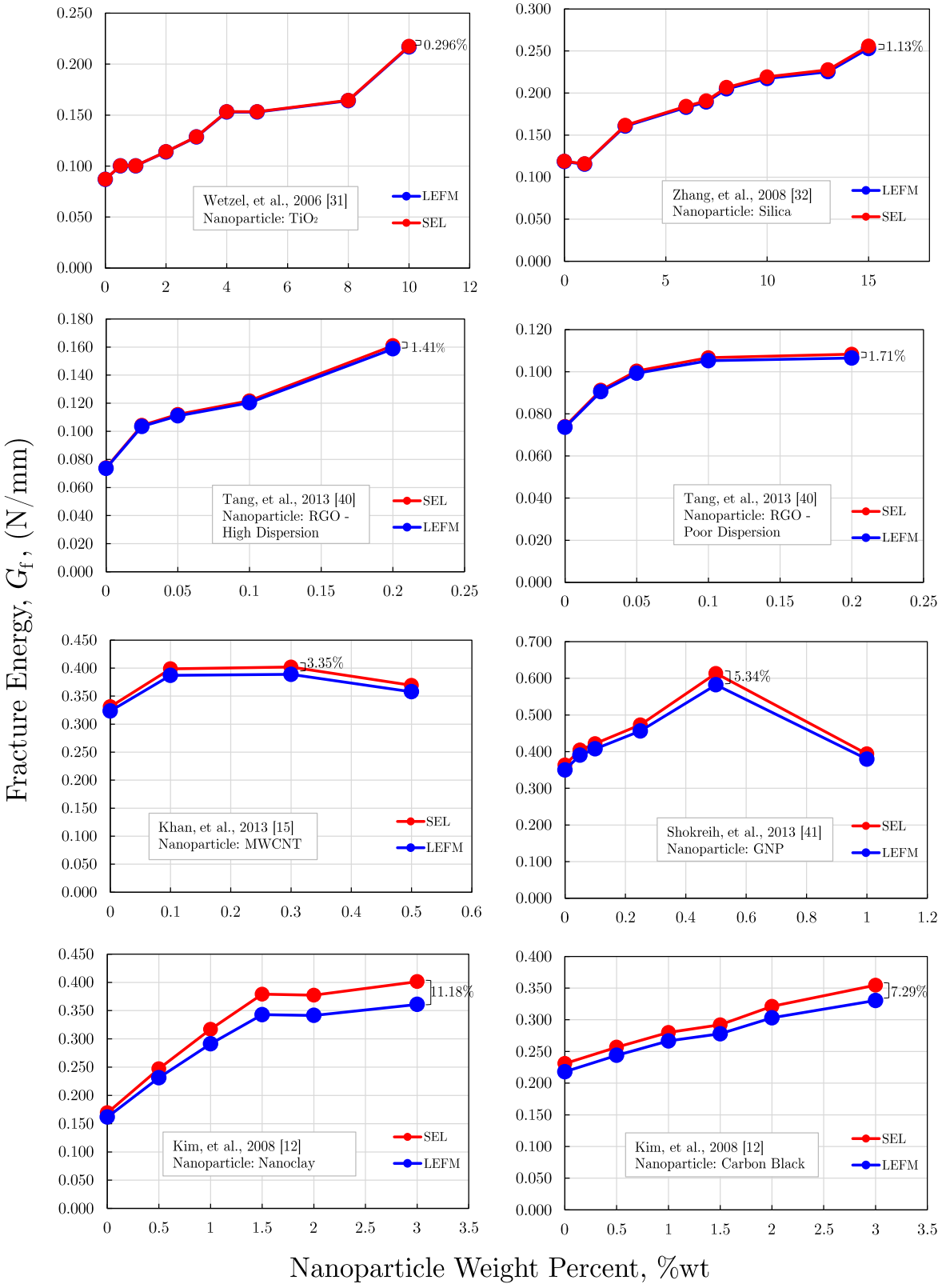

Figure 6.1: Comparative Analysis of $G_{f_{LEFM}}$ and $G_{f_{Corrected}}$ values to the nanoparticle $\%wt$ across multiple studies

6.3 Discussion

The overall results show a great deal of variation, with some cases showing very little difference between the LEFM and the corrected fracture energy values (Wetzel [63] showed 0.296% difference) and in other cases the corrected fracture energy method shows a much greater increase in the energy measured, up to 157% in Liu [59]. The size of the specimens used from one study to the next does not vary greatly enough to explain the huge difference in the percent difference values calculated. What does explain these results is that the specimens that have the greater fracture process zones also have a greater percent increase calculated. The size of the FPZ region is a material property that depends on the specific composition of the composite being analyzed. This means that the size of the FPZ changes as more nanofiller is added. If the FPZ takes up a large enough percentage of the area of the specimen, the area of the specimen cannot be neglected and needs to be factored into the overall calculation of the fracture energy. In LEFM, the assumption is that the area at the tip of a crack is negligible (very small) which means that the force at the crack tip is infinite. Taking the FPZ area into account, if that area is large enough, say in a smaller sample, it cannot be ignored and the LEFM analysis method falls apart.

In the case of the results for Liu *et al.* [59], the largest percent increase was observed as well as the greatest FPZ size. Liu was using compact tension specimens,

$$Area_{Specimen} = 30mm * 36mm = 1080mm^2$$

and the FPZ diameter was calculated to be $FPZ = 7.3660mm$ which means the area of the FPZ is

$$Area_{FPZ} = \pi \left(\frac{7.3660mm}{2} \right)^2 = 42.614mm^2$$

Comparing the area of the specimen to the area of the FPZ,

$$\left(\frac{42.614mm^2}{1080mm^2} \right) * 100 = 3.946\%$$

This might not seem like a large percentage, but this means that the size of the FPZ zone is large enough to allow for behavior that is inconsistent with the LEFM model because this area of weakened material is too large to be simplified as a singular point.

On the other hand, we also have data which shows very little difference between the LEFM and Corrected G_f calculations. Wetzel *et al.* [63] also used compact tension for their testing, with the same specimen size used as Liu *et al.* The area of their specimen is

$$Area_{Specimen} = 30mm * 36mm = 1080mm^2$$

and the FPZ diameter was measured to be $FPZ = 0.0139mm$ which means that the of the FPZ is

$$Area_{FPZ} = \pi \left(\frac{0.0139mm}{2} \right)^2 = 1.517 * 10^{-4} mm^2$$

Comparing the area of the specimen to the area of the FPZ,

$$\left(\frac{1.517 * 10^{-4} mm^2}{1080mm^2} \right) * 100 = 1.405 * 10^{-5}\%$$

Keep in mind that both experiments used the same size specimen sizes and the nanofillers used were in similar concentrations (Liu: 15%wt Rubber and Wetzel: 10%wt TiO_2). The difference is clearly from how the different nanofillers bond with the epoxy, or rather how well they can bond. This bond can be effected by how well the nanofiller is dispersed, if it contains any special functional groups, and

The part of using nanofillers that is challenging is that it is a complex process, where the results depend on many different factors. The epoxy chosen might not bond well with any fillers, which might prevent it's ability to be reinforced properly by any filler.

Chapter 7

Conclusions

7.1 Final Analysis and Future Work

This paper investigated and discussed the effects of nanomodification on the fracturing behavior and scaling of graphene nanocomposites, an aspect of utmost importance for structural design but so far overlooked. The analysis leveraged on a comprehensive set of fracture tests on geometrically scaled Single Edge Notch Bending (SENB) specimens of three different sizes and varying graphene contents. Based on the results obtained in this study, the following conclusions can be elaborated:

1. For all the investigated contents, the addition of graphene nanoplatelets to the resin did not provide a significant effect on the elastic properties and strength whereas an outstanding enhancement of mode I fracture energy was reported. A weight fraction of 1.6% of graphene resulted in an increase of the fracture energy of about 92.4% compared to the pristine resin, this result making graphene-modified resins ideal candidates for the development of tougher and more ductile composite structures;

2. The fracture tests on geometrically scaled SENB specimens confirmed a remarkable size effect. The analysis of the experimental data showed that the fracture scaling of the pure epoxy is captured accurately by Linear Elastic Fracture Mechanics (LEFM). However, this was not the case for graphene nanocomposites which exhibited a more complicated scaling. The double logarithmic plots of the nominal stress as a function of the characteristic size of the specimens showed that the fracturing behavior evolves from ductile to brittle with increasing sizes. For sufficiently large specimens, the data tend to the classical $-1/2$ asymptote predicted by LEFM. However, for smaller sizes, a significant deviation from LEFM was reported with data exhibiting a milder scaling, a behavior associated to a more pronounced ductility. This trend was more and more pronounced for increasing graphene contents;

3. The deviation from LEFM reported in the experiments is related to the size of the Fracture Process Zone (FPZ) for increasing contents of graphene. In the pure epoxy the damage/fracture zone close to the crack tip, characterized by significant non-linearity due to subcritical damaging, was generally very small compared to the specimen sizes investigated. This was in agreement with the inherent assumption of LEFM of negligible non-linear effects during the fracturing process. However, the addition of graphene nanoplatelets with the various additional damage mechanisms that come with it (such as e.g. platelet/matrix delamination, nano-crack deflection and plastic yielding), resulted in larger and larger FPZs. For sufficiently small specimens, the size of the highly non-linear FPZ was not negligible compared to the specimen characteristic size thus highly affecting

the fracturing behavior, this resulting into a significant deviation from LEFM;

4. Capturing the correct scaling of the fracturing behavior is of utmost importance for structural design. Further, it is quintessential to correctly measure important material properties such as the fracture energy. The analysis of the results reported in this study shows that using LEFM to calculate the mode I fracture energy from the experiments leads to a size dependent G_f. Taking the specimens with 1.6% wt of graphene as an example, the fracture energy according to LEFM was 0.8 N/mm, 1.0 N/mm and 1.25 N/mm for the small, medium and large sizes respectively. The reason for this discrepancy is that LEFM lacks intrinsically of a characteristic length and thus cannot capture the effects of the FPZ size;

5. Following Bažant [4,28,29], an Equivalent Fracture Mechanics approach was used to introduce a characteristic length, c_f, into the formulation. This length is related to the FPZ size and it is considered a material property as well as G_f. The resulting scaling equation, known as Bažant's Size Effect Law (SEL), depends not only on G_f but also on the FPZ size. An excellent agreement with experimental data is shown, with SEL capturing the transition from quasi-ductile to brittle behavior with increasing sizes. The fracture energy for the specimens with 1.6% wt of graphene, finally a material property independent of the specimen size, was 1.69 N/mm whereas $c_f = 1.59$ mm;

6. The difference between the fracture energy predicted by LEFM and SEL depends on the FPZ size compared to the specimen size, with LEFM underestimating G_f compared to SEL. For the specimens with 1.6% wt of graphene and the sizes considered in this work, LEFM predictions were about 113.3%, 49.2% and 20.9% lower compared to SEL for the small, medium and large sizes respectively. The difference decreases with increasing specimen sizes and tends to zero for sufficiently large specimens as the FPZ becomes negligible compared to the specimen size.

7. The foregoing evidences show that particular care should be devoted to the understanding of the scaling of the fracture behavior of nanocomposites. In particular, the fracture tests carried out to characterize e.g. the fracture energy should guarantee objective results. Size effect testing on geometrically scaled specimens is a simple and effective approach to provide objective data. Alternatively, LEFM could be used provided that the specimen size is large enough. The size limit depends on the size of the FPZ and the geometry of the tested specimen. For the SENB specimens investigated, a difference lower than 10% between the nominal strength predicted by LEFM and SEL can be guaranteed if $D \geq 4.263 g'(\alpha_0) c_f / g(\alpha_0)$. This limit is generally higher than the one suggested by ASTM D5045-99 to guarantee a plane strain condition.

The FPZ is an area where the material is weakened and the crack can propagate more easily. The purpose of the addition of nanoparticle is to strengthen this area to increase the overall fracture toughness of the material. However, the nanoparticles can weaken this zone by causing agglomeration if added in too high of a concentration. The purpose of this experiment is to determine the amount of graphene nanoparticles needed to allow for the greatest increase in fracture toughness without causing agglomeration. Since it has been observed that the fracture energy is continuing to increase, we have clearly not reached this critical concentration of graphene yet, despite the evidence of graphene pullout and microcracking.

Appendix

Drawings

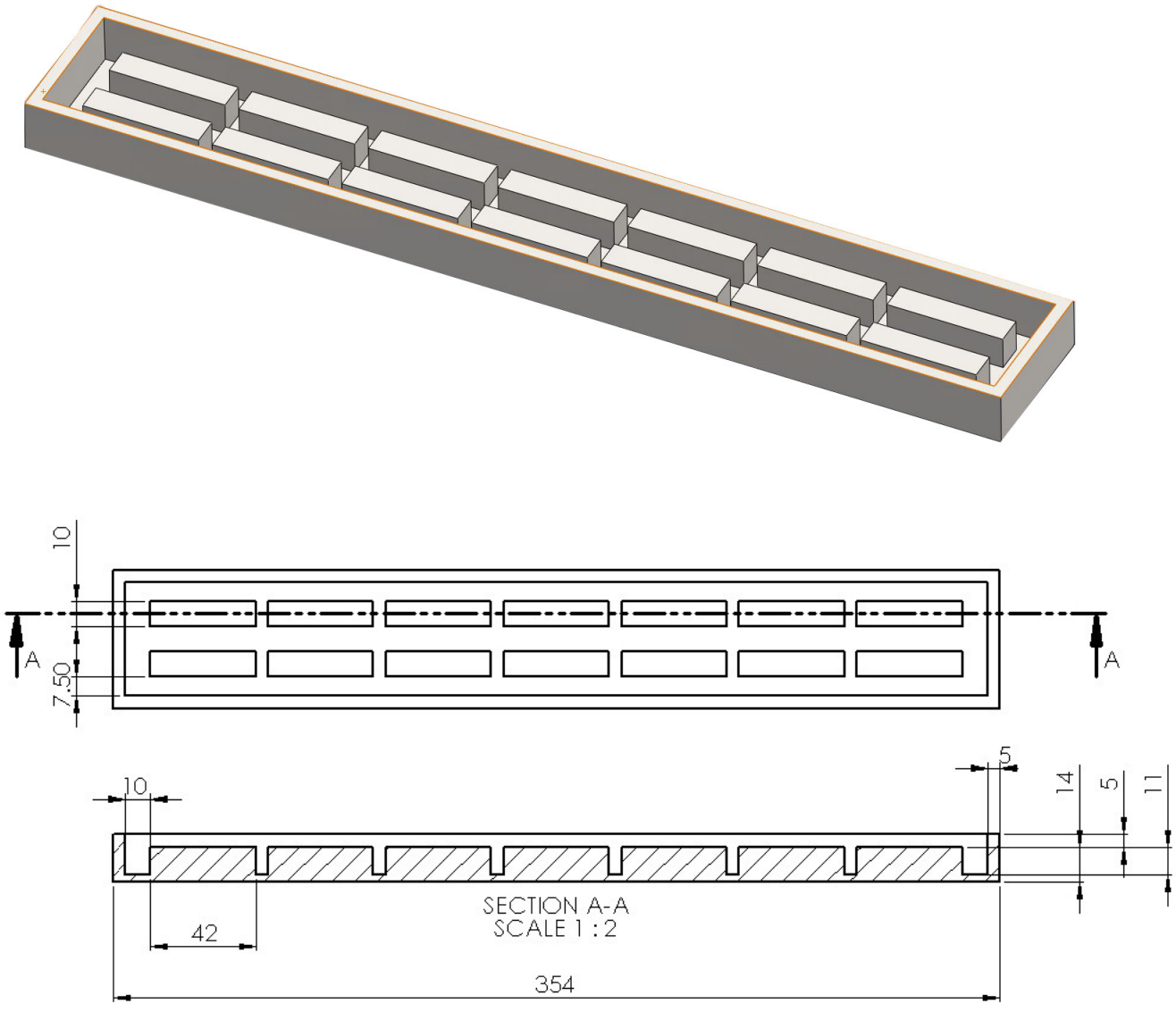

Figure 7.1: Smallest Specimen Mold Positive. Units: mm

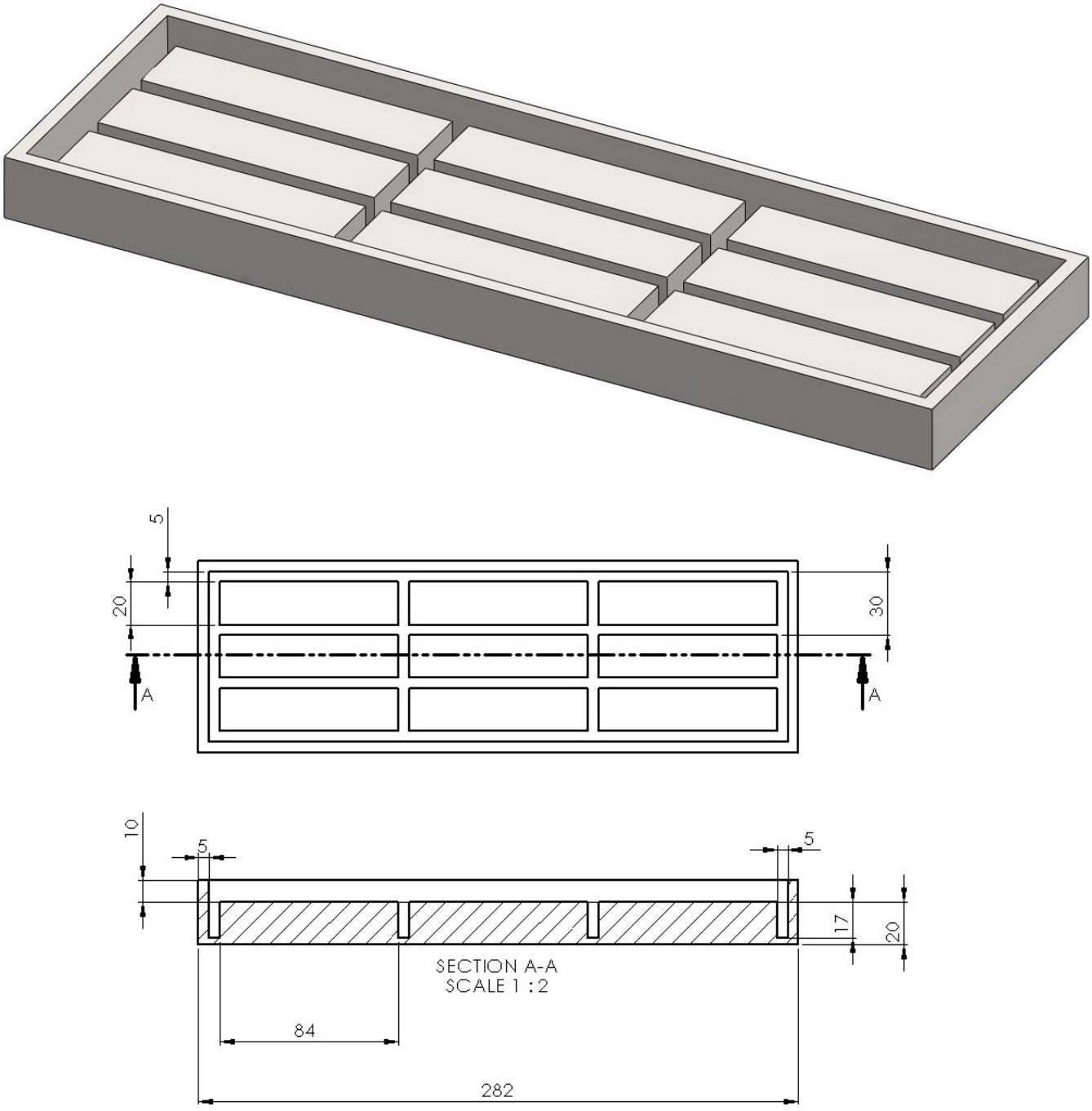

Figure 7.2: Second Smallest Specimen Mold Positive. Units: mm

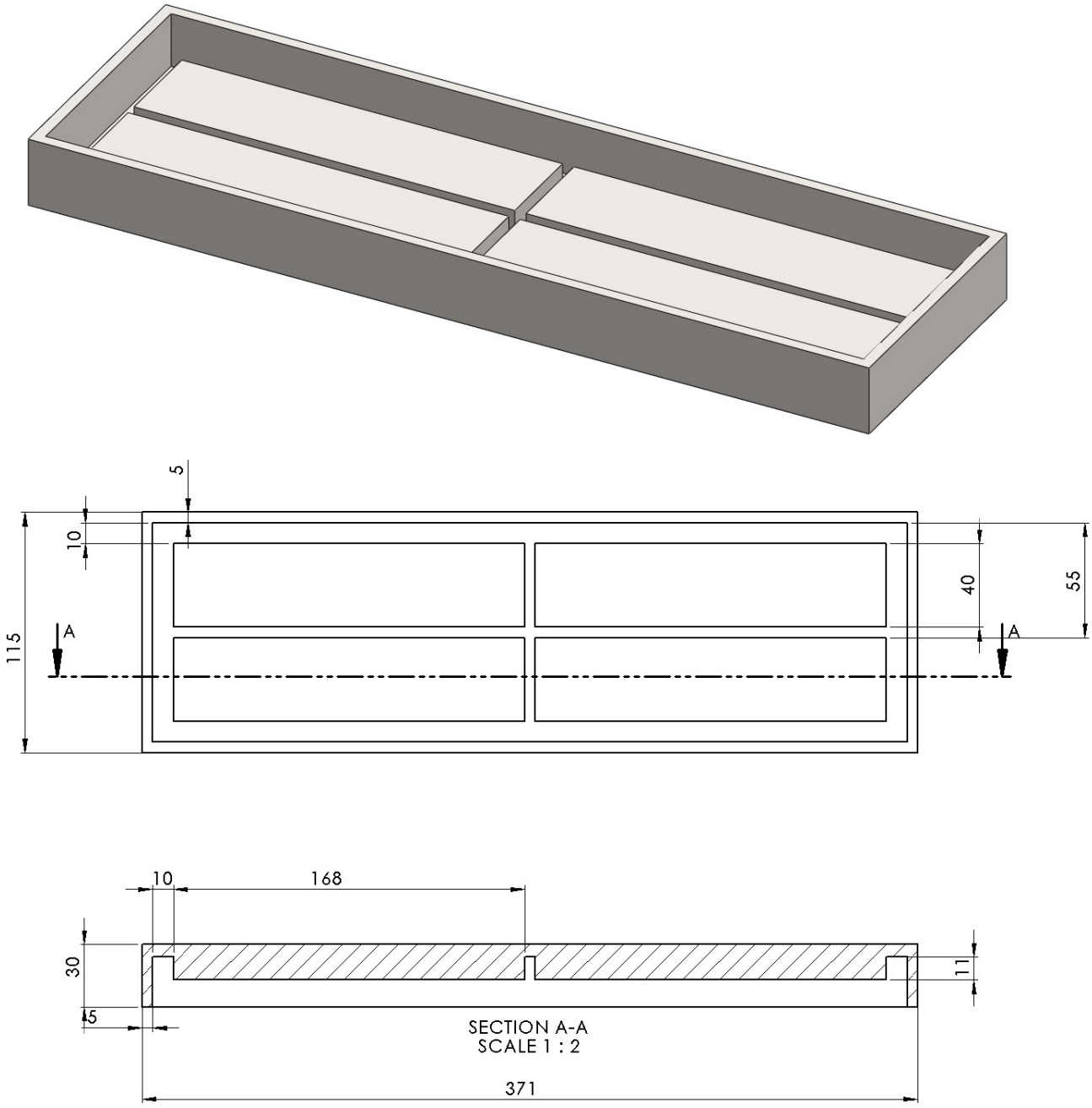

Figure 7.3: Medium Specimen Mold Positive. Units: mm

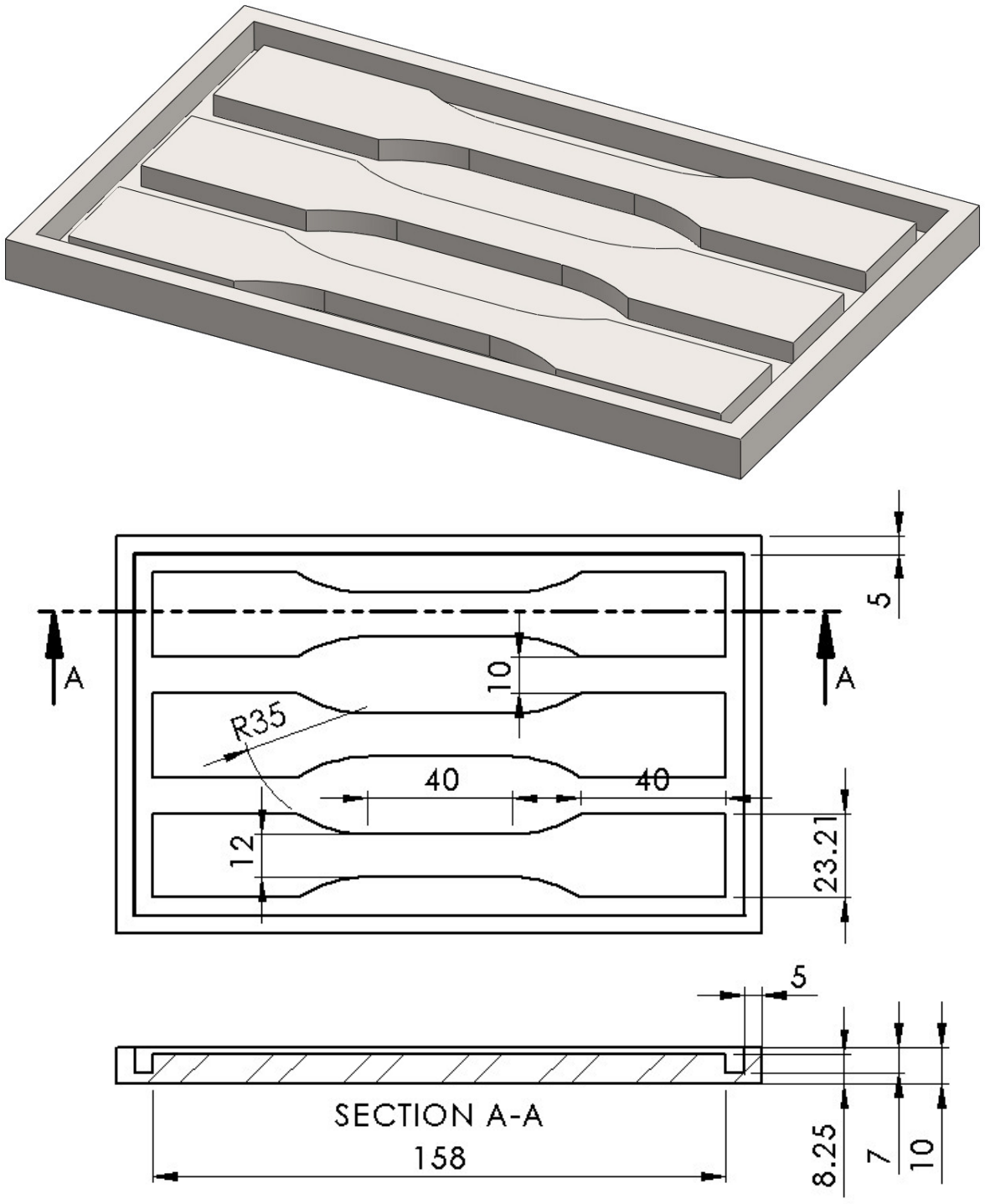

Figure 7.4: Dogbone Specimen Mold Positive. Units: mm

ABAQUS Meshes

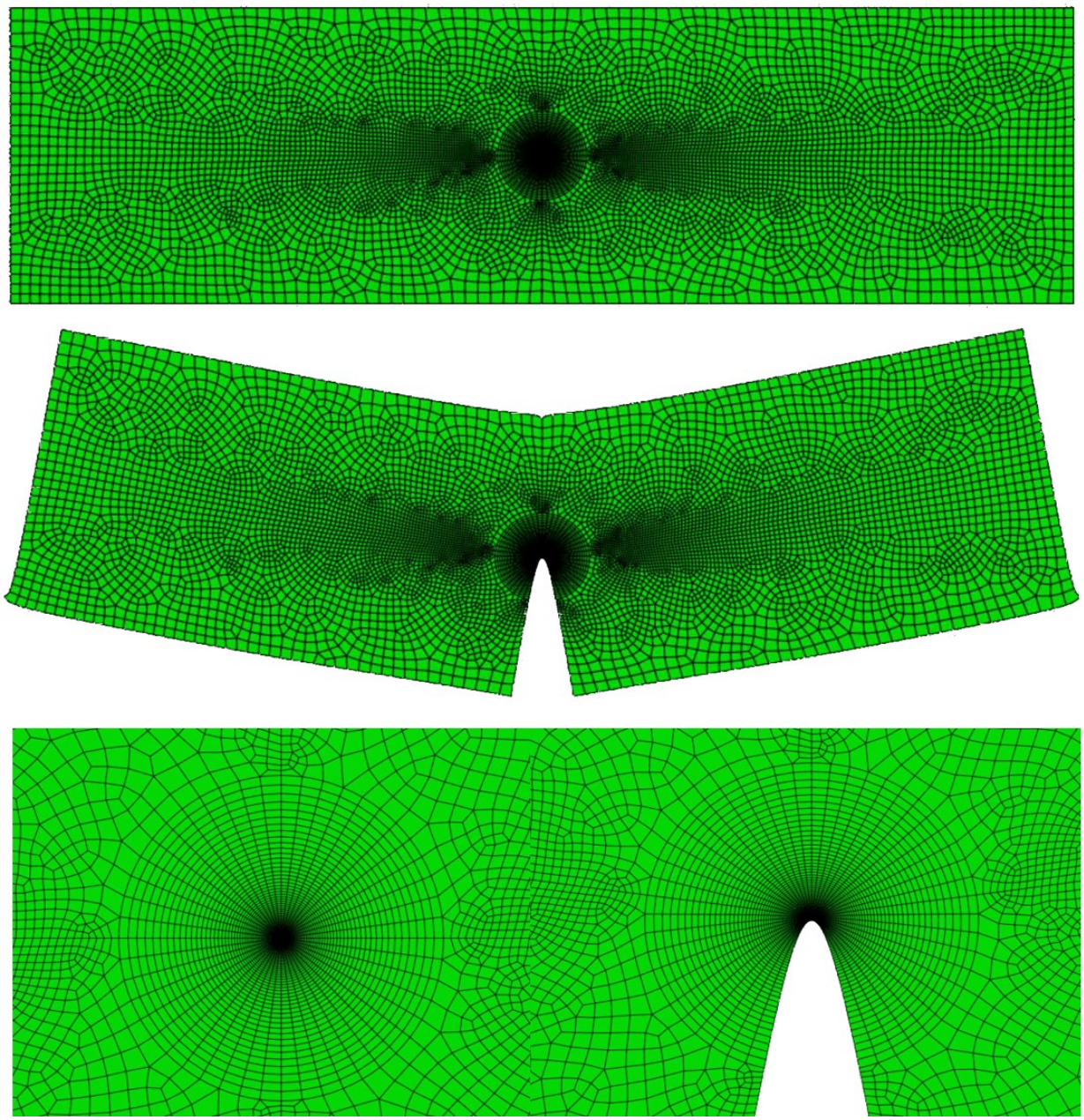

Figure 7.5: ABAQUS Mesh for Three-Point-Bending Test with Details

Original Crack/Notch Development Process and Results

Originally in this experiment, the cracks in the specimens were created by using a 0.3 mm jewelry saw. It was thought that this thin blade would allow for more control in creating a crack in the specimen that is geometrically scaled, since this is the same technique used when testing concrete. In addition, this crack creation method does not put the test specimen under a pre-load at the crack tip, which weakens the overall specimen. The process was to measure and mark the center of the sample on both sides, using the length and width measurements of the specimen. Next the crack is cut into the specimens, being careful to go slowly and carefully, to ensure that the crack remains straight. This part of the process was labor intensive, with the largest samples taking at least thirty minutes to create the respective cracks.

This method was used so as to ensure that the crack length of each defect was exactly one-half of the thickness (D) of the respective test coupon. So for the smallest samples, which have a width of approximately 10 mm, the crack would have a length of approximately 5 mm. Each sample's dimensions were measured, to ensure that the crack tip ends at the center of each specimen. The reason that the cracks were made in this manner was that the sawing action of the blade prevents the formation of a fracture process zone (FPZ) before running the test, which differs from traditional pre-fracturing procedures [27, 32].

When doing the three point bend testing for the epoxy samples, the critical loads measured were between 8 to 10 times higher than expected. These values were completely unrealistic in value and this led to doing analysis of the estimates and assumptions that were made. When the calculations were checked and no mathematical mistakes were found, attention turned to the crack creation method. This process for creating the crack was different than ones that had been used in other studies, so it was the next aspect of the experiment that was investigated as a possible reason for the differing values. I thought that it was possible that a notch had been created in these samples, instead of the desired crack. To test this assumption by creating two second smallest and two medium SENB specimens, identical to the ones previously measured, but these would have saw cuts one quarter of the length of the specimen width and a crack made with a razor blade for approximately the other quarter of the width. This means that the only difference would be how the cracks were made, but their respective lengths would be statistically similar in value. The results from this experiment can be seen in fig. 7.6.

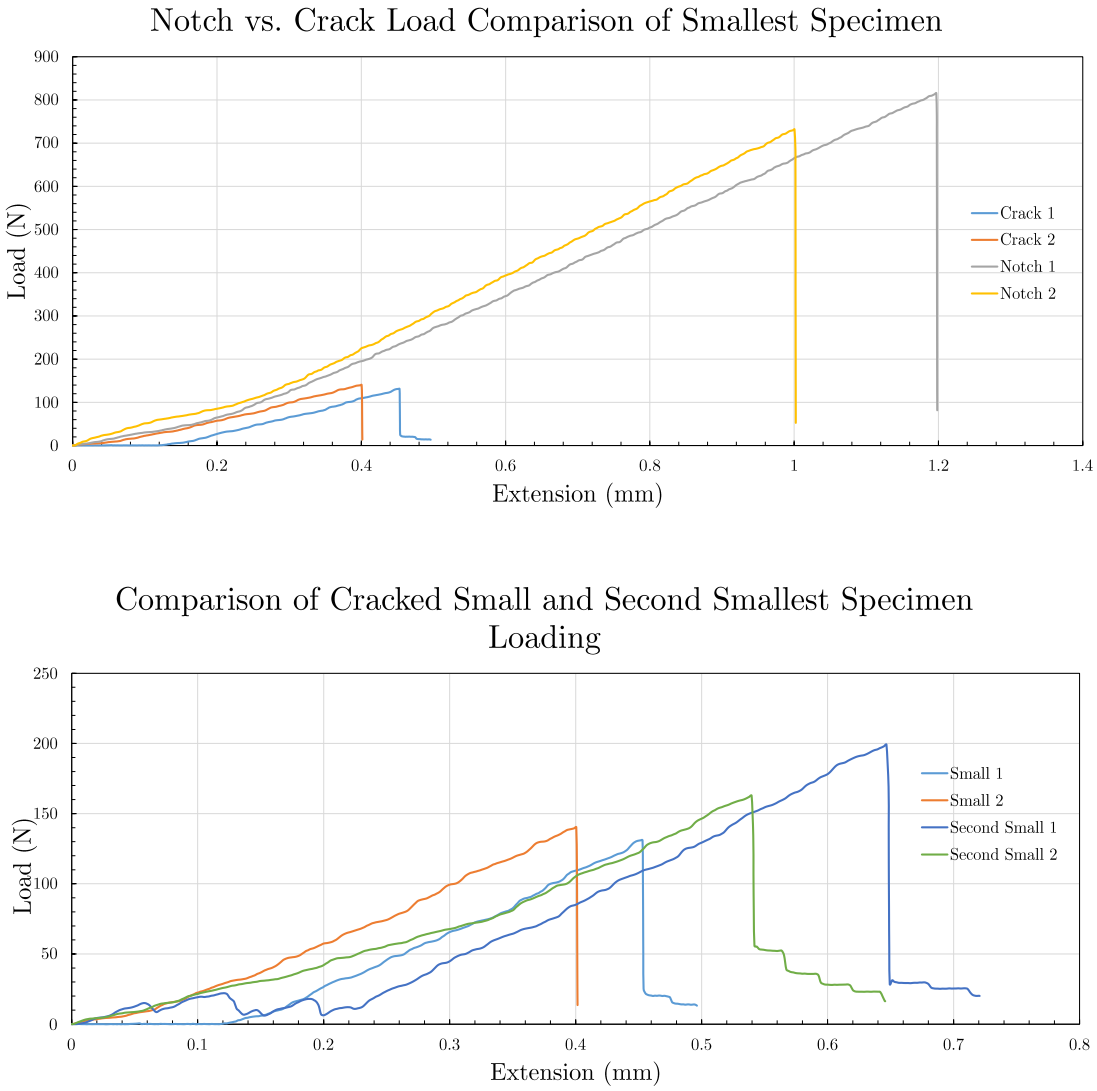

Figure 7.6: Notch vs Crack Load Analysis

What was found was that the creating the crack using the "tapping method" using a razor blade made the samples break at a critical loading approximately eight times lower than when the specimen has the notch made with the saw. These results are consistent with the conclusion that what was made with the saw was a notch for the composite and not a crack. There is a great deal of research that has been done with concrete fracture mechanics and crack propagation. They have found that using the "tapping method" does not provide sufficient cracking in the material. They instead make a saw cut in the concrete, which mimics a crack very well, since the diameter of the crack tip is significantly smaller than the crack length. The assumption was made that the same could be assumed for when making a crack in the epoxy specimens. The above testing shows that this original assumption was incorrect and as a result, the tapping method was used for the samples in this experiment. Using the tapping method means that my specimens are no longer exactly geometrically scaled, which will be taken into account in the data analysis.

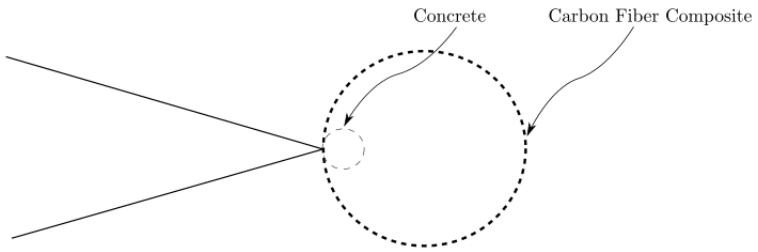

Figure 7.7: Comparison of Fracture Progress Zone Size in Concrete and Carbon Fiber Composites

There is a fracture process zone (FPZ) in front of the crack tip, which causes that area to be weaker than the surrounding material. This means that the crack can more easily propagate with the FPZ zone moving with it as the crack lengthens until the crack length equals the width of the specimen at fracture. In the samples tested, the cracks were made using a 0.3 mm jewelry saw, which is the same width as the razor blade that is used for creating cracks using tapping method. The extremely high critical load results that I received using the sawing method casts into doubt the original assumption that using the saw created a crack. In concrete, "cracks" are made using this exact method, so it was thought that this would also be a well controlled method to create proportional cracks for this experiment. Yet, the results point to the "crack" that was made is actually a notch. A notch behaves very differently than a crack and might explain the much higher critical loads measured.

Publications

Journal Articles

- Cory Mefford, Yao Qiao, Marco Salviato, "Fracture Behavior and Scaling of Graphene Nanocomposites", Composite Structures, 2017 (under review - available at http://arxiv.org/abs/1702.05828)
- Yao Qiao, Cory Mefford, Marco Salviato, "A Study on the Fracturing Behavior of General Nanocomposites, Composites Science and Technology, 2017 (under preparation)

Peer Reviewed Contributions at Conference Proceedings

- Cory Mefford, Marco Salviato, "Scaling of fracturing behavior of graphene reinforced polymers: experimental characterization and modeling", Engineering Mechanics Institute (EMI2016), Nashville, TN, May 22, 2016
- Yao Qiao, Cory Mefford, Marco Salviato, "Graphene Nanocomposites: A study on the failure behavior and scaling", International Conference on Composite Materials (ICCM21), Xi'an, China, August 20, 2017

Bibliography

[1] M. F. Ashby, S. F. Bush, R. Bullough N. Swindells, G. Ellison, Y. Lindblom, R. W. Cahn, and J.F. Barnes. Technology of the 1990s: Advanced materials and predictive design [and discussion]. *Philosophical Transactions of the Royal Society of London A: Mathematical, Physical and Engineering Sciences*, 322(1567):393–407, 1987.

[2] N.G McCrum, C.P. Buckley, and C.B Bucknall. *Principles of Polymer Engineering*. Oxford University Press, 1997.

[3] River Edge. *Graphene and It's Facinating Atributes*. World Scientific, 2011.

[4] Zdeněk Bažant and Jaime Planas. *Fracture and Size Effect in Concrete and Other Quasi-brittle Materials*. CRC Press, 1998.

[5] Richard F. Gibson. *Principles of Composite Material Mechanics*. CRC Press, 2012.

[6] Dennis Working, Peter Lilehei, Sharon Lowther, Emile Siochi, Jae-Woo Kim, Godfrey Sauti, Kristopher Wise, and Cheol Park. Effect of nanofiller characteristics on nanocomposite properties. *Langley Reasearch Center*, Hampton, Virginia, 2016.

[7] Debdatta Ratna. *Handbook of Thermoset Resins*. Smithers Rapra Technology, 2009.

[8] Nobel Media. The 2010 nobel prize in physics - press release. http://www.nobelprize.org/nobel_prizes/physics/laureates/2010/press.html, 2010.

[9] Changgu Lee, Xiaoding Weil, Jeffrey Kysarl, and James Hone. Measurement of the elastic properties and intrinsic strength of monolayer graphene. *Science*, 321:385–388, 2008.

[10] Phys.org. Graphene outperforms carbon nanotubes for creating stronger, more crack-resistant materials. http://phys.org/news/2010-04-graphene-outperforms-carbon-nanotubes-stronger.html, 2010.

[11] Swetha Chandrasekaran, Narumichi Sato, Folke Tölle, Rolf Mülhaupt, Bodo Fiedler, and Karl Schulte. Fracture toughness and failure mechanism of graphene based epoxy composites. *Composites Science and Technology*, 97:90–99, 2014.

[12] Byung Chul Kim, Sang Wook Park, and Dai Gil Lee. Fracture toughness of the nano-particle reinforced epoxy composite. *Composites Structures*, 86:69–77, 2008.

[13] Deok-Bo Lee, Toru Ikeda, Noriyuki Miyazaki, and Nak-Sam Choi. Damage zone around crack tip and fracture toughness of rubber-modified epoxy resin under mixed-mode conditions. *Engineering Fracture Mechanics*, 69:1363–1375, 2002.

[14] M. Martin-Gallego, M.M. Bernal, M. Hernandez, R. Verdejo, and M.A. Lopez-Manchado. Comparison of filler percolation and mechanical properties in graphene and carbon nanotubes filled epoxy nanocomposites. *European Polymer Journal*, 49:1347–1353, 2013.

[15] Shafi Ullah Khan, Jayaram R. Pothnis, and Jang-Kyo Kim. Effects of carbon nanotube alignment on electrical and mechanical properties of epoxy nanocomposites. *Composites: Part A*, 49:26–34, 2013.

[16] Izzuddin Zaman, Tam Thanh Phan, Hsi-Chiang Kuan, Qingshi Meng, Ly Truc Bao La, Lee Luong, Osama Youssf, and Jun Ma. Epoxy/graphene platelets nanocomposites with two levels of interface strength. *Polymer*, 52:1603–1611, 2011.

[17] John Rogers. Electronic materials: making graphene for macroelectronics. *Nature Nanotecnology*, 3(5):254–255, 2008.

[18] Abd Rashid bin Mohd Yusoff, Liming Dai, Hui-Ming Cheng, and Jie Liu. Graphene based energy devices. *Nanoscale*, 7:6881–6882, 2015.

[19] Abhishek K. Pathak, Munu Borah, Ashish Gupta, T. Yokozeki, and Sanjay R. Dhakate. Improved mechanical properties of carbon fiber/graphene oxide-epoxy hybrid composites. *Composites Science and Technology*, 135:28–38, October 2016.

[20] Xiao Wang, Jie Jin, and Mo Song. An investigation of the mechanism of graphene toughening epoxy. *Carbon*, 65:324–333, 2013.

[21] Swetha Chandrasekaran, Christian Seidel, and Karl Schulte. Preparation and characterization of graphite nano-platelet (gnp)/epoxy nano-composite: Mechanical, electrical and thermal properties. *European Polymer Journal*, 49:3878–3888, 2013.

[22] Ming-Wei Lee, Tai-Yuan Wang, and Jia-Lin Tsai. Mechanical properties of nanocomposites with functionalized graphene. *Journal of Composite Materials*, 50(27):3779–3789, 2016.

[23] Long-Cheng Tang, Yan-Jun Wan, Dong Yan, Yong-Bing Pei, Li Zhao, Yi-Bao Li, Lian-Bin Wu, Jian-Xiong Jiang, and Guo-Qiao Lai. The effect of graphene dispersion on the mechanical properties of graphene/epoxy composites. *Carbon*, 60:16–27, 2013.

[24] Tongwu Jiang, Tapas Kuila, Nam Hoon Kim, Bon-Cheol Ku, and Joong Hee Lee. Enhanced mechanical properties of silanized silica nanoparticle attached graphene oxide/epoxy composites. *Composites Science and Technology*, 79:115–125, 2013.

[25] M.M. Shokrieh, M. Esmkhani S.M. Ghoreishi, and Z. Zhao. Effects of graphene nanoplatelets and graphene nanosheets on fracture toughness of epoxy nanocomposites. *Fatigue and Fracture of Engineering Materials and Structures*, 37:1116–1123, 2014.

[26] D. Galpaya, M. Wang, G. George, N. Motta, and E. Waclawik. Preparation of graphene oxide/epoxy nanocomposites with significantly improved mechanical properties. *Journal of Applied Physics*, 116(5):053518, 2014.

[27] Marco Salviato, Kedar Kirane, Shiva Esna Ashari, Zdeněk Bažant, and Gianluca Cusatis. Experimental and numerical investigation of intra-laminar energy dissipation and size effect in two-dimensional textile composites. *Composites Science and Technology*, 135:67–75, 2016.

[28] Zdeněk Bažant. Size effect in blunt fracture: concrete, rock, metal. *Journal of Engineering Mechanics*, 110(4):518–535, 1984.

[29] Zdeněk Bažant and M.T. Kazaemi. Determination of fracture energy, process zone length and brittleness number from size effect, with application to rock and concrete. *International Journal of Fracture*, 44:111–131, 1990.

[30] Zdeněk Bažant, Issac Daniel, and Zhengzhi Li. Size effect and fracture characteristics of composite laminates. *Journal of Engineering Materials and Technology*, 118(3):317–324, 1996.

[31] C.E. Inglis. Stresses in a plate due to the presence of cracks and sharp corners. *Technical Institute Naval Architects*, 55:219–241, 1913.

[32] American Society for Testing and Materials. *D5045-99 - Standard test methods for plane-strain fracture toughness and stain energy release rate of plastic materials.* ASTM, 1999.

[33] American Society for Testing and Materials. *ASTM D638-02a - Standard Test Method for Tensile Properties of Plastics.* ASTM, 2003.

[34] TAP Plastics. Silicone rtv mold-making system. http://www.tapplastics.com, 2016.

[35] Hexion. Epikote resin mgs. http://hexion.com.

[36] Graphene Supermarket. A-12 graphene nanoplatelet. https://graphene-supermarket.com.

[37] Mixer Direct. https://graphene-supermarket.com.

[38] Hielscher Ultrasound Technology. https://www.hielscher.com.

[39] Robinair. http://www.robinair.com.

[40] Marino Quaresimin, Marco Salviato, and Michele Zappalorto. Fracture and interlaminar properties of clay-modified epoxies and their glass reinforced laminates. *Engineering Fracture Mechanics*, 81:80–93, 2012.

[41] Michele Zappalorto, Marco Salviato, and Marino Quaresimin. Mixed mode (i+ii) fracture toughness of polymer nanoclay nanocomposites. *Engineering Fracture Mechanics*, 111:50–64, 2013.

[42] Michele Zappalorto, Marco Salviato, A Pontefisso, and Marino Quaresimin. Fracture and interlaminar properties of clay-modified epoxies and their glass reinforced laminates. *Engineering Fracture Mechanics*, 20(6):405–419, 2013.

[43] Keqin Xiao, Ye Lin, and Yuk Kwok. Effects of precracking methods on fracture behaviour of an araldite-f epoxy and its rubber-modified systems. *Journal of Material Science*, 33(11):2831–2836, 1998.

[44] M.S. Cayard and W.L. Bradley. The effect of various precracking techniques on the fracture toughness of plastics. In *General Papers*, pages 2713–2723, Houston, USA, 1989. International Conference of Fracture ICF7.

[45] Correlated Solutions. Digital image capture (dic). http://www.correlatedsolutions.com.

[46] Jeol. Scanning electron microscopes. http://www.jeol.co.jp/en/science/sem.html.

[47] Ming-Wei Lee, Tai-Yuan Wang, and Jia-Lin Tsai. Mechanical properties of nanocomposites with functionalized graphene. *Journal of Composite Materials*, 1/13/16:1–11, 2016.

[48] Marco Salviato, Michele Zappalorto, and Marino Quaresimin. The effect of surface stresses on the critical debonding stress around nanoparticles. *International Journal of Fracture*, 172(1):97–103, 2011.

[49] M. Salviato, M. Zappalorto, and M. Quaresimin. Plastic yielding around nanovoids. *Procedia Engineering*, 10:3316 – 3321, 2011.

[50] Michele Zappalorto, Marco Salviato, and Marino Quaresimin. Influence of the interphase zone on the nanoparticle debonding stress. *Composites Science and Technology*, 72(1):49 – 55, 2011.

[51] M. Zappalorto, M. Salviato, and M. Quaresimin. Assessment of debonding-induced toughening in nanocomposites. *Procedia Engineering*, 10:2973 – 2978, 2011.

[52] Michele Zappalorto, Marco Salviato, and Marino Quaresimin. A multiscale model to describe nanocomposite fracture toughness enhancement by the plastic yielding of nanovoids. *Composites Science and Technology*, 72(14):1683 – 1691, 2012.

[53] Michele Zappalorto, Marco Salviato, and Marino Quaresimin. Stress distributions around rigid nanoparticles. *International Journal of Fracture*, 176(1):105–112, 2012.

[54] Marco Salviato, Michele Zappalorto, and Marino Quaresimin. Plastic shear bands and fracture toughness improvements of nanoparticle filled polymers: A multiscale analytical model. *Composites Part A: Applied Science and Manufacturing*, 48:144 – 152, 2013.

[55] Marco Salviato, Michele Zappalorto, and Marino Quaresimin. Nanoparticle debonding strength: A comprehensive study on interfacial effects. *International Journal of Solids and Structures*, 50(2021):3225 – 3232, 2013.

[56] M. Quaresimin, M. Salviato, and M. Zappalorto. A multi-scale and multi-mechanism approach for the fracture toughness assessment of polymer nanocomposites. *Composites Science and Technology*, 91:16 – 21, 2014.

[57] Jim Rice. A path independent integral and the approximate analysis of strain concentration by notches and cracks. *Journal of Applied Mechanics*, 35:379–386, 1968.

[58] Peerapan Dittanet and Raymond Pearson. Effect of silica nanoparticle size on toughening mechanisms of filled epoxy. *Polymer*, 53:1890–1905, 2012.

[59] Hong-Yuan Liu, Gong-Tao Wang, Yiu-Wing Mai, and Ying Zeng. On fracture toughness of nano-particle modified epoxy. *Composites: Part B*, 42:2170–2175, 2011.

[60] Milad Zamanian, Mehrzad Mortezaei, Babak Salehnia, and J.E. Jam. Fracture toughness of epoxy polymer modified with nanosilica particles: Particle size effect. *Engineering Fracture Mechanics*, 97:193–206, 2013.

[61] Raneesh Konnola, C.P. Reghunadhan Nair, and Kuruvilla Joseph. High strength toughened epoxy nanocomposite based on poly(ether sulfone)-grafted multi-walled carbon nanotube. *Polymers Advanced Technologies*, 27:82–89, 2015.

[62] Walid Naous, Xiao-Yan Yu, Qing-Xin Zhang, Kimiyoshi Naito, and Yutaka Kagawa. Morphology, tensile properties and fracture toughness of epoxy/al_2o_3 nanocomposites. *Journal of Polymer Physics*, 44:1466–1473, 2006.

[63] Bernd Wetzel, Patrick Rosso, Frank Haupert, and Klaus Friedrich. Epoxy nanocomposites fracture and toughening mechanisms. *Engineering Fracture Mechanics*, 73:2375–2398, 2006.

[64] Hui Zhang, Long-Cheng Tang, Zhong Zhang, Klaus Friedrich, and Stephan Sprenger. Fracture behaviours of in situ silica nanoparticle-filled epoxy at different temperatures. *Polymer*, 49:3816–3825, 2008.

[65] B.B. Johnsen, A.J. Kinloch, R.D. Mohammed, A.C. Taylor, and S. Sprenger. Toughening mechanisms of nanoparticle-modified epoxy polymers. *Polymer*, 48:530–541, 2007.

[66] Jun Ma, Mao-Song Mo, Xu-Sheng Du, Patrick Rosso, Klaus Friedrich, and Hsu-Chiang Kuan. Effect of inorganic nanoparticles on mechanical property, fracture toughness and toughening mechanism of two epoxy systems. *Polymer*, 49:3510–3523, 2008.

[67] Chenggang Chen, Ryan S. Justice, Dale W. Schaefer, and Jeffery W. Baur. Highly dispersed nanosilicaepoxy resins with enhanced mechanical properties. *Polymer*, 49:3805–3815, 2008.

[68] D. Carolan, A. Ivankovic, A.J. Kinloch, S. Sprenger, and A.C. Taylor. Toughening of epoxy-based hybrid nanocomposites. *Polymer*, 97:179–190, 2016.

[69] Daniel R. Bortz, César Merino, and Ignacio Martin-Gullon. Carbon nanofibers enhance the fracture toughness and fatigue performance of a structural epoxy system. *Composites Science and Technology*, 71:31–38, 2011.

[70] Gowthaman Swaminathan and Kunigal Shivakuma. Thermomechanical and fracture properties of exfoliated nanoclay nanocomposites. *Journal of Reinforced Plastics and Composites*, 30.3:256–268, 2011.

[71] Hossein Salehi Vaziri, Mohamadreza Abadyan, Meisam Nouri, Iraj Amiri Omaraei, Zahra Sadredini, and Mohamad Ebrahimnia. Investigation of the fracture mechanism and mechanical properties of polystyrene/silica nanocomposite in various silica contents. *Journal of Materials Science*, 46:5628–5638, 2011.